Title: Novel quantal analysis method reveals conservation of average excitatory synaptic charge across cortical pyramidal neurons of different sizes

Author Names and Affiliations: Martynas Dervinis[1], Guy Major[1]

[1]: Cardiff University, Cardiff, Wales, CF10 3AT, UK

Corresponding author email address: martynas.dervinis@gmail.com

Number of pages: 52

Number of figures: 12

Abstract: 224

Body text excluding Materials and Methods: 4193 (946 + 3247)

Conflict of interest statement: The authors declare no competing financial interests.

Acknowledgements: Cardiff University (GM, MD), The Medical Research Council of the UK (MD PhD scholarship). Neural activity simulations and minis' distribution fitting were performed on the Cardiff School of Biosciences' Biocomputing Hub HPC/Cloud infrastructure.

Abstract

In chemical synapses of the central nervous system (CNS), information is transmitted via the presynaptic release of a vesicle (or 'quantum') of neurotransmitter, which elicits a postsynaptic electrical response with an amplitude termed the 'quantal size'. Measuring amplitudes of miniature postsynaptic currents (mPSCs) or potentials (mPSPs) at the cell soma is generally thought to offer a technically straightforward way to estimate quantal sizes, as each of these miniature responses (minis) is generally thought to be elicited by the spontaneous release of a single neurotransmitter vesicle. However, in large highly-branched neurons, a somatically recorded mini is typically massively attenuated compared with at its input site, and a significant fraction are indistinguishable from (or cancelled out by) background noise fluctuations. Here, using a new software package called 'minis', we describe a novel quantal analysis method that estimates the 'electrical size' of the synapse by comparing events detected in somatic recordings from the same neuron of (a) *real* minis and (b) background noise (minis blocked pharmacologically) with *simulated* minis added by a genetic algorithm. The estimated minis' distributions reveal a striking inverse dependence of mean excitatory mPSP amplitude on total cell capacitance (proportional to cell size, more exactly, extracellular membrane surface area) suggesting that, in rats at least, the average charge (ca. 30 fC) injected by excitatory synapses is conserved across neocortical pyramidal neurons of different sizes.

Abbreviations

ABF – Axon Binary File

aCSF – artificial cerebrospinal fluid

AMPA – α-amino-3-hydroxy-5-methyl-4-isoxazolepropionic acid

AMPAR – α-amino-3-hydroxy-5-methyl-4-isoxazolepropionic acid receptor

ANN – artificial neural network

AP – action potential

CGP55845A – selective competitive antagonist of $GABA_B$ receptors (thus slow K^+ dependent IPSPs)

CPP – (*RS*)-3-(2-carboxypiperazin-4-yl)-propyl-1-phosphonic acid (potent selective competitive glutamate NMDA receptor antagonist, thus depolarization-dependent, slow component of EPSPs)

EPSC – excitatory postsynaptic current

EPSP – excitatory postsynaptic potential

GA – genetic algorithm

GABA – gamma-aminobutyric acid (inhibitory neurotransmitter)

IC50 – concentration blocking half of the receptors

IPSC – inhibitory post-synaptic current

IPSP – inhibitory post-synaptic potential

MAD – maximum absolute deviation

mEPSC– miniature excitatory post-synaptic current

mEPSP– miniature excitatory post-synaptic potential

60 mIPSP– miniature inhibitory post-synaptic potential

61 mPSC – miniature post-synaptic current

62 mPSP – miniature post-synaptic potential

63 NBQX – 2,3-dioxo-6-nitro-1,2,3,4-tetrahydrobenzo[*f*]quinoxaline-7-sulfonamide (potent selective

64 competitive antagonist of AMPA (and kainate) glutamate receptors, thus fast component of EPSPs)

65 NMDA – N-methyl-D-aspartate

66 NMDAR - N-methyl-D-aspartate receptor

67 SAD – sum of absolute deviations

68 SD – standard deviation

69 smEPSP – simulated mEPSP

70 SSD – sum of signed deviations

71 SSE – sum of squared errors

72 TTX – tetrodotoxin (potent selective competitive antagonist of Na^+ channels, thus action potentials)

73 V_m – transmembrane potential

74

Introduction

Synaptic transmission in the CNS occurs in 'quanta' (Forti et al., 1997; Hardingham et al., 2010; Isaacson and Walmsley, 1995; Jonas et al., 1993; Kraszewski and Grantyn, 1992; Kullmann and Nicoll, 1992; Kuno, 1964; Larkman et al., 1991; Sahara and Takahashi, 2001; Stern et al., 1992; Wall and Usowicz, 1998), usually thought to each correspond to the release of a single neurotransmitter vesicle (Heuser et al., 1979). The amplitude of the postsynaptic response to a quantum of transmitter, the quantal size, is a key parameter defining the efficacy of synaptic transmission (Katz, 1969; Vere-Jones, 1966) and, therefore, an important determinant of neural computation.

Quantal size measurements in the CNS are difficult due to multi-synaptic contacts (multiple synapses per connection between a particular pair of neurons and multiple release sites/postsynaptic densities/receptor "rafts" for some synapses), limited accessibility, significant quantal variance (both within and between synapses of a given connection), temporal non-stationarity of synaptic properties (e.g. receptor desensitisation or internalisation, and depletion of glutamate from presynaptic vesicles), and low signal-to-noise ratios of somatic electrophysiological recordings of quantal events (Bekkers, 1994; Farsi et al., 2021; Korn and Faber, 1991). For these reasons classical quantal analysis as done at the neuromuscular junction has run into problems in central synapses, where most of the minis do not 'stand out' from the noise. More recent methods such as noise deconvolution, Variance-Mean analysis, and optical quantal analysis have not fared much better (Biró et al., 2005; Clamann et al., 1991; Clements, 2003; Clements and Silver, 2000; Edwards et al., 1976; Enoki et al., 2009; Jack et al., 1981; Liu et al., 2022; Oertner et al., 2002; Peled and Isacoff, 2011; Redman, 1990; Reid and Clements, 1999; Silver, 2003; Yuste et al., 1999), or suffer from potential selection biases (e.g. paired recordings typically require cells close together whose synapses may be a non-representative sub-population, differing from the overall population of synapses).

A complementary method of assessing synaptic function is to measure properties of mPSCs. Miniature PSC amplitude measurements are often taken as quantal size estimates across the population of active synapses onto a neuron, as the mPSC (under voltage clamp) or mPSP (under voltage recording) likely corresponds to the response to a spontaneous release of a single neurotransmitter vesicle (Brown et al., 1979; del Castillo and Katz, 1954; Fatt and Katz, 1952; Isaacson and Walmsley, 1995; Wall and Usowicz, 1998). Measurements of mPSC amplitudes are routine in the literature. However, they are likely overestimates due to small amplitude events being difficult to detect and largely being missed or lost in the noise.

The use of voltage clamp can be a major reason why mPSCs “go missing”. Theoretical studies (Major, 1993a; Rall and Segev, 1985; Spruston et al., 1993) predicted and experimental findings (Williams and Mitchell, 2008) confirmed that somatic voltage clamp fails to space clamp extended dendrites, and to capture all (or even most of) the current flowing in at electrically remote synapses. Amplitude attenuation can also be caused if series resistance is not compensated (Major, 1993a; Williams and Mitchell, 2008). These issues can be somewhat sidestepped by switching to voltage recording, at the cost of (a little) more temporal integration.

However, most mPSCs go undetected because of the electrophysiology of the neuron itself. Distal minis leak charge via the dendritic membrane, but an even more significant amplitude attenuation, 40-fold or more, is inflicted by charging the membrane capacitance of the entire dendritic arbour (Larkum et al., 2009; Major et al., 2013a; Nevian et al., 2007; Stuart and Spruston, 1998; Williams and Mitchell, 2008; Williams and Stuart, 2002). Such amplitudes, at the soma (approximately 80 µV, on average, in layer 5 pyramidal neurons (Nevian et al. 2007), detected via simultaneous dendritic whole-cell recordings) are often indistinguishable from noise fluctuations. Recording from thin dendrites close to synaptic input sites is technically extremely challenging – a tour de force beyond

126 most labs. Therefore, a reliable yet widely accessible quantal analysis method, based on standard
127 somatic whole-cell patch recording, would require taking account of the background noise in
128 addition to measuring putative mPSPs (or mPSCs).
129
130 Here we describe such a method, based on recording excitatory mPSPs (mEPSPs) in the presence of
131 background physiological noise ('noise with minis') then noise alone, from the same cell, after
132 blocking mEPSPs pharmacologically. To detect mEPSP-like events in these recordings, we used a
133 newly developed algorithm called 'minis' which is described in our companion article (Dervinis and
134 Major, 2024). Because of small potentials being 'overshadowed' by larger minis, either by
135 summating with them on rising phases, or having their amplitudes reduced on decaying phases
136 (analysed and discussed in detail in our companion article (Dervinis and Major, 2024)), events
137 detected in the 'noise-alone' recording cannot be used to remove the noise component in the 'noise
138 with minis' recording simply by subtracting their two distributions. Instead, we adopted the
139 approach of using simulated minis, superimposing them on the 'noise-alone' recording and varying
140 their parameters until the amplitude and rise time distributions of events detected in the 'noise with
141 simulated minis' voltage trace closely matches those from the 'noise with real minis' recording, with
142 identical detection parameters. Therefore, we augmented our 'minis' software with a genetic
143 optimisation algorithm (GA) that automatically adjusts amplitudes, rise times and frequencies of
144 simulated minis until a statistically indistinguishable match is achieved. This novel quantal analysis
145 method produced an unbiased 'upper limit' quantal charge estimate for excitatory neocortical
146 synapses in the rat of approximately 31.3 pC, on average, which was conserved across pyramidal
147 neurons of all sizes in cortical layers 2/3 and 5. 'Minis' thus provides an experimentally
148 straightforward quantal analysis method for detecting mPSPs or mPSCs in somatic recordings, and
149 (in aggregate) 'separating' the smaller of these events from comparably-sized background noise
150 fluctuations.
151

Materials and Methods

Animals and electrophysiology

All experimental procedures were carried out in accordance with the UK Animals (Scientific Procedures) Act 1986. The full description is provided in our companion article (Dervinis and Major, 2024). Coronal somatosensory neocortical slices obtained from 19- to 27-day old Wistar rats (RRID:RGD_13508588; n = 11) were used to obtain whole-cell voltage recordings (n = 14) of mEPSPs in the background of physiological (and other) noise ('noise with minis' condition), by superfusing artificial cerebrospinal fluid (aCSF) containing blockers of action potentials (APs) and inhibitory postsynaptic potentials (IPSPs). Excitatory postsynaptic potential (EPSP) blockers were then added ('noise-alone' condition, with all glutamatergic, GABAergic and AP-dependent synaptic potentials blocked, i.e. the vast majority of fast synaptic inputs in the neocortex), and background noise traces were recorded from each cell, while maintaining stability of the whole-cell recording (as judged by numerous criteria, below).

Passive membrane time constant, total membrane capacitance, input resistance, and bridge balance (series resistance compensation) error were estimated by injecting current pulses as described in (Major et al., 1993).

Methodology

The goal of the study was to design an experimentally straightforward quantal analysis method based on standard somatic recordings of minis, as opposed to far more challenging recordings from sub-micron diameter input dendrites closer to (a few of) the synapses. Due to their low signal-to-noise ratio, *simulated* minis were used to infer the signal (mEPSP) component and to eliminate (in aggregate) the noise component in these recordings.

177 The experimental design of this study was similar to the one described in the preceding companion
178 article (Dervinis and Major, 2024). As described in the previous section, whole-cell recordings were
179 obtained where first mEPSPs were recorded in the background of physiological and other noise
180 followed by blocking EPSPs pharmacologically to record 'pure' noise in the absence of minis.
181 Simulated mEPSPs (smEPSPs) were then randomly added to the noise traces (Figure 1) and the
182 'minis' algorithm was applied to this 'noise with simulated minis' voltage trace. The resulting
183 distribution of detected events (in terms of their amplitudes and 10-90% rise times) was compared
184 to the equivalent distribution based on the 'noise with real minis' recording, detected with the same
185 parameters (such as amplitude detection threshold, baseline duration and maximum rise time gap
186 till each peak). The discrepancy between the two distributions was used to inform the GA, which
187 would then adjust the distribution of smEPSPs and generate new 'noise with simulated minis'
188 voltage traces and compare them again to the equivalent distribution detected with the same
189 parameters from the 'noise with real minis' recording. This procedure was repeated multiple times
190 (of the order of tens to hundreds of generations with 260 examples per generation; 10 examples per
191 each parameter optimised by the GA) until the two distributions were closely matched, within the
192 bounds of chance statistical errors (details below). At the end of this process the minis distribution
193 used for simulating the closely matched recording was deemed to be the inference of the true minis
194 distribution underlying the 'noise with real minis' recording (or at least compatible with it).
195
196 **Detection of miniature postsynaptic potentials**
197 Detection of real and simulated mEPSPs was carried out using our 'minis' software. The detailed
198 description of this detection algorithm is provided in the companion article (Dervinis and Major,
199 2024). We used the same detection algorithm parameters as described in that article except for the
200 amplitude range, which was set to 0.02-10 mV.
201
202 **Selection of recordings for fitting distributions of detected real minis-like events**

203 Prior to carrying out any estimation of the distribution of minis, segments of 'noise with real minis'
204 and 'noise-alone' recordings were carefully selected. Segments containing unusual amount of noise
205 or V_m glitches were rejected. Parts of recording showing instability or drift of recording parameters
206 (or excessive movement of the recording pipette relative to the soma) were also rejected, to ensure
207 that only good quality data were used. Data analysis performed at this preprocessing/selection stage
208 were built into our 'minis' software.
209
210 As part of the preprocessing stage, 'minis' produced seven graphs showing the evolution of various
211 recording parameters across the entire duration of a single recording. An example (from the longest
212 recording obtained) is provided in Figure 2, showing these graphs as individual panels. Figure 2A
213 shows the evolution of V_m from the very beginning of the recording obtained in the regular aCSF
214 with APs present (in this case) to the very end of the recording, where APs, mIPSPs and mEPSPs were
215 all blocked for some time ('noise-alone'). The data is shown after removing V_m segments containing
216 responses to regularly injected current pulses and has a total duration of 8520 s. Throughout the
217 entirety of this recording the baseline V_m varied between –70 and –67 mV and, thus remained
218 relatively stable.
219
220 There are three time markers that extend across all figure panels marking the time when the aSCF
221 containing TTX, gabazine, and CGP55845A was infused to block APs and IPSPs (the first marker), the
222 time when APs were observed to cease (the second marker), and the time when the aCSF containing
223 NBQX and CPP was infused to block remaining EPSPs (the third marker). The recording segment
224 between the second and the third markers constituted the 'noise with minis' recording, while the
225 segment following the third marker *after* mEPSPs were eventually blocked constituted the 'noise-
226 alone' recording. The darker yellow shaded regions that also extend across all panels of Figure 2
227 mark files (epochs) that were selected for subsequent minis distribution fitting.
228

229 The remaining panels of Figure 2 were used to guide data selection. The standard deviation (SD) of
230 the V_m (Figure 2B) was useful in determining the transitions between different pharmacological
231 conditions. Stable prolonged decreases in SD reliably indicated when APs or minis were effectively
232 blocked. Sudden brief increases in SD flagged problematic recording segments containing higher
233 levels of noise or V_m glitches. Gradual increases in SD suggested gradual deterioration of recording
234 quality.
235
236 Similar information was also provided by the evolution of the biggest 10% of amplitudes of all
237 detected minis-like events in a single sweep (Figure 2C). Prolonged drop in the amplitudes marked
238 transitions between recording conditions, while sudden jumps were indicative of V_m instabilities.
239 Finally, effective decay time constants of biggest 10% of detected events (Figure 2D) could be used
240 as an indicator for the presence/absence of minis. Blocking minis resulted in time constants
241 becoming large and fluctuating unstably, indicating that only noise fluctuations were being detected
242 that did not possess the typical decay dynamics common to EPSPs.
243
244 Further insights into the recording quality over time were provided by V_m responses to brief current
245 pulses. Passive membrane time constant measurements over time (Figure 2E) were expected to
246 remain stable. Deviations from this could signal a change in passive membrane properties due to
247 degradation in the recording quality. Total membrane capacitance (Figure 2F) was also expected to
248 be stable over time. Change in the capacitance could indicate membrane tearing, patch-resealing or
249 pipette movement or clogging, loss of membrane or part of the cell or some substantial uncontrolled
250 destabilisation of the recording. Finally, change in input resistance (detected from a change in the
251 bridge balance error; Figure 2G) was not permitted to exceed the balance error estimated offline at
252 the beginning of the recorded data by more than two-fold. Violation of this rule of thumb indicated a
253 deterioration in the recording quality potentially resulting from debris accumulating in the recording
254 pipette, movement of the pipette tip or the recorded cell body, partial formation of a membrane

'tube' (similar to what would happen in the process of producing an outside-out patch by slowly retracting the pipette), or other reasons.

We obtained the seven longitudinal recording state/quality indicators described above for all our recordings. Multi-panelled graphs showing these indicators for each individual recording separately are provided in Supplementary Figures 1-13.

Simulations

Simulating distributions of miniature excitatory postsynaptic potentials with a range of amplitudes and rise times

All simulations were carried out using our 'minis' software, developed in Matlab (Mathworks; RRID:SCR_001622), and performed on the Cardiff School of Biosciences' Biocomputing Hub HPC/Cloud infrastructure. Simulation of minis-like events was based on an analytical solution to the passive cable equation for a transient current (Rall, 1977) using 100 lumped terms with a double exponential synaptic current with τ_1= 0.15-3 ms (optimised in each instance/iteration) and τ_2 = 2 ms (Major et al., 1993). The detailed description of how arbitrary shape PSPs were obtained is provided in our companion article (Dervinis and Major, 2024).

A pool of simulated events was generated combining four bivariate (two-dimensional: amplitude and 10-90% rise time) normal distributions. Six parameters described each distribution: amplitude mean μ_X and standard deviation σ_X, 10-90% rise time mean μ_Y and standard deviation σ_Y, a correlation (or rotation) factor ρ, and a (relative frequency or number) scale factor n:

$$f(x,y) = \frac{n}{2\pi\sigma_X\sigma_Y\sqrt{1-\rho^2}} e^{-\frac{1}{2(1-\rho^2)}\left(\left(\frac{x-\mu_X}{\sigma_X}\right)^2 - 2\rho\left(\frac{x-\mu_X}{\sigma_X}\right)\left(\frac{y-\mu_Y}{\sigma_Y}\right) + \left(\frac{y-\mu_Y}{\sigma_Y}\right)^2\right)}.$$

All distribution parameters were controlled by the GA.

Fitting distributions of detected real mini-like events

The Matlab ga() function was used to control 24 parameters describing Four (rotated) bivariate normal distributions (6 parameters per distribution). Additional controlled parameters were the synaptic rise time constant τ_1 which ranged between 0.15 and 3 ms and the passive membrane time constant τ_m. The range for the latter constant was taken to be between 0.9 times and 1.1 times the initial estimate based on the averaged waveform of all minis-like events detected in the 'noise with real minis' recording. Thus, there were 26 parameters in total, controlled by the GA.

The GA would start by generating multiple distributions of simulated minis or smEPSPs (i.e. 'individuals'; we used 260 individuals per 'generation' with 10 individuals per parameter optimised by the GA; see a single run structure in Figure3A). Events would be drawn pseudo-randomly from a distribution and then simulated events of the chosen shapes (in terms of amplitude and 10-90% rise time) would be added to the 'noise-alone' recording at times that were also chosen pseudo-randomly (Figure 1). For generating the initial set of individuals ('population'), the GA chose parameters pseudo-randomly within prescribed ranges. For each of the four bivariate normal distributions the parameter ranges were as follows: μ_X (-0.1-1 mV), σ_X (0.01-1 mV), μ_Y (-1-10 ms), σ_Y (0.25-10 ms), ρ (-1 to 1), and n (0-10,000 for the first distribution and –10,000 to 10,000 for the remaining three distributions; negative counts were used for 'sculpting' the base distribution). Any negative count bins within the resulting final distribution were zeroed out. Any events with negative rise times or amplitudes below the simulation threshold (varying non-negative value) were excluded.

Next, the GA assessed the 'fitness' of each individual in the generation by using the cost function (explained in the next subsection). The top 5% of the most fit individuals survived to the next generation without change, while individual 'crossover' ('recombination'), genetic migration, and other GA parameters were set to default values of the Matlab ga() function. A new evolved generation of individuals was then created, which then served as the basis for yet another

306 generation and so on. This process (a single run in Figure 3A) was repeated until an 'individual' was
307 created with the lowest cost (highest fitness value) possible, or there was no improvement in the
308 fitness for 100 consecutive generations, or the number of generations reached 1000 (Figure 3A).
309
310 In cases where the GA terminated without converging on the highest fitness value, the distribution
311 fitting procedure was reinitiated using the most fit individual as a seed (Runs 2 and 3 in Figure 3B).
312 The population genetic diversity was reset by setting the GA-controlled parameter ranges to ±25% of
313 the original ranges relative to the seed parameter values, to explore the space around the current
314 best seed values. The re-running of distribution fitting was repeated until the GA converged to an
315 'apparently fittest possible individual' (or the 'best fit possible/achievable'; defined in the next
316 subsection), or otherwise an 'acceptable' level of fitness was reached (also defined in the next
317 subsection), or there was no improvement in fitness compared to the previous run for two
318 consecutive runs while an 'acceptable' fit was not yet attained (Figures 3B and C). In the latter case,
319 the entire distribution fitting procedure was reinitiated starting with a high simulated amplitude
320 lower limit (e.g., 200 μV), with the limit being gradually lowered until the 'best possible' or
321 'acceptable' fit was attained (Figure 3D). This 'backwards' ('downwards') fitting procedure was
322 required for several recordings having a large mean amplitude which, when we started with a low
323 simulated amplitude lower limit, failed to converge to an acceptable fit.
324
325 If the most fit individual was within acceptable levels of fitness values, the lower threshold on
326 smEPSP amplitude was increased by 10 μV (Figures 3B and C) (or lowered during the 'backwards' i.e.
327 'downwards' fitting procedure if no 'acceptable' fit was obtained; Figure 3D) and the entire fitting
328 step was re-run. This was repeated until the GA stopped converging (or started converging during
329 the 'backwards'/'downwards' fitting procedure) on a solution with acceptable fitness values.
330

331 The reason for attempting to push up the lower limit of the amplitudes of the smEPSPs is that it
332 became obvious that GA-generated solutions were not unique. Given an acceptable fit, matching the
333 histograms of events detected from the 'noise with real minis' recording can generally be achieved
334 by using distributions with a larger number of smaller amplitude smEPSPs, which get 'lost' in the
335 noise or summate with other smEPSPs, although the distribution of bigger smEPSPs is more tightly
336 constrained. (Indeed, one can also often (but not always) achieve acceptable fits with *fewer* small
337 amplitude smEPSPs (Supplementary Figure 14)). There is large number of such distributions with
338 ever-decreasing amplitudes of smEPSPs (in theory, all the way down to events resulting from brief
339 single AMPAR or NMDAR channel sub-conductance state openings, injecting undetectably small
340 amounts of charge). Therefore, the GA with the thresholding procedure described above has no
341 guaranteed way of arriving at the true distribution of minis, only at a distribution giving an
342 approximate *upper bound* on the *mean* (or median) mini amplitude – unless further biological
343 constraints are imposed.
344
345 *Cost function*
346 The goal of the minis distribution fitting procedure was to match 'noise with simulated minis' and
347 'noise with real minis' recordings as closely as possible, in terms of the distribution of amplitudes
348 and 10-90% rise times of detected mini-like events in the two types of V_m recording traces
349 ('simulated' vs. 'real' distributions), in the process 'cancelling out' any systematic errors in
350 amplitudes or shapes introduced by the detection algorithm or the summation or superposition of
351 events. This was achieved by minimising the cost function using the GA. The cost function was
352 composed of four types of components: *shape constraints* on the *simulated* minis distribution, *sums*
353 of *absolute* deviations (SADs) between 'simulated' and 'real' distributions, *sums* of *signed* deviations
354 (SSDs) between 'simulated' and 'real' distributions, and *maximal absolute* deviations (MADs)
355 between 'simulated' and 'real' distributions (Figures 4A and B). We avoided using the sum of
356 squared errors (SSE) because it is sensitive to outliers (giving them undue weight).

We calculated the typical ranges of SADs and MADs for each of the 14 recordings by taking the individual 'noise with real minis' recording and dividing it into smaller files (range was 15-606 files), each the duration of a single recording sweep (20 s, typically). Each file in this set was subjected to the minis detection procedure resulting in a set of 'real' (detected mini-like events) distributions. These were then subtracted from each other, in all pairwise combinations, and the corresponding SAD (sum of absolute deviations) and MAD (maximum absolute deviation) scores were calculated for each of the possible n*(n-1)/2 file pairings (range 105 to 183315, corresponding to 15 to 606 available files, respectively). Six SAD- and six MAD-based scores were calculated based on: distributions of amplitudes of (1) *all* detected events, (2) the largest 50%, (3) the largest 10% and (4) the largest 2% of detected events, (5) distribution of all 10-90% rise times, and (6) a joint amplitude and 10-90% rise time distribution. Three different SSD (sum of signed deviations)-based scores were calculated based on the amplitudes of (1) the largest 50%, (2) the largest 10%, and (3) the largest 2% of detected events. These latter scores constrained high-amplitude (but low count) tails of 'simulated' distributions to have sufficient counts to avoid negative distribution deviations ('simulated' – 'real').

To ensure good fits to *all* portions of the histograms, and to prevent 'dilution' or 'swamping' effects on the high amplitude (but low event frequency) tail by the low amplitude, high frequency 'hump', the smallest 'global' percentile (same for every measure) was estimated, that guaranteed to include *half* of all single-sweep file pairings (real vs. real data) with *all* their 15 respective SAD, MAD, and SSD score values falling below this percentile threshold *simultaneously* ('15-score combined 50th centile'; Figure 5 and Tables 1 and 2). This centile estimate was used to determine cut-off values for all these 15 different scores, to construct the optimisation cost function. The 'global' centile value from single sweep file comparisons was then used with SAD and MAD scores from longer files during the GA-

382 controlled fitting procedure (typically 5 recording sweep-long files to match the size of the 'noise-
383 alone' recording files, 100 s typically).
384
385 The cost function was constructed of 6 types of SAD scores and 6 types of MAD scores estimated
386 using the '15-score combined 50th centile' procedure and 3 types of SSD scores. These 15 scores
387 were used to evaluate how close the 'simulated' distribution was to the single selected 'real'
388 distribution that was deemed to be of the best quality by a human observer (Figures 4A and B).
389 Typically, it was a file close to the *end* of the 'noise with minis' recording epoch, therefore, being the
390 most similar file, in terms of recording quality parameters, to the 'noise-alone' recording epoch
391 (which was generally the *first* good-quality epoch safely *after* pharmacological blockade of
392 neurotransmission was deemed complete). An additional corresponding 15 'envelope deviation'
393 scores (same as SADs, MADs, and SSDs but comparing to the envelope or lower and upper range
394 limits of superimposed all available data distributions within that pharmacological epoch) were
395 calculated assessing how much each 'real' or 'simulated' distribution deviated from the full set
396 consisting of all the remaining 'real' distributions and the single 'simulated' distribution (Figures 4C
397 and D). The 'simulated' distribution was expected to have lower deviation scores than the worst
398 performing (most discrepant from the others) 'real' distribution (so the simulated distribution would
399 not be picked as the 'worst outlier' by a double-blind observer).
400
401 'Simulated' distributions were further penalised if their underlying source 'simulated minis'
402 distribution was non-unimodal, had a 10-90% rise time mean larger than 5 ms, or it violated a 10-
403 90% rise time skewness constraint that the mean 10-90% rise time of simulated minis should exceed
404 the median at least by a quarter of the standard deviation, as seen for the real minis (with noise)
405 distributions (range of 0.25 to 0.39 standard deviations). Finally, 'simulated' distributions were also
406 penalised if their underlying 'simulated minis' amplitude distribution had a sharp cliff at its lower

end. Hence, together with the four shape constraints there were 34 fitness components in total (15 + 15 + 4 = 34).

If all SAD, MAD, SSD, deviation scores, and shape constraints for comparing the 'simulated' distribution to the 'real' distributions were satisfied (≤ 15-score 50th centile SAD and MAD cutoff values and ≥0 SSD values) at the end of the fitting procedure, the fit was deemed to be the 'best possible' (a 'very good match', by all criteria). Alternatively, the fit could also be deemed 'acceptable' if all amplitude SAD, MAD, and SSD scores, as well as the distribution unimodality constraint were satisfied (excluding 10-90% rise time scores, all 'envelope deviation' scores, and the distribution skewness and 'cliff' constraints). The 'best' and 'acceptable' fits comprised the set of 'good enough' fits in terms of their GA-optimised 'fitness' which, however, did not guarantee a statistically acceptable fitness.

Final test for distribution acceptance or rejection

The notion of a 'good enough' fit is somewhat arbitrary, so far. Once the fitting procedure was completed, we set out to check whether the final fit was objectively acceptable using statistical tests. We divided the full available length of the 'noise with real minis' recording condition (epoch) into smaller files of the same length as the selected 'noise-alone' recording file and constructed a *set* of (independent) 'real' ('noise with real minis') distributions (histograms) by running the 'minis' detection algorithm on all these files (which we term the 'real distribution set'). We then compared these individual 'real' distributions to each other, pairwise, by subtracting their marginal ('1-D') amplitude and 10-90% rise time distributions from each other, taking the absolute value of the differences, and summing over all bins (bin sizes of 10 µV and 0.5 ms; bin counts were normalised by the average bin count over all 'real' distributions to increase the weight of distribution tails). So we ended up with amplitude (Figure 6A) and 10-90% rise time (Figure 6B) sets of SAD scores for each distribution (individual file) within the 'distribution set' (the 'real-real SAD score sets'; there is an

amplitude and a rise time 'real-real SAD score set' for each distribution within the 'distribution set' corresponding to individual lines in Figures 6A and B). The number of SAD scores in each 'real-real SAD score set' corresponded to the number of possible comparisons between the distribution (file) of interest and the rest of the distributions (files) = n - 1 (given n different files). Finally, we selected the 'worst' ('most discrepant') and the 'best' ('least discrepant' compared to the others) 'real' reference distributions (files; the top and the bottom rows of SAD score matrices in Figures 6A and B, respectively), in terms of their median SAD scores (median over all SADs in the 'real-real SAD score set' for that distribution). Therefore, we were left with only two sets: The 'worst real-real SAD set' and 'the best real-real SAD set'.

We also compared the 'good enough so far' ('work-in-progress') 'noise with simulated minis' distribution to all the non-reference 'real' ('noise with *real* minis') distributions. The comparison yielded another set of SAD scores: the 'simulated-real SAD score set' (Figures 6C and D). The median of this was then compared to the medians of the 'worst real-real SAD score set' and the 'best real-real SAD score set' using the non-parametric Wilcoxon signed-rank paired samples test. If the median score of the 'simulated-real SAD score set' was significantly larger than the median score of the '*worst* real-real SAD score set', (i.e. if the distributions actually were identical, that discrepancy or more would only have occurred purely by chance less than 5% of the time; Bonferroni-corrected for a requirement to simultaneously satisfy both amplitude and 10-90% rise time tests), the 'simulated' distribution was deemed to be an inadequate fit and, was therefore rejected and the fitting procedure continued. (By contrast, if the median score of the 'simulated-real SAD score set' was significantly *smaller* than the median score of the '*best* real-real SAD score set', the 'simulated' distribution was deemed likely to be an "excellent" fit; however, 'passing' this test was not strictly required and was used only for guidance). The 'work-in-progress' 'good enough' fit was ultimately accepted if the median of the 'simulated-real SAD score set' was *not* significantly larger than the median of the 'worst (most discrepant) real-real SAD score set'. Intuitively, this corresponds

459 (roughly) to a double-blind observer not being able to pick out that (simulated minis with real noise)
460 distribution (histogram) from the (real minis with real noise) data distributions (histograms): it was
461 not (obviously) the 'most discrepant' histogram.
462
463 **Statistical analyses**
464 Parametric inferential statistics tests were used for incidence rates of minis (frequencies minis/s),
465 mean amplitudes, and total cell membrane capacitances, as quantile-quantile ('Q-Q') plots indicated
466 that these measures were normally distributed. Sums of absolute distribution bin deviations (SADs)
467 were often not normally distributed as assessed by Q-Q plots, and therefore were tested using the
468 corresponding non-parametric paired samples Wilcoxon signed-rank test.
469
470 **Data accessibility**
471 All data analysed in this study are publicly available (Dervinis, 2024a, 2024b). The available data
472 include 'noise with minis' and 'noise-alone' whole-cell patch membrane potential recordings that
473 were used in computer simulations and minis' distribution fitting, as well as GA distribution fitting
474 results. All electrophysiological recordings were stored in Axon Binary File (ABF) format.
475
476 **Code accessibility**
477 All analyses were carried out in Matlab and the analysis code is publicly available on GitHub
478 (Dervinis, 2024c). The code is complete with instructions on how to reproduce figures reported in
479 this study.
480
481 **Software accessibility**
482 The present study reported the use of a novel quantal analysis method that is part of 'minis'
483 software available on GitHub (Dervinis, 2024d).
484

Results

Estimating quantal size by direct subtraction of noise component

We have analysed 'noise with minis' recordings and 'noise-alone' recordings with the 'minis' detection algorithm. Detected mEPSP-like events had an amplitude and 10-90% rise time distributions that resembled log-normal or gamma distributions (Figure 7), left skewed with a long tail on the right. In the amplitude domain, the lower end of the distribution contains a mixture of real minis and noise fluctuations that were misidentified as real events (but also missing small minis cancelled out by noise, summating with larger minis, or failing to be detected due to being on a decay phase of a big preceding mini – the 'overshadowing' effect).

We initially tested whether the noise component (in 'noise with minis' recordings) could be reliably estimated based on the corresponding 'noise-alone' recording (where synaptic activity has been pharmacologically blocked), simply by directly subtracting the detected 'noise-alone' events distribution from the 'noise with minis' distribution, to yield an estimate of the pure minis' component. Figure 7A shows both 'noise with minis' and 'noise-alone' detected event amplitude distributions superimposed. After subtracting the 'noise-alone' distribution from the 'noise with minis' distribution there appear negative low amplitude bins in the resulting distribution (indicated by an arrowhead in Figure 7A). These missing low amplitude events are caused by a greater number of small false positive mini-like detections in the noise-alone traces, and larger minis overshadowing smaller minis and small amplitude noise fluctuations in the 'noise with minis' recording (we have discussed this phenomenon in more detail in our companion article (Dervinis and Major, 2024)). Therefore, the direct subtraction approach can only provide a relatively crude 'first order', high-end upper limit on the mean of the mini amplitude distribution. Nevertheless, this over-estimate is more reliable than a highly subjective approach of simply estimating the mean amplitude based on events detected using a high amplitude threshold, or worse still, detected manually, by what could, perhaps

uncharitably, be termed a “beauty contest” method (rather arduous, slow, subjective, and prone to human error/bias).

Estimating quantal size by simulating excitatory postsynaptic potential source distributions

An alternative and more reliable way of estimating the quantal size in our recordings is to estimate the minis component directly using simulations. This relies on the ‘minis’ optimisation algorithm (GA) being able to closely match a ‘noise with simulated minis’ voltage trace (Figure 3) with the ‘noise with real minis’ recordings in terms of amplitude and 10-90% rise time distributions of minis-like events detected within these traces. We were able to successfully do that for all our recordings (see Figure 8 and Supplementary Figures 15-27). In the example shown in Figure 8, the overall amplitude SAD of the ‘simulated’ distribution was not significantly larger than the worst-performing ‘real’ distribution (unidirectional ‘underfit’ test: Is ‘simulated’ median SAD significantly > worst-performing ‘real’ median SAD? Wilcoxon signed-rank paired samples test statistic $W (n = 16) = 105$, $p = 0.058$ (Bonferroni-corrected due to comparing once on amplitudes and once on rise times); a high W statistic indicates a high absolute distance between the two medians, irrespective of its sign/direction, while $p < 0.025$ would indicate fit rejection, due to a fit SAD score being larger than the worst SAD score than would be expected by chance alone, at that significance level; downward arrow indicates ‘simulated’ median SAD < ‘real’ median SAD relationship in Figure 8) and was not outperforming the best ‘real’ distribution (‘simulated’ median SAD < best-performing ‘real’ median SAD Wilcoxon signed-rank paired samples unidirectional ‘overfit’ test $W(16) = 135$, $p = 1$; upward arrow indicates ‘simulated’ median SAD > ‘real’ median SAD relationship in Figure 8). Similarly, the ‘simulated’ 10-90% rise time distribution was also neither an underfit (‘simulated’ median SAD > worst-performing ‘real’ median SAD unidirectional ‘underfit’ test $W(16) = 0$, $p = 1$) nor an overfit (‘simulated’ median SAD < best-performing ‘real’ median SAD unidirectional ‘overfit’ test $W(16) = 117$, $p = 1$).

536 All simulations produced ‘good enough’ matches showing amplitude and 10-90% rise time
537 distributions of detected minis-like events being within the range of (and thus indistinguishable
538 from) amplitude and 10-90% rise time count values measured in sets of ‘real event’ distributions
539 (Supplementary Figures 15-27). None of the fits performed significantly worse than the worst-
540 performing ‘real’ distribution, qualifying them as ‘good enough’ (accepted) fits. All resulting minis
541 source distributions are displayed in Figure 9 and Supplementary Figures 28-40. An example in
542 Figure 9 shows that the ‘real minis’ source distribution likely has a log-normal or gamma-like shape
543 in both amplitude and rise time domains.
544
545 Incidence rates (frequencies of minis per second) estimated based on simulated minis source
546 distributions ranged roughly between 10 and 100 minis/s (a mean of 27.3 ± 2.4 minis/s and a range
547 of 6.8 to 58.1 minis/s; Figure 10). This estimate is an order of magnitude higher than the one based
548 on the literature (3.6 minis/s; (Dervinis and Major, 2024)) and significantly higher than the one based
549 on the direct subtraction method (15.9 ± 0.9 minis/s; $t(13) = 3.51$, $p = 0.004$) and also higher than
550 the estimate based on amplitudes higher than a (deliberately chosen) unrealistically high detection
551 threshold of 0.8 mV (14.3 ± 0.9 minis/s; $t(13) = 3.69$, $p = 0.003$). It is precisely within the range
552 predicted in our companion article (Dervinis and Major, 2024). However, this range is possibly still
553 somewhat of an underestimate, as mini source distributions were often generated using a lower
554 limit on simulated amplitudes to constrain the distribution non-uniqueness, as discussed in the
555 Methods subsection on the distribution fitting (also see Supplementary Figure 14).
556
557 Mean amplitudes of minis derived using simulations ranged between 53 and 182.9 μV (overall mean
558 of 114.1 ± 5.5 μV, layer 2/3 mean of 133.1 ± 9.9 μV, and layer 5 mean of 95.1 ± 11.2 μV; Figure 11A).
559 When compared to capacitance estimates (or 1/capacitance), there was a strong (very tight)
560 correlation between each cell’s mean mEPSP amplitude and the inverse of its capacitance (which is
561 proportional to cell size, assuming capacitance per unit area is more or less a biological constant for

562 each cell class/type of membrane/density of channels with charged gates moving within the
563 membrane (Gentet et al., 2000); $r = 0.96$, $p = 7.1 \times 10^{-8}$, $R^2 = 0.92$). That is, the larger the cell, the
564 smaller the amplitude of its somatically detected minis and vice-versa. This relationship is predicted
565 by the theory of capacitors ($C = Q/V$, where C stands for capacitance, Q stands for charge, and V
566 stands for voltage across the cell's membrane), and it is a direct demonstration of an attenuating
567 effect of cell's capacitance on the amplitude of somatically detected minis. If a direct line was drawn
568 through the data and the origin of the axes in Figure 11A, the slope of this line would provide a
569 quantal size estimate for excitatory synapses in the CNS in terms of 'injected' charge ($Q = \Delta V/$
570 $\Delta(1/C)$) which is approximately equal to 31.3 fC, for these data. The fact that the least square fitted
571 line to the data ($y = 30.6x + 2.76$), with a negligibly small intercept term (2.76), roughly coincided
572 with the line through the origin fitted to the data ($y = 31.3x$) indicated that no obvious 'proactive'
573 mechanism *varying with cell size* was in place to compensate for the attenuation of the average
574 minis' amplitude due to the size of the cell.
575
576 Another notable observation was that the mean amplitude estimates derived either by noise
577 subtraction or by minis source distribution simulation were highly correlated ($r = 0.84$, $p = 1.49 \times 10^{-4}$,
578 $R^2 = 0.71$ Figure 11B). The equation of the line ($y = 1.37x – 65.9$) fitted to this data provides a
579 possible "shortcut" method to approximate the mean amplitude of fitted minis' source distribution
580 by inserting the mean estimated using 'naïve' noise subtraction directly into this equation.
581
582 *Generic miniature excitatory postsynaptic potential distribution in neocortex*
583 To construct a generic mEPSP distribution, we normalised amplitudes of simulated minis' source
584 distributions shown in Figure 9 and Supplementary Figures 28-40 by dividing them by their
585 respective means, taking the total average, and then scaling the amplitudes to the overall mean
586 (114.1 ± 5.5 μV). The resulting combined (amplitude and 10-90% rise time) distribution is shown in
587 Figures 12A and B. The corresponding marginal amplitude and 10-90% rise time distributions are

588 shown in Figures 12C and D, respectively. Both marginal distributions have left-skewed log-normal-
589 like or gamma-like distributions. This may be useful in neural network simulations, or to potentially
590 speed up (and constrain) fitting of simulated minis on noise to real minis with noise, using the GA
591 (e.g., limit the source distribution to one 2-D 'rotated' log-normal or gamma distribution).
592

593 # Discussion

594 We report two major scientific advances. First, a novel quantal analysis method based on sequential
595 somatic recording, from a given neuron, of a) mEPSPs (after blockade of action potential-mediated
596 neurotransmission, and all inhibitory neurotransmission, including mIPSPs) on a background of other
597 physiological noise, and b) subsequent recordings from the same cell of noise alone, after additional
598 pharmacological blockade of mEPSPs (all glutamatergic ionotropic excitatory neurotransmission).
599 The latter type of recording provides a means to estimate the properties of the noise component
600 which can then be used to take into account noise fluctuations in the combined minis and noise
601 recording. However, this was done not by a direct subtraction of the histogram of amplitudes
602 (and/or rise times) detected from the noise-alone recordings, but rather by the simulation of the
603 underlying minis component and repeatedly superimposing (at random) the waveforms of simulated
604 minis onto the noise trace, varying source distribution parameters until the histograms detected
605 from the 'noise with simulated minis' voltage trace closely matched those detected from the 'noise
606 with real minis' recording. The key tool for achieving this match was a genetic algorithm that
607 optimised the parameters of the 2-dimensional simulated minis distribution in terms of amplitudes
608 and 10-90% rise times (and rate, i.e. minis per second), simultaneously, to best fit the experimental
609 data distributions.
610

611 The second major advance was the application of our novel quantal analysis method, that
612 successfully measured the mean 'electric charge injected' size of excitatory synapses of cortical

613 pyramidal cells, which was shown to be approximately 31.3 fC, across the entire sample of
614 neocortical pyramidal neurons recorded. This number was inferred from the slope of the line which
615 tightly fitted mean mini amplitude vs. 1/total cell capacitance, in accordance with the theory of
616 capacitors. The fact that this line had an intercept at the origin of the axes indicated that there was
617 no biological compensation (other than *number* of synapses) for the amplitude attenuation of minis
618 due to cell size (i.e., total capacitance). Indeed, cell capacitance played a major role affecting the
619 *voltage* amplitude of mEPSPs, resulting in a large proportion of mEPSPs being otherwise
620 indistinguishable from noise (as independently found in numerous other studies, e.g. (Major et al.,
621 2013b; Nevian et al., 2007), summarised in (Major et al., 2013b)). The number of these 'missed'
622 minis was so high that the estimated minis' incidence rate (frequency) was in the order of 10-100
623 minis/s: an order of magnitude higher than typically reported in the synaptic physiology literature
624 (with the notable exception of (Nevian et al., 2007), which predicted this result, by simultaneous
625 dual somatic and basal dendritic whole-cell patch recordings of mEPSPs, with dendritic detection,
626 and simultaneous somatic measurement). Finally, both the amplitude and 10-90% rise time
627 distributions of minis had a left-skewed log-normal- or gamma-like shape.
628
629 These findings have some major implications. First, the method, as used for estimating the mEPSP
630 distributions in cortical layers 2/3 and 5 of cells of various size, and then using these distributions to
631 arrive at the electrical size of excitatory synapses, serves as a proof of principle that it can be
632 successfully used to estimate PSP distributions of various types in the CNS. The next logical step of
633 this method is to extend its application to the estimation of amplitude and rise time distributions of
634 mIPSPs generated by different types of inhibitory synapses and, as a result, their 'electrical sizes'.
635 Moreover, the ability to obtain relatively accurate 'quantal' size estimates unobscured by
636 physiological noise is important for constraining synaptic parameters in physiologically realistic
637 simulations of neural activity. For example, now we should be able to better estimate how many
638 active synapses are needed to generate an NMDA spike within a single dendritic segment (Major et

al., 2013b). The importance of these number estimates is not restricted to the domain of physiologically realistic simulations but also extends to more abstract computations that use NMDA spike-like mechanisms as coincidence detectors in the latest cortically inspired/constrained models of artificial intelligence (Hawkins et al., 2019). Accurate estimates of synaptic transmission parameters thus have very wide-reaching ramifications.

These findings also draw attention to some possible methodological issues in the field of synaptic physiology. As discussed in our companion article (Dervinis and Major, 2024), the reported incidence rates ('frequencies') for mEPSCs are generally well below 10 minis/s. Even if one doubts the incidence rates we arrived with simulations, in the range of 10-100 minis/s, the rates given by 'naïve' direct subtraction of the distribution of events detected in the 'noise-alone' recording from the distribution based on the 'noise with minis' recording is still within 5.9 to 26.7 minis/s, which we know to be an underestimate. Therefore, reported mini incidence rates below 10 minis/s are almost certainly underestimates. This may have multiple causes, including lower slice temperatures in the majority of studies (we used physiological, ca. 37 °C), and a significant temperature dependence of synaptic release, as well as differences in slice health and slicing angle (which can affect branch and local circuit 'amputations'). Another big cause could be the use of voltage clamp, especially if the series resistance is not compensated fully, as this low-pass filters traces and obscures smaller minis. As discussed earlier, these estimates could be improved by switching to voltage recording instead of using voltage clamp (Major, 1993a; Rall and Segev, 1985; Spruston et al., 1993; Williams and Mitchell, 2008) but at the price of somewhat slower decay times of minis (Major 1993), thus more temporal overlap/integration and consequent difficulties detecting peaks. But more importantly, a strong association between cell capacitance (i.e. surface area) and the extent to which somatically recorded minis' amplitudes are attenuated, indicates that special care must be taken to account for the effect of background noise fluctuations on the amplitude measurements - as we have done here. This association is yet more evidence supporting experimental observations of massive mini

665 amplitude attenuation as the PSP spreads from its dendritic source location to the soma (Larkum et
666 al., 2009; Major et al., 2013a; Nevian et al., 2007; Stuart and Spruston, 1998; Williams and Mitchell,
667 2008; Williams and Stuart, 2002), especially in cells with large dendritic arbours, hence large surface
668 areas and overall membrane capacitance. Dendritic spines and post-synaptic densities (the
669 specialised regions opposite release sites, containing high densities of synaptic receptors, with a
670 substantial fraction tethered to the cytoskeleton) are not grossly different in size between different
671 classes of pyramidal neurons in the neocortex, although differences exist between cortical layers,
672 cortical areas, and, particularly, species (Yuste, 2010).
673
674 It is also worth noting that understanding the link between cell capacitance and somatically
675 recorded average mini amplitudes, as well as knowing actual shapes of mini distributions in terms of
676 their amplitudes and rise times, allows us to generate artificial data where the 'ground truth' is
677 known. Such labelled data could perhaps be used to train artificial neural networks (ANNs) which
678 could then be used to develop 'next generation' quantal analysis methods allowing detection of
679 minis directly in mixed 'noise with minis' recordings. We are not the first to suggest the application
680 of ANNs to this issue (see (Pircher et al., 2022) and (Wang et al., 2024)). However, we are not aware
681 of attempts to use realistic mini distributions for this purpose.
682
683 Even though the novel quantal analysis method we present here is an important advance, it
684 nevertheless has limitations. One of them is the need for (relatively) long duration recordings using
685 different pharmacological agents at various stages. However, the somatic recording set up is not as
686 complicated and high-skill as an alternative multisite 2-photon targeted dendritic recording set up
687 would be (Nevian et al., 2007), a heroic technique which has not to our knowledge been reproduced
688 in another lab. Experiments themselves could be further streamlined, as we did in some cases, by
689 pre-blocking action potentials before obtaining the whole-cell recordings, and using high solution
690 perfusion rates. This is particularly useful for smaller cells which are more prone to osmotic

691 overloading or shrinkage and resulting recording instability after a few tens of minutes (the pipette
692 solution cannot exactly reproduce the cytoplasm, as it contains no proteins or other
693 macromolecules, and is missing many common metabolites). Moreover, the distribution fitting
694 procedure involving the GA can be lengthy and computationally intensive. However, the 'minis'
695 software is parallelised at the PSP detection level, as well as at the GA optimisation level, making it
696 particularly suitable to be executed on multi-core computing clusters. Although our 'minis' software
697 combined with two-stage recordings offers unprecedented control for the background physiological
698 noise, provided recording stability is very good throughout, we understand that many researchers
699 may not be persuaded to adopt it themselves. The possibility of misleading fits if the recording noise
700 became substantially worse between 'noise with minis' and 'noise-alone' recording phases needs to
701 be vigilantly excluded. Nevertheless, our 'minis' software should still be useful for detecting mini-like
702 events without recording independent noise, or fitting simulated to real distributions, if there is
703 some other credible cut-off or separation method that can be used to distinguish between small or
704 partially cancelled minis and mini-like noise. We anticipate, indeed, that, realistically, this scenario is
705 likely to be its most popular use.
706
707 Some researchers may be critical of a method that does not rely on a direct measurement of minis
708 but rather on an approximation via indirect means, using simulations. This is a valid criticism that
709 could (perhaps) be addressed in the future by using a method of repeatedly subjecting a voltage
710 recording to the minis detection procedure with an increasingly lower threshold while subtracting
711 detected events from the voltage recording, or perhaps compensating for the 'exponential-like'
712 decay phases of recent, temporally integrated, detected mini-like events. Some combination of
713 these approaches could potentially recover most of the smaller minis that are 'overshadowed' by
714 the larger ones (the so called 'negative bins' problem illustrated in Figure 7A), providing the
715 waveforms were reasonably stereotyped in shape (not the case under voltage clamp, in neurons
716 with large or extended or highly-branched dendritic arbours, (Major, 1993b)). Furthermore, other

717 researchers may question the ability to pharmacologically isolate the background physiological
718 noise. Our 'noise with minis' recordings may contain random openings of individual AMPA receptor
719 (AMPAR) or NMDA receptor (NMDAR) channels (possibly extra-synaptic) and our 'noise-alone'
720 recordings may fail to fully eliminate all channel openings in the presence of quantal release of
721 neurotransmitter (although we used high doses, well above IC50s' (Lehmann et al., 1987; Randle et
722 al., 1992) and rapid slice perfusion, to achieve quick wash-in times).
723 Background/physiological/electrical noise itself may also be drifting between two such (hypothetical)
724 conditions, with the presence or absence of mEPSP pharmacological blockers. Occasionally, we
725 rejected recordings (or epochs) with suspicious or obvious instabilities. These factors are unlikely to
726 have affected the results significantly, due to the small amplitudes of any remaining membrane
727 potential variations in the fitted cells. Two largely independent analyses of the same data by the two
728 authors separately yielded similar results and conclusions (albeit with somewhat different data
729 selection, sweep lengths, and tests of goodness of fits: the 'first pass', not presented here, relied
730 more on 'double-blind' visual inspection of multiple real minis with noise data distributions from the
731 same cell superimposed on the simulated minis with noise fit distribution: if the latter stood out
732 obviously from the crowd, it was rejected).
733
734 Despite some of the limitations discussed above, the method and its application to neocortical
735 excitatory connections presented in this article provide a useful advance in the field of synaptic
736 physiology. Logical next steps could include the application of this novel quantal analysis method to
737 establish the properties of other types of excitatory synapse, and various types of inhibitory synapse,
738 in both neocortex and hippocampus, and in other species, and to investigate whether average
739 synaptic 'size' (injected charge) is more widely conserved within different cell classes.

References

Bekkers JM. 1994. Quantal analysis of synaptic transmission in the central nervous system. *Curr Opin Neurobiol* **4**:360–365. doi:https://doi.org/10.1016/0959-4388(94)90097-3

Biró ÁA, Holderith NB, Nusser Z. 2005. Quantal Size Is Independent of the Release Probability at Hippocampal Excitatory Synapses. *The Journal of Neuroscience* **25**:223–232. doi:10.1523/JNEUROSCI.3688-04.2005

Brown TH, Wong RKS, Prince DA. 1979. Spontaneous miniature synaptic potentials in hippocampal neurons. *Brain Res* **177**:194–199. doi:https://doi.org/10.1016/0006-8993(79)90931-4

Clamann HP, Rioult-Pedotti MS, Luscher HR. 1991. The influence of noise on quantal EPSP size obtained by deconvolution in spinal motoneurons in the cat. *J Neurophysiol* **65**:67–75. doi:10.1152/jn.1991.65.1.67

Clements JD. 2003. Variance–mean analysis: a simple and reliable approach for investigating synaptic transmission and modulation. *J Neurosci Methods* **130**:115–125. doi:https://doi.org/10.1016/j.jneumeth.2003.09.019

Clements JD, Silver RA. 2000. Unveiling synaptic plasticity: a new graphical and analytical approach. *Trends Neurosci* **23**:105–113. doi:10.1016/S0166-2236(99)01520-9

del Castillo J, Katz B. 1954. Quantal components of the end-plate potential. *J Physiol* **124**:560–573. doi:https://doi.org/10.1113/jphysiol.1954.sp005129

Dervinis M. 2024a. https://gin.g-node.org/dervinism/minis-benchmarking-data2. *GIN*. doi:10.12751/g-node.mvsy4j

Dervinis M. 2024b. https://gin.g-node.org/dervinism/minis-quantal-analysis-data. *GIN*. doi:10.12751/g-node.32m2ge

Dervinis M. 2024c. https://github.com/dervinism/minis-quantal-analysis. *GitHub*. doi:10.5281/zenodo.14288653

Dervinis M. 2024d. https://github.com/dervinism/minis. doi:10.5281/zenodo.14573132

Dervinis M, Major G. 2024. A novel method for reliably measuring miniature and spontaneous postsynaptic potentials/currents in whole-cell patch clamp recordings in the central nervous system. *bioRxiv*. doi:10.1101/2022.03.20.485046

Edwards FR, Redman SJ, Walmsley B. 1976. Statistical fluctuations in charge transfer at Ia synapses on spinal motoneurones. *J Physiol* **259**:665–688. doi:https://doi.org/10.1113/jphysiol.1976.sp011488

Enoki R, Hu Y, Hamilton D, Fine A. 2009. Expression of Long-Term Plasticity at Individual Synapses in Hippocampus Is Graded, Bidirectional, and Mainly Presynaptic: Optical Quantal Analysis. *Neuron* **62**:242–253. doi:10.1016/j.neuron.2009.02.026

Farsi Z, Walde M, Klementowicz AE, Paraskevopoulou F, Woehler A. 2021. Single synapse glutamate imaging reveals multiple levels of release mode regulation in mammalian synapses. *iScience* **24**. doi:10.1016/j.isci.2020.101909

Fatt P, Katz B. 1952. Spontaneous subthreshold activity at motor nerve endings. *J Physiol* **117**:109–128.

Forti L, Bossi M, Bergamaschi A, Villa A, Malgaroli A. 1997. Loose-patch recordings of single quanta at individual hippocampal synapses. *Nature* **388**:874–878. doi:10.1038/42251

Gentet LJ, Stuart GJ, Clements JD. 2000. Direct Measurement of Specific Membrane Capacitance in Neurons. *Biophys J* **79**:314–320. doi:https://doi.org/10.1016/S0006-3495(00)76293-X

Hardingham NR, Read JCA, Trevelyan AJ, Nelson JC, Jack JJB, Bannister NJ. 2010. Quantal Analysis Reveals a Functional Correlation between Presynaptic and Postsynaptic Efficacy in Excitatory Connections from Rat Neocortex. *The Journal of Neuroscience* **30**:1441–1451. doi:10.1523/JNEUROSCI.3244-09.2010

Hawkins J, Lewis M, Klukas M, Purdy S, Ahmad S. 2019. A Framework for Intelligence and Cortical Function Based on Grid Cells in the Neocortex. *Front Neural Circuits* **12**. doi:10.3389/fncir.2018.00121

Heuser JE, Reese TS, Dennis MJ, Jan Y, Jan L, Evans L. 1979. Synaptic vesicle exocytosis captured by quick freezing and correlated with quantal transmitter release. *Journal of Cell Biology* **81**:275–300. doi:10.1083/jcb.81.2.275

Isaacson JS, Walmsley B. 1995. Counting quanta: Direct measurements of transmitter release at a central synapse. *Neuron* **15**:875–884. doi:10.1016/0896-6273(95)90178-7

Jack JJ, Redman SJ, Wong K. 1981. The components of synaptic potentials evoked in cat spinal motoneurones by impulses in single group Ia afferents. *J Physiol* **321**:65–96. doi:https://doi.org/10.1113/jphysiol.1981.sp013972

Jonas P, Major G, Sakmann B. 1993. Quantal components of unitary EPSCs at the mossy fibre synapse on CA3 pyramidal cells of rat hippocampus. *J Physiol* **472**:615–663. doi:https://doi.org/10.1113/jphysiol.1993.sp019965

Katz B. 1969. The Release of Neural Transmitter Substances. Liverpool: Liverpool Univ. Press.

Korn H, Faber DS. 1991. Quantal analysis and synaptic efficacy in the CNS. *Trends Neurosci* **14**:439–445. doi:https://doi.org/10.1016/0166-2236(91)90042-S

Kraszewski K, Grantyn R. 1992. Unitary, quantal and miniature gaba-activated synaptic chloride currents in cultured neurons from the rat superior colliculus. *Neuroscience* **47**:555–570. doi:https://doi.org/10.1016/0306-4522(92)90165-X

Kullmann DM, Nicoll RA. 1992. Long-term potentiation is associated with increases in quantal content and quantal amplitude. *Nature* **357**:240–244. doi:10.1038/357240a0

Kuno M. 1964. Quantal components of excitatory synaptic potentials in spinal motoneurones. *J Physiol* **175**:81–99. doi:https://doi.org/10.1113/jphysiol.1964.sp007504

Larkman A, Stratford K, Jack J. 1991. Quantal analysis of excitatory synaptic action and depression in hippocampal slices. *Nature* **350**:344–347. doi:10.1038/350344a0

Larkum ME, Nevian T, Sandler M, Polsky A, Schiller J. 2009. Synaptic Integration in Tuft Dendrites of Layer 5 Pyramidal Neurons: A New Unifying Principle. *Science (1979)* **325**:756–760. doi:10.1126/science.1171958

Lehmann J, Schneider J, McPherson S, Murphy DE, Bernard P, Tsai C, Bennett DA, Pastor G, Steel DJ, Boehm C. 1987. CPP, a selective N-methyl-D-aspartate (NMDA)-type receptor antagonist: characterization in vitro and in vivo. *Journal of Pharmacology and Experimental Therapeutics* **240**:737–746.

Liu Z, Lu X, Villette V, Gou Y, Colbert KL, Lai S, Guan S, Land MA, Lee J, Assefa T, Zollinger DR, Korympidou MM, Vlasits AL, Pang MM, Su S, Cai C, Froudarakis E, Zhou N, Patel SS, Smith CL, Ayon A, Bizouard P, Bradley J, Franke K, Clandinin TR, Giovannucci A, Tolias AS, Reimer J, Dieudonné S, St-Pierre F. 2022. Sustained deep-tissue voltage recording using a fast indicator evolved for two-photon microscopy. *Cell* **185**:3408-3425.e29. doi:10.1016/J.CELL.2022.07.013

Major G. 1993a. Solutions for transients in arbitrarily branching cables: III. Voltage clamp problems. *Biophys J* **65**:469–491. doi:10.1016/S0006-3495(93)81039-7

Major G. 1993b. Solutions for transients in arbitrarily branching cables: III. Voltage clamp problems. *Biophys J* **65**:469–491. doi:10.1016/S0006-3495(93)81039-7

Major G, Evans JD, Jack JJ. 1993. Solutions for transients in arbitrarily branching cables: I. Voltage recording with a somatic shunt. *Biophys J* **65**:423–449. doi:10.1016/S0006-3495(93)81037-3

Major G, Larkum ME, Schiller J. 2013a. Active Properties of Neocortical Pyramidal Neuron Dendrites. *Annu Rev Neurosci* **36**:1–24. doi:10.1146/annurev-neuro-062111-150343

Major G, Larkum ME, Schiller J. 2013b. Active Properties of Neocortical Pyramidal Neuron Dendrites. *Annu Rev Neurosci* **36**:1–24. doi:10.1146/annurev-neuro-062111-150343

Nevian T, Larkum ME, Polsky A, Schiller J. 2007. Properties of basal dendrites of layer 5 pyramidal neurons: a direct patch-clamp recording study. *Nat Neurosci* **10**:206–214. doi:10.1038/nn1826

Oertner TG, Sabatini BL, Nimchinsky EA, Svoboda K. 2002. Facilitation at single synapses probed with optical quantal analysis. *Nat Neurosci* **5**:657–664. doi:10.1038/nn867

Peled ES, Isacoff EY. 2011. Optical quantal analysis of synaptic transmission in wild-type and rab3-mutant Drosophila motor axons. *Nat Neurosci* **14**:519–526. doi:10.1038/nn.2767

Pircher T, Pircher B, Feigenspan A. 2022. A novel machine learning-based approach for the detection and analysis of spontaneous synaptic currents. *PLoS One* **17**:1–16. doi:10.1371/journal.pone.0273501

Rall W. 1977. Core Conductor Theory and Cable Properties of Neurons In: Kandel ER, Brookhardt JM, Mountcastle VM, editors. Handbook of Physiology, Cellular Biology of Neurons. Bethesda, MD: American Physiological Society. pp. 39–97.

Rall W, Segev I. 1985. Space-clamp problems when voltage clamping branched neurons with intracellular microelectrodes In: T. G. Smith Jr, Lecar H, Redman SJ, Gage P, editors. Voltage and Patch Clamping with Microelectrodes. Bethesda, MD: American Physiological Society. pp. 191–215.

Randle JCR, Guet T, Cordi A, Lepagnol JM. 1992. Competitive inhibition by NBQX of kainate/AMPA receptor currents and excitatory synaptic potentials: importance of 6-nitro substitution. *Eur J Pharmacol* **215**:237–244. doi:https://doi.org/10.1016/0014-2999(92)90033-Z

Redman S. 1990. Quantal analysis of synaptic potentials in neurons of the central nervous system. *Physiol Rev* **70**:165–198. doi:10.1152/physrev.1990.70.1.165

Reid CA, Clements JD. 1999. Postsynaptic expression of long-term potentiation in the rat dentate gyrus demonstrated by variance-mean analysis. *J Physiol* **518**:121–130. doi:https://doi.org/10.1111/j.1469-7793.1999.0121r.x

Sahara Y, Takahashi T. 2001. Quantal components of the excitatory postsynaptic currents at a rat central auditory synapse. *J Physiol* **536**:189–197. doi:https://doi.org/10.1111/j.1469-7793.2001.00189.x

Silver RA. 2003. Estimation of nonuniform quantal parameters with multiple-probability fluctuation analysis: theory, application and limitations. *J Neurosci Methods* **130**:127–141. doi:https://doi.org/10.1016/j.jneumeth.2003.09.030

Spruston N, Jaffe DB, Williams SH, Johnston D. 1993. Voltage- and space-clamp errors associated with the measurement of electrotonically remote synaptic events. *J Neurophysiol* **70**:781–802. doi:10.1152/jn.1993.70.2.781

Stern P, Edwards FA, Sakmann B. 1992. Fast and slow components of unitary EPSCs on stellate cells elicited by focal stimulation in slices of rat visual cortex. *J Physiol* **449**:247–278. doi:https://doi.org/10.1113/jphysiol.1992.sp019085

Stuart G, Spruston N. 1998. Determinants of Voltage Attenuation in Neocortical Pyramidal Neuron Dendrites. *The Journal of Neuroscience* **18**:3501–3510. doi:10.1523/JNEUROSCI.18-10-03501.1998

Vere-Jones D. 1966. SIMPLE STOCHASTIC MODELS FOR THE RELEASE OF QUANTA OF TRANSMITTER FROM A NERVE TERMINAL. *Australian Journal of Statistics* **8**:53–63. doi:https://doi.org/10.1111/j.1467-842X.1966.tb00164.x

Wall MJ, Usowicz MM. 1998. Development of the quantal properties of evoked and spontaneous synaptic currents at a brain synapse. *Nat Neurosci* **1**:675–682. doi:10.1038/3677

Wang N-S, Marino M, Malinow R. 2024. Detecting unitary synaptic events with machine learning. *Proceedings of the National Academy of Sciences* **121**:e2315804121. doi:10.1073/pnas.2315804121

Williams SR, Mitchell SJ. 2008. Direct measurement of somatic voltage clamp errors in central neurons. *Nat Neurosci* **11**:790–798. doi:10.1038/nn.2137

Williams SR, Stuart GJ. 2002. Dependence of EPSP Efficacy on Synapse Location in Neocortical Pyramidal Neurons. *Science (1979)* **295**:1907–1910. doi:10.1126/science.1067903

Yuste R. 2010. Dendritic Spines. The MIT Press. doi:10.7551/mitpress/9780262013505.001.0001

Yuste R, Majewska A, Cash SS, Denk W. 1999. Mechanisms of Calcium Influx into Hippocampal Spines: Heterogeneity among Spines, Coincidence Detection by NMDA Receptors, and Optical Quantal Analysis. *The Journal of Neuroscience* **19**:1976–1987. doi:10.1523/JNEUROSCI.19-06-01976.1999

Figures

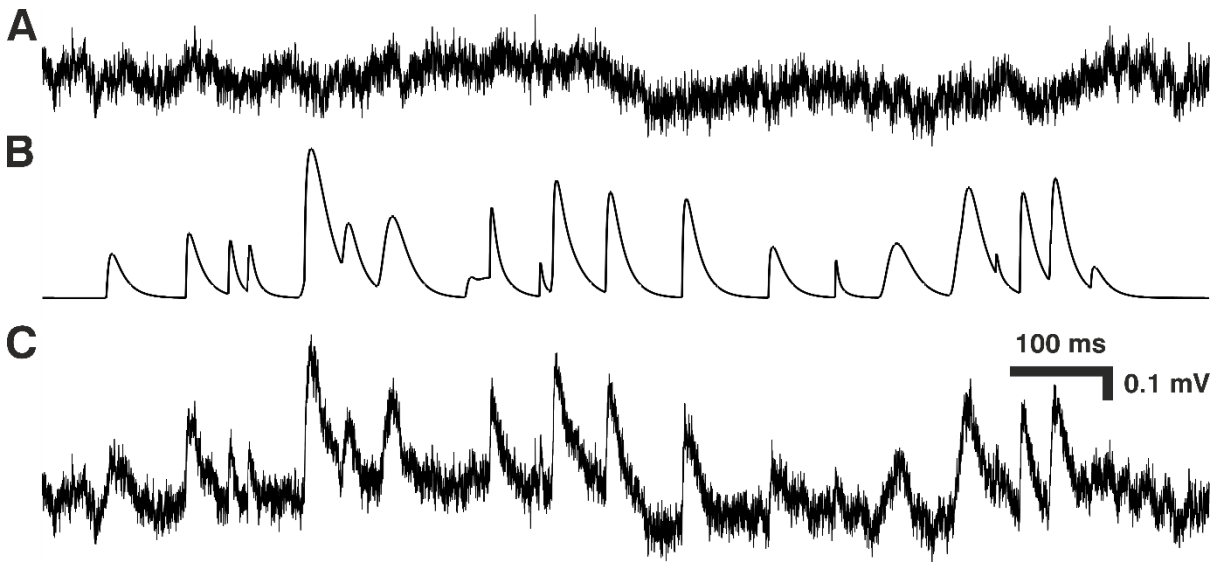

Figure 1: Constructing 'noise with simulated minis' voltage trace.

(A) Segment of 'noise-alone' voltage recording (from cortical layer 2/3 pyramidal neuron p131a).

(B) Simulated mEPSPs that were randomly added to the noise-alone trace in (A) to produce the 'real noise with simulated mEPSPs' voltage trace in (C).

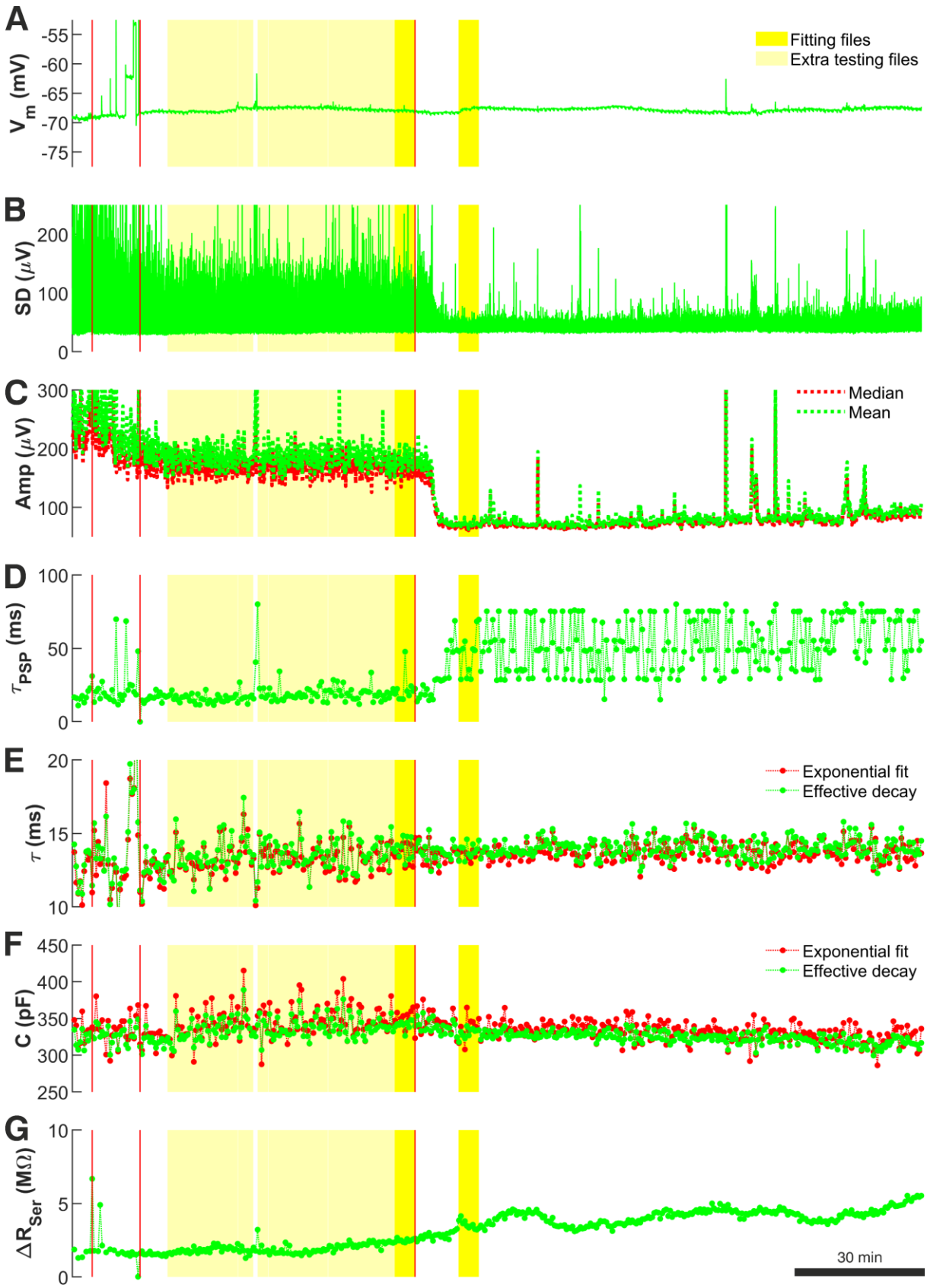

Figure 2: Recording quality measures used during the data preprocessing stage to select 'noise with

902 minis' and 'noise-alone' recording sweeps for further data analysis for recording p103a (layer 5
903 'burster' with tuft and thick trunk).
904 (A) Baseline V_m across the entire recording session. Stimulation pulses were excluded from the
905 display. The total recording duration (excluding pulse periods) was 8520 s. The first red vertical line
906 marks the time when pharmacological blockade of APs was initiated. The second red vertical line
907 marks the time when no more APs were observed in the recording. The third red vertical line marks
908 the time when pharmacological blockade of mEPSPs was initiated. Bright yellow periods mark 'noise
909 with minis' and 'noise-alone' recording segments selected as the main comparison files for the
910 distribution fitting. Light yellow marks all the remaining good quality 'noise with minis' recording
911 sweeps that were also included in the distribution fitting procedure for estimating target SAD, MAD,
912 and 'deviation' scores, as well as statistical evaluation of fits (see Methods).
913 (B) V_m standard deviation measured over consecutive 15 ms windows over the same recording
914 session.
915 (C) Evolution of mean and median amplitudes of the biggest top 10% of detected events (including
916 minis and noise events), averaged over single sweeps (duration of each was 4 s).
917 (D) Effective decay time constants (time to drop to 1/e of starting value 'safely' (8 ms) after the peak
918 and upwardly convex part) of the same biggest 10% of detected events as in panel (C) averaged over
919 consecutive 20-second-long (5-sweep-long) segments across the same session. Once minis were
920 blocked pharmacologically, effective time constant of detected events, (now pure noise) increased,
921 and its scatter, so this is another useful indication of when the block is complete.
922 (E) Evolution of passive membrane time constant over the entire recording session. Measurements
923 were averaged over consecutive 20-second-long (5-sweep-long) segments. Measurements based on
924 exponential decay curve fit and on 'effective time constant' (time for V_m to drop to 1/e of a value
925 just after change in current (after pipette capacitance artefact and fast charge redistribution
926 components: starting at 4 ms after the end of the pulse).

927 (F) Evolution of total cell membrane capacitance across the recording session. Measurements were
928 averaged over consecutive 20-second-long (5-sweep-long) segments. Measurements based on
929 exponential decay curve fit and on effective time constant (time taken for V_m drop to 1/e of an initial
930 value of the slowest impulse response component).
931 (G) Evolution of whole-cell pipette series resistance change (bridge balance error) across the
932 recording session, calculated from any jumps at starts or ends of charging curves. Measurements
933 were averaged over consecutive 4-second-long (5-sweep-long) segments.
934

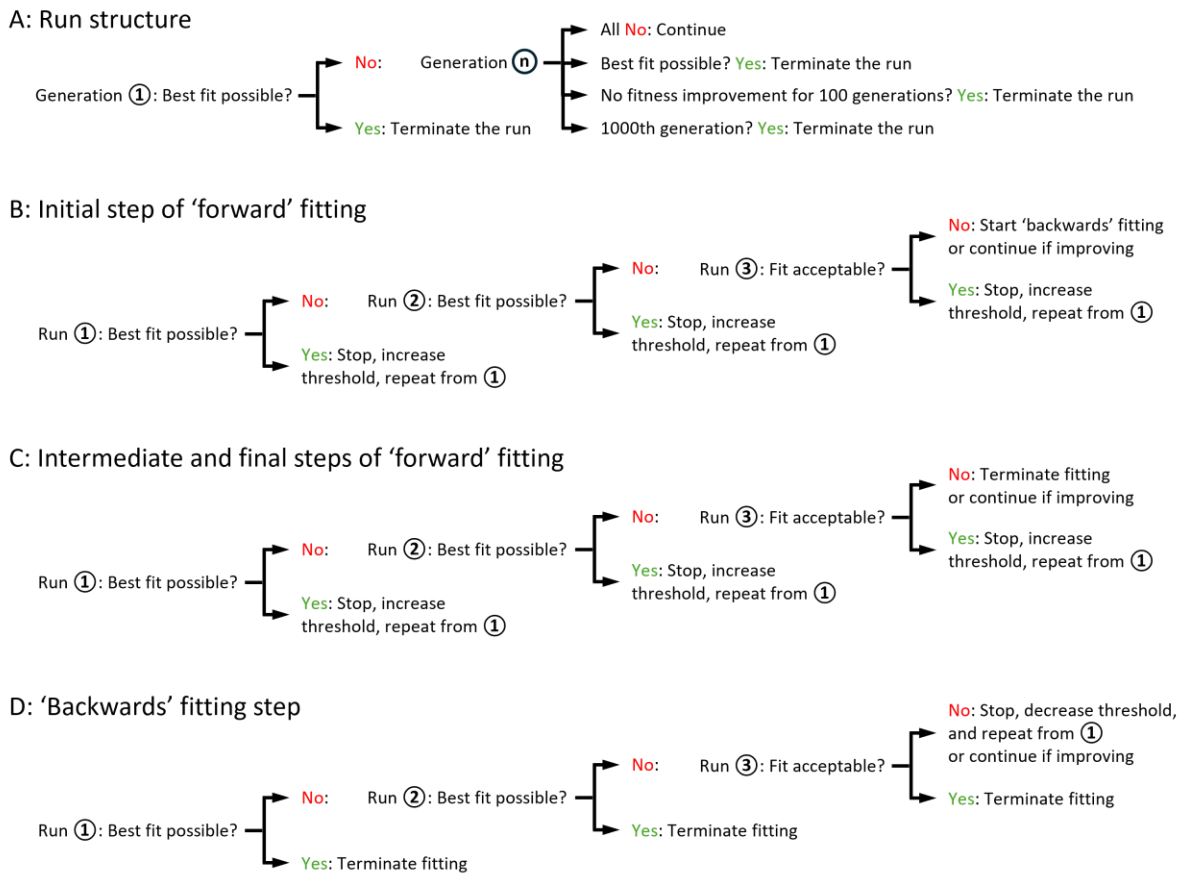

Figure 3: Schematic illustration of 'minis' genetic algorithm execution steps leading to the discovery of a minis source distribution underlying a distribution of minis-like events detected in a 'noise with minis' recording.

(A) The structure of a single GA run.

(B) The structure of the initial step of the 'forward' ('upward') fitting procedure where the lower threshold of the simulated minis amplitude is gradually raised.

(C) The structure of intermediate and final steps of the 'forward' ('upward') fitting procedure.

(D) The structure of the 'backwards' ('downwards') fitting procedure where the lower threshold of the simulated minis amplitude is gradually lowered.

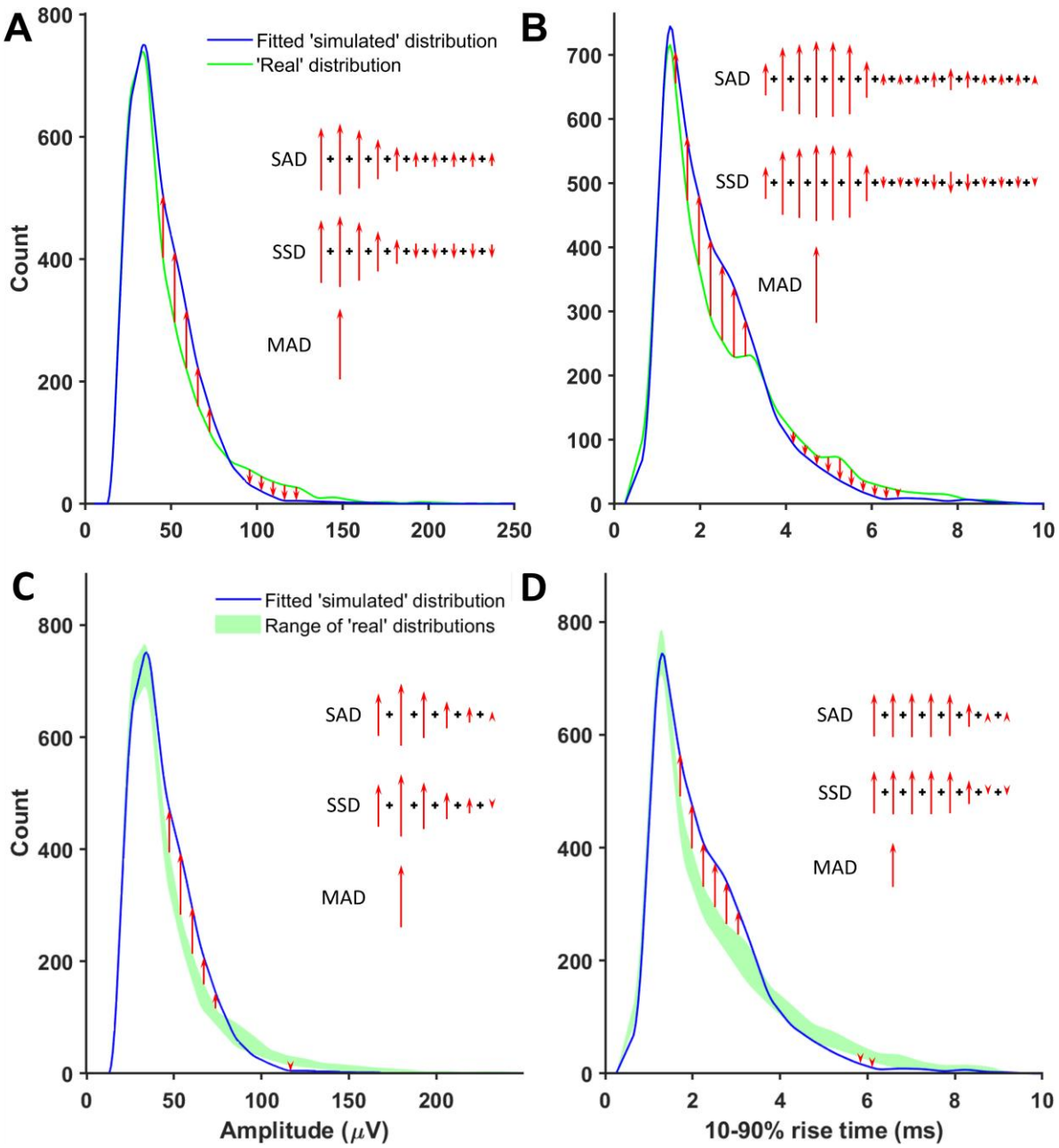

Figure 4: Non-shape components of the genetic algorithm's cost function.

(A) A schematic illustration of how amplitude SADs, MADs, and SSDs were calculated. Red arrows mark detected minis-like event count discrepancies between 'simulated' and 'real' 'noise with minis' distribution bins.

(B) A schematic illustration of how 10-90% rise time SADs, MADs, and SSDs were calculated.

(C) A schematic illustration of how amplitude 'envelope deviation' scores corresponding to SADs, MADs, and SSDs were calculated. Red arrows mark detected minis-like event count discrepancies

954 between the ‘noise with simulated minis’ distribution and the envelope of all superimposed ‘noise

955 with real minis’ distribution bins.

956 (D) A schematic illustration of how 10-90% rise time ‘envelope deviation’ scores corresponding to

957 SADs, MADs, and SSDs were calculated.

958

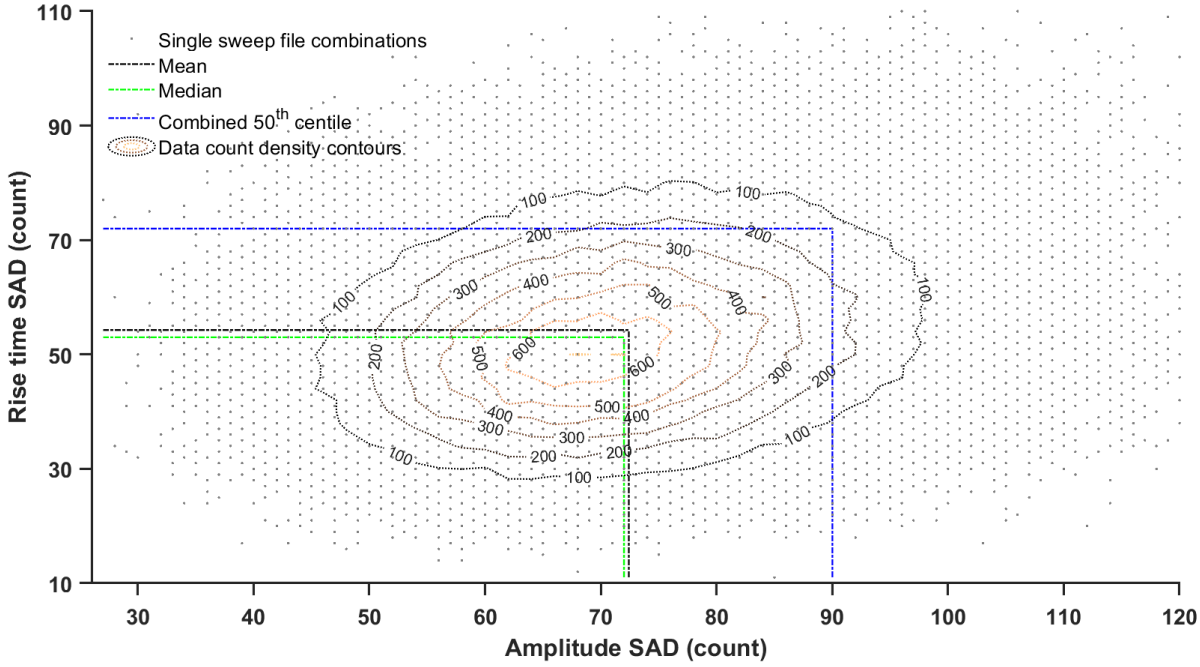

Figure 5: Amplitude and rise time scattergram (density plot) of sum of absolute deviation (SAD) scores between histograms from all possible pairs of 'noise with minis' single sweep files (4 s) from a layer 5 pyramidal neuron (p103a).

The line marking 'combined 50th centile' cutoff is based on 15 different SAD, SSD, and MAD scores as explained in Tables 1 and 2 (it extends to the remaining 13 dimensions not shown here). '15-score combined 50th centile' sets a lower (more exacting) threshold for accepting ('steering') distribution fits than the mean or the median would. This is justified because distribution fits need to satisfy all 15 SAD, SSD, and MAD scores *simultaneously* (e.g. to ensure that one of the tails of the distribution is not badly fit, as well as the remaining parts of the distribution).

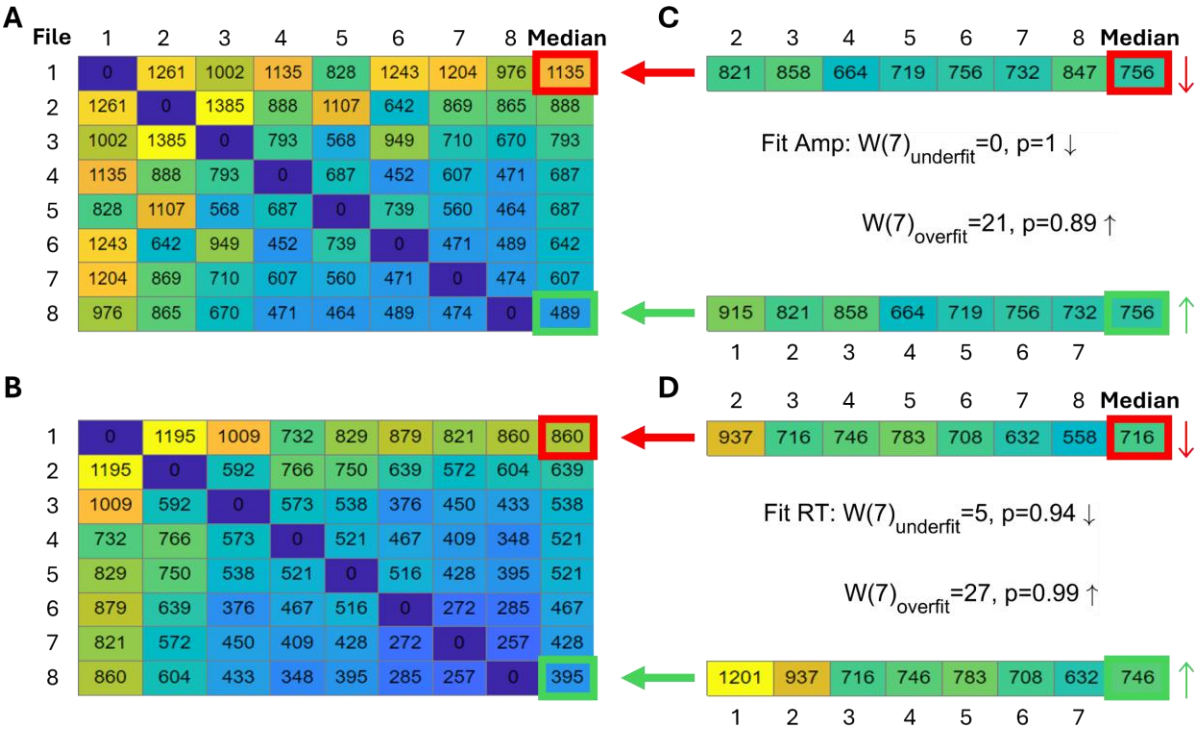

Figure 6: A schematic illustration of simulated minis distribution acceptance tests.

(A) A matrix showing amplitude SADs for all 'noise with real minis' recording file comparisons. The last matrix column shows the median SAD score for all comparisons in individual matrix rows. The matrix cell with thick red borders indicates the 'worst'-performing distribution, while the cell with thick green borders indicates the 'best'-performing distribution.

(B) A matrix showing 10-90% rise time SADs for all 'noise with real minis' recording file comparisons.

(C) Two sets of SADs for comparisons of the 'noise with simulated minis' amplitude distribution and all non-reference 'noise with real minis' amplitude distributions. The top vector contains comparisons with the same 'real' distributions/files as the top matrix row in (A) as indicated by the thick red arrow (the reference 'worst' distribution was excluded from the comparison). The thin red arrow points in the downward direction consistent with the 'simulated' median (right) being lower than the 'real' 'worst'-performing distribution's median (left). The bottom vector contains comparisons with the same 'real' distributions/files as the bottom matrix row in (A) as indicated by the thick green arrow (the reference 'best' distribution was excluded from the comparison). The thin green arrow points in the upward direction consistent with the 'simulated' median (right) being

986 higher than the ‘real’ ‘best’-performing distribution’s median (left). Results of the amplitude
987 acceptance Wilcoxon signed-rank paired samples test for the simulated minis distribution are shown
988 in the middle between the two SAD vectors. The top line tests whether the median of the SAD vector
989 top set in (C) is larger than the median in the red-bordered cell of the matrix in (A) ($W_{underfit}$; the
990 number of files/distributions minus the reference distribution is indicated within brackets). The
991 downward arrow indicates that the median of the SAD vector in (C) is smaller than the red-bordered
992 median in (A). The bottom line tests whether the median of the SAD vector bottom set is smaller
993 than the median in the green-bordered cell of the matrix in (A) ($W_{overfit}$). The upward arrow indicates
994 that the median of the SAD vector in (C) is larger than the green-bordered median in (A).
995 (D) A set of SADs and acceptance tests as in (C) but for the 10-90% rise time distribution of simulated
996 minis.
997

998 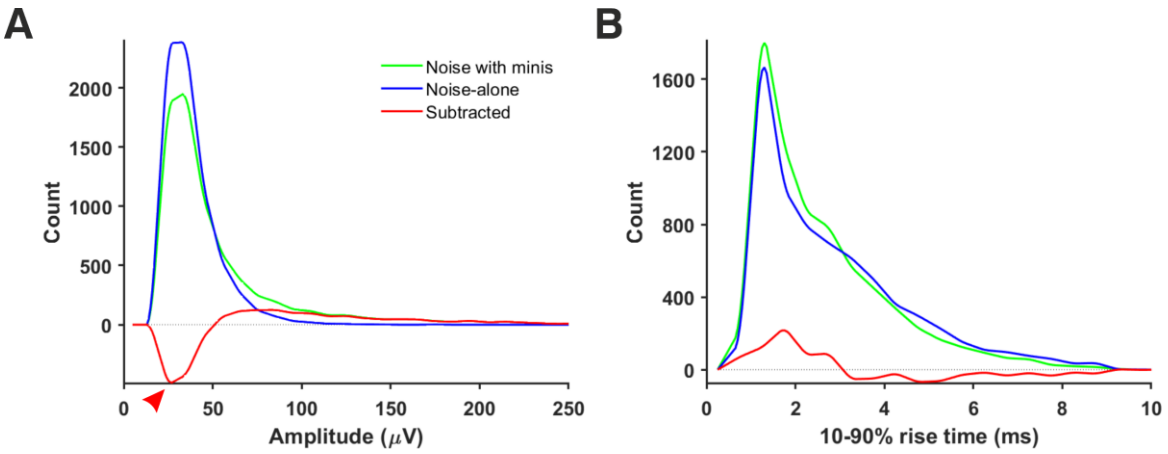

999 **Figure 7:** Amplitude and rise time distributions of detected mini-like events in 'noise with minis' and

1000 'noise-alone' recordings.

1001 (A) Amplitude distributions in a "thick" tufted neocortical layer 5 pyramidal neuron (p108b). Red

1002 arrowhead indicates negative bins after subtracting 'noise-alone' distribution from 'noise with minis'

1003 distribution.

1004 (B) 10-90% rise time distributions from the same neuron.

1005

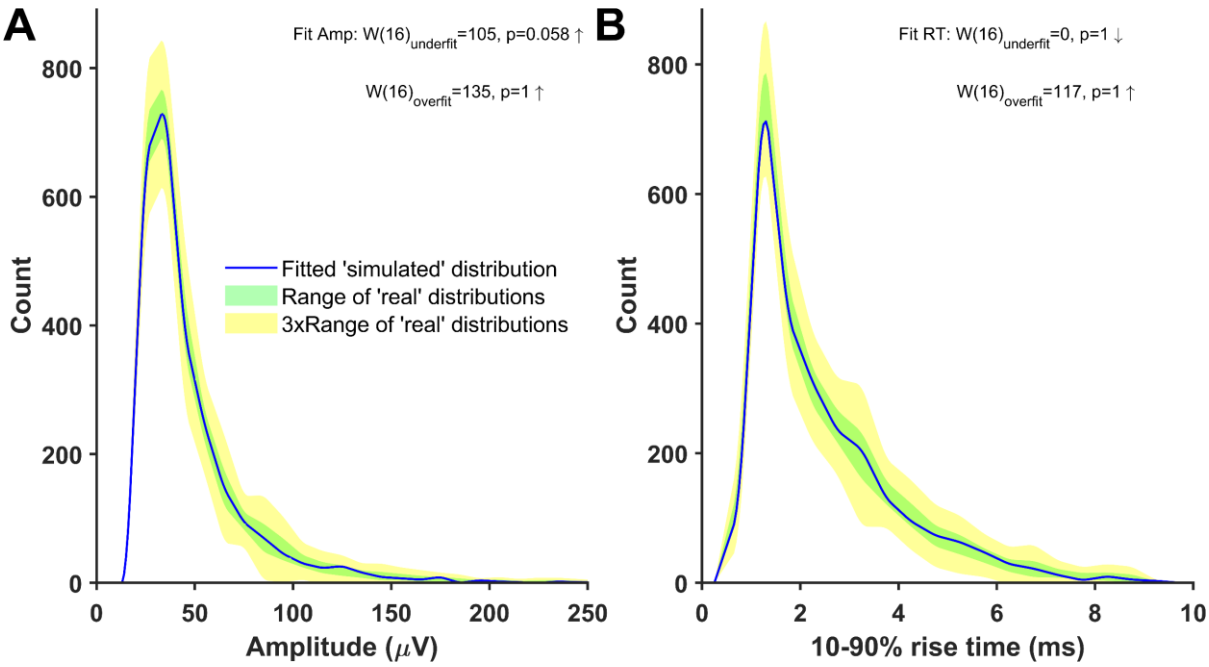

Figure 8: Distributions of mini-like events detected in a 'noise with simulated minis' voltage trace reasonably closely matching 'noise with real minis' recordings from the same cell, p106b (neocortical layer 5).

Parameters of simulated minis were controlled by the Genetic Algorithm. Up arrows indicate 'simulated' SAD > 'real' SAD; down arrows 'simulated' SAD < 'real'. The underfit test involves a comparison with the 'worst-performing' 'real' SAD (most discrepant from the others), whereas the overfit ('excellent fit') test involves a comparison with the 'best-performing' 'real' SAD (least discrepant from the others). With the underfit test (top), a fit SAD worse (bigger) than the 'real' SAD (up arrow), and $p < 0.05$ would mean the fit is rejected (not the case here: both amplitude and rise time fits (A and B) were accepted). (See Methods and Figure 6 for more details).

(A) Amplitude and (B) 10-90% rise time distributions (blue) of mini-like events detected in a 'noise with simulated minis' voltage trace, compared with 'envelopes' or bands (shaded) of all available 'real' data distributions from the neuron (taking the most extreme low and high values at each point across all the available data files recorded with both APs and IPSPs blocked).

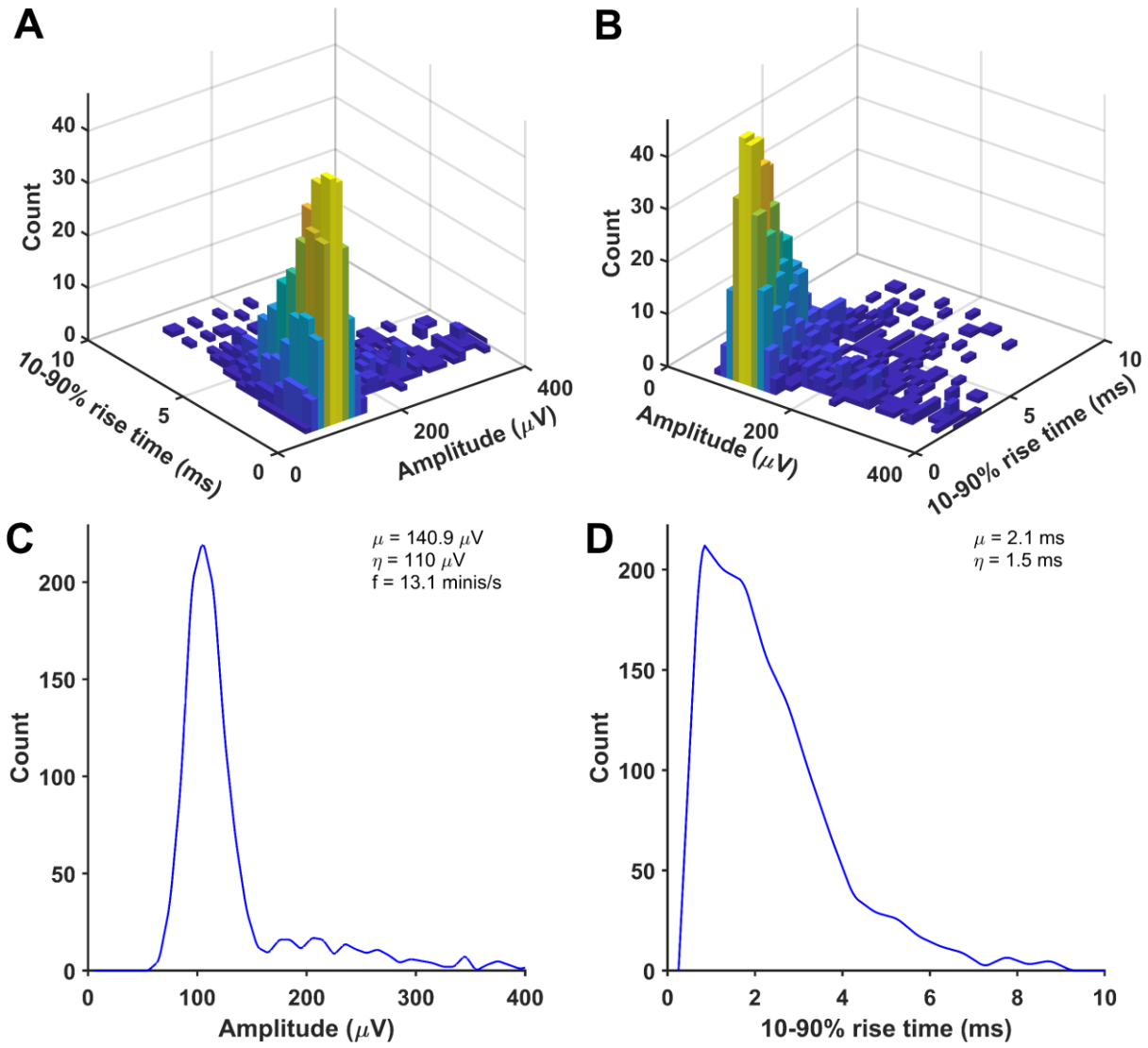

Figure 9: An example of a simulated minis distribution that was used to produce a close match between the distributions of detected mini-like events in a 'noise with simulated minis' voltage trace (with a 60 µV lower limit on simulated amplitudes) and a 'noise with real minis' recording, for a neocortical layer 2/3 cell (p131c).

(A) and (B) Joint amplitude and 10-90% rise time distribution of simulated minis, viewed from different angles.

(C) and (D) Corresponding 'marginal' (one-dimensional) amplitude and 10-90% rise time distributions, projected onto the axis indicated.

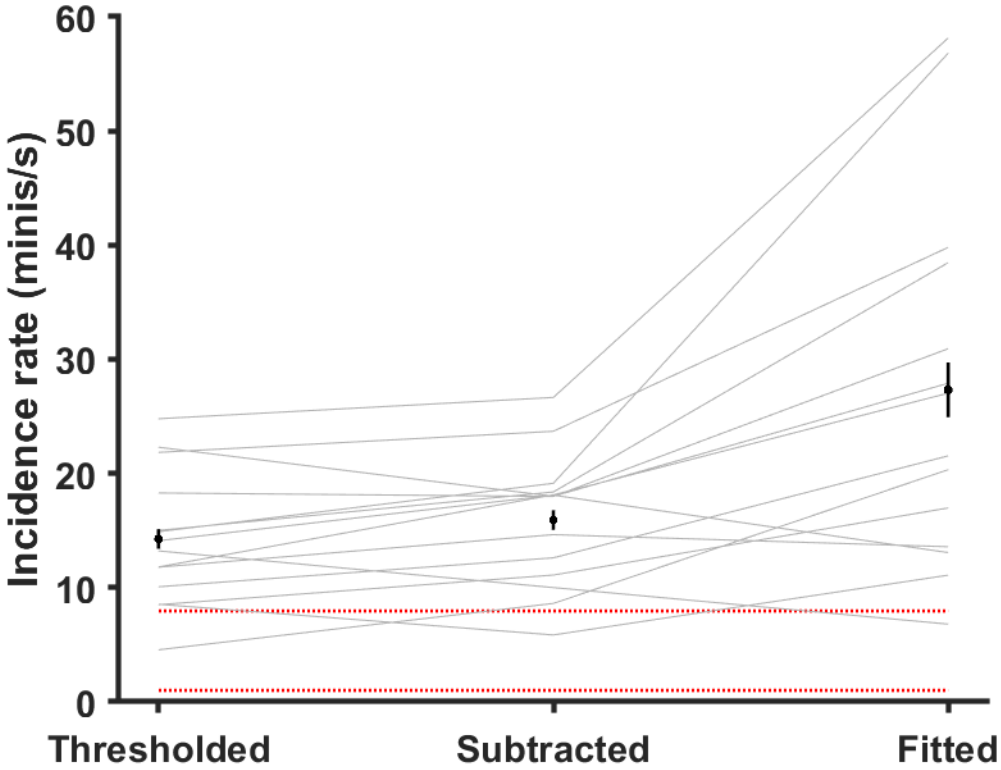

Figure 10: Estimated mEPSP incidence rates ('frequencies') using various methods (grey lines are individual cells).

'Thresholded' method: an 'unreasonably high' 80 µV detection threshold was applied to all 14 'noise with real minis' recordings so only larger events were included.

'Subtracted' method: the distribution of mini-like events in the 'noise-alone' recording was subtracted from the distribution of mini-like events in the 'noise with real minis' recording and the incidence rate estimate was based on the positive bins of the resulting distribution.

'Fitted' method: the simulated minis distribution was used to estimate a lower bound on the mEPSP incidence rate (*lowest* acceptable rate statistically consistent with the real experimental data).

Black markers and black vertical lines correspond to means and 95% confidence intervals. Red dotted lines mark the range of incidence rates typically reported in the literature; discussed in the companion article (Dervinis and Major, 2024).

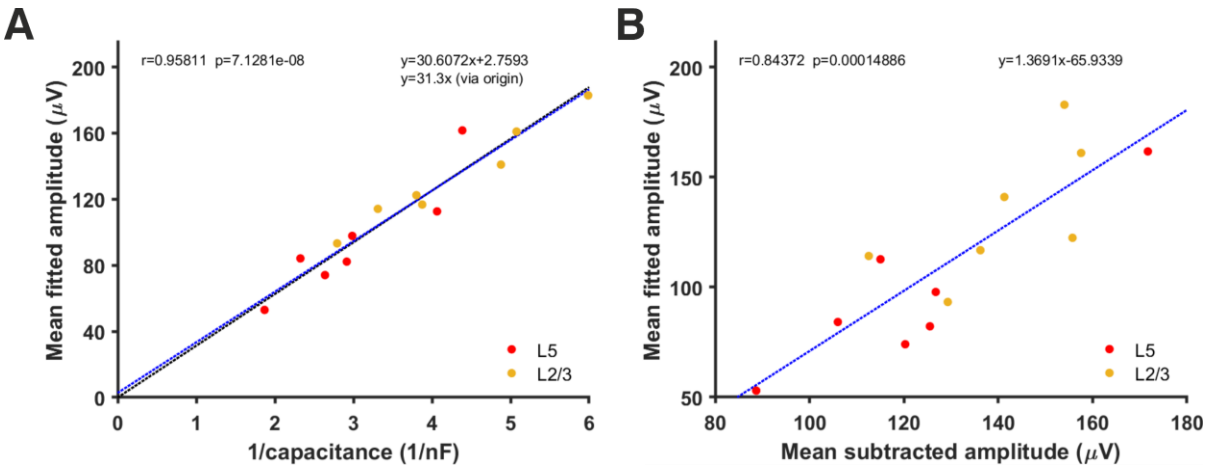

Figure 11: Relationship between each cell's inverse total membrane capacitance and its estimated mean mEPSP amplitude using simulations and fitting of minis distributions.

(A) Correlation between mean mini amplitudes from different neurons, as derived using the simulated minis distribution fitting method and the inverse of each cell's total capacitance. The blue line is the least square fit to the data while the (nearly indistinguishable) black line is the fit to the data that passes through the origin.

(B) Correlation between the mean mEPSP amplitude of each neuron estimated from 'fitting' versus 'subtracting' (the corresponding noise histogram, as in Figure 7).

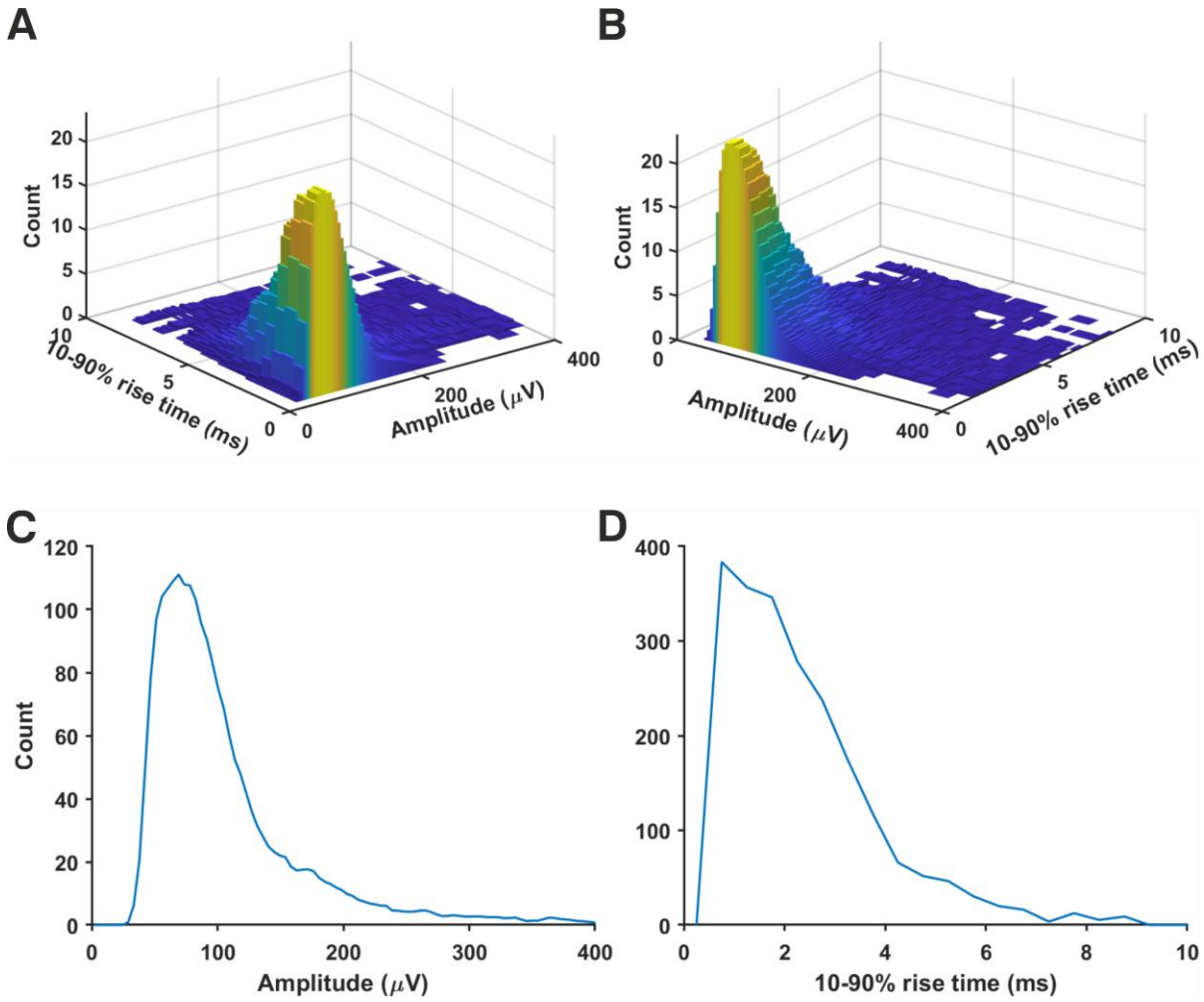

Figure 12: Generic 'averaged' mEPSP distribution from rat (somatosensory) neocortical pyramidal neurons.

Distributions resulting from all 14 recordings were averaged. All mini amplitudes were first normalised by the means of their respective source distributions, then multiplied by the average of the average amplitudes (114.1 ± 5.5 μV) across all the neurons analysed.

(A) A joint amplitude and 10-90% rise time distribution of simulated minis.

(B) The same distribution but viewed from a different angle.

(C) 'Marginal' (1-dimensional) amplitude distribution projected from the above distribution onto the amplitude axis.

(D) 'Marginal' 10-90% rise time distribution.

Tables

Amp SAD ≤56th centile?	Top 50% amp SAD ≤56th centile?	Top 10% amp SAD ≤56th centile?	Top 2% amp SAD ≤56th centile?	Top 50% amp SSD ≤0?	Top 10% amp SSD ≤0?	Top 2% amp SSD ≤0?	RT SAD ≤56th centile?	Joint SAD ≤56th centile?	Amp MAD ≤56th centile?	Top 50% amp MAD ≤56th centile?	Top 10% amp MAD ≤56th centile?	Top 2% amp MAD ≤56th centile?	RT MAD ≤56th centile?	Joint MAD ≤56th centile?
…	…	…	…	…	…	…	…	…	…	…	…	…	…	…
Yes	Yes	Yes	Yes	No	No	No	Yes	Yes	Yes	Yes	Yes	Yes	Yes	Yes
Yes	Yes	Yes	Yes	Yes	Yes	Yes	Yes	Yes	Yes	Yes	Yes	Yes	Yes	Yes
Yes	Yes	Yes	Yes	No	No	No	Yes	Yes	Yes	Yes	Yes	Yes	Yes	Yes
No	No	No	No	Yes	No	No	Yes	Yes	Yes	No	No	No	Yes	Yes
No	Yes	No	No	No	Yes	Yes	Yes	Yes	Yes	Yes	No	No	Yes	No
Yes	Yes	Yes	Yes	No	No	No	No	Yes	Yes	Yes	Yes	Yes	No	Yes
…	…	…	…	…	…	…	…	…	…	…	…	…	…	…

Table 1: Failed hypothetical attempt to use 56th centile as a basis for the combined '15-score 50th centile'.

The table shows a representative portion of a much bigger table illustrating a hypothetical scenario where the 15 SAD, SSD, and MAD scores are arranged in columns and rows corresponding to different two-file comparisons (many other comparisons are above and below those portrayed for the sake of the argument). SAD, SSD, and MAD scores are calculated by subtracting one file distribution from another (see the text for a detailed explanation). In this example, only *one* file comparison pair (green; 1/6 = 16.7%; row shaded in grey) satisfies the condition of having *all* its actual between-file SAD, SSD, and MAD values equal or below their respective 56th centile (across all comparison pairs - a unique value applying all the way down each column) – i.e. *simultaneously* in *all* columns. Therefore, the 56th percentile of each SAD, SSD, and MAD score would be too small to serve as the basis for the composite, joint or combined '15-score 50th centile': we need *half* the rows to be green, i.e. to pass the test.

Amp SAD ≤90th centile?	Top 50% amp SAD ≤90th centile?	Top 10% amp SAD ≤90th centile?	Top 2% amp SAD ≤90th centile?	Top 50% amp SSD ≤0?	Top 10% amp SSD ≤0?	Top 2% amp SSD ≤0?	RT SAD ≤90th centile?	Joint SAD ≤90th centile?	Amp MAD ≤90th centile?	Top 50% amp MAD ≤90th centile?	Top 10% amp MAD ≤90th centile?	Top 2% amp MAD ≤90th centile?	RT MAD ≤90th centile?	Joint MAD ≤90th centile?
…	…	…	…	…	…	…	…	…	…	…	…	…	…	…
Yes	Yes	Yes	Yes	Yes	Yes	Yes	Yes	Yes	Yes	Yes	No	No	No	Yes
Yes	Yes	Yes	Yes	Yes	Yes	Yes	Yes	Yes	Yes	Yes	Yes	Yes	Yes	Yes
Yes	Yes	Yes	Yes	Yes	Yes	Yes	Yes	Yes	Yes	Yes	Yes	Yes	Yes	Yes
Yes	Yes	Yes	Yes	Yes	Yes	Yes	Yes	Yes	Yes	Yes	Yes	Yes	Yes	No
Yes	Yes	Yes	Yes	Yes	Yes	Yes	Yes	Yes	Yes	Yes	Yes	Yes	No	No
Yes	Yes	Yes	Yes	Yes	Yes	Yes	Yes	Yes	Yes	Yes	Yes	Yes	Yes	Yes
…	…	…	…	…	…	…	…	…	…	…	…	…	…	…

Table 2: Using 90th SAD centile as a basis for the combined '15-score 50th centile'.

The table shows another example where the 15 SAD, SSD, and MAD scores are arranged in columns and rows correspond to different two-file comparisons. SAD, SSD, and MAD scores are calculated by subtracting one file distribution from another (see the text for a detailed explanation). Now *three* of the six file pairings (*half* of them: green; rows shaded in grey) satisfy the condition of having *all* their between-file SAD, SSD, and MAD scores equal or below their respective 90th centiles (across all comparison pairs - a unique number applying all the way down each column). Therefore, the 90th percentile works as the basis for the combined '15-score 50th centile'. Higher than 90 leads to more than half and lower than 90 leads to fewer than half of possible file pairs 'passing' all 15 tests simultaneously.

1083 **Supplementary Figures**

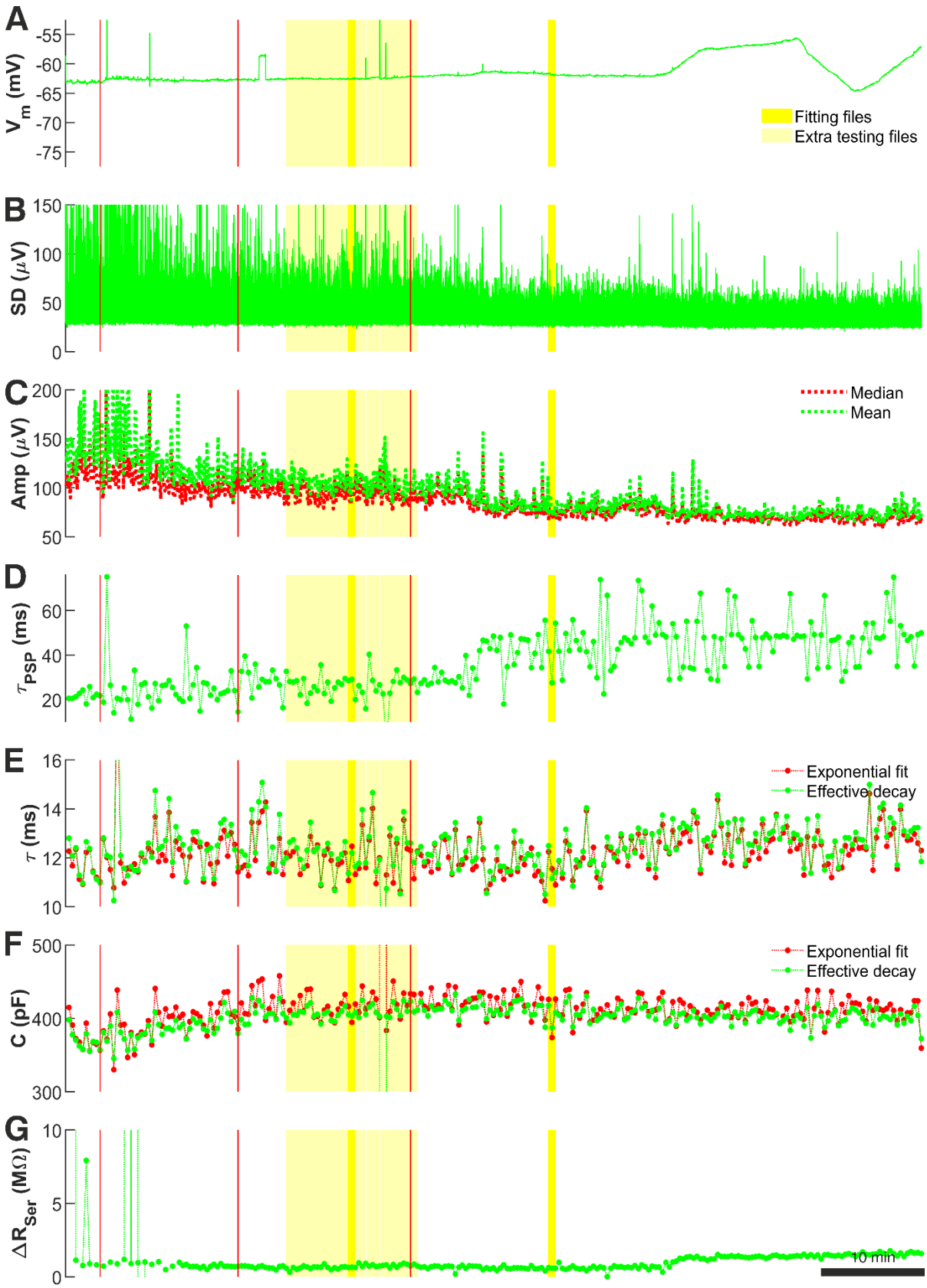

Supplementary Figure 1: Cell p106b (layer 5). Recording quality measures used to select 'noise with minis' and 'noise-alone' sweeps.

1087 (A) Baseline V_m across entire recording (excluding stimulation pulse periods); duration 4960 s. Red

1088 lines and shaded yellow regions and Panels B-G as for Figure 2.

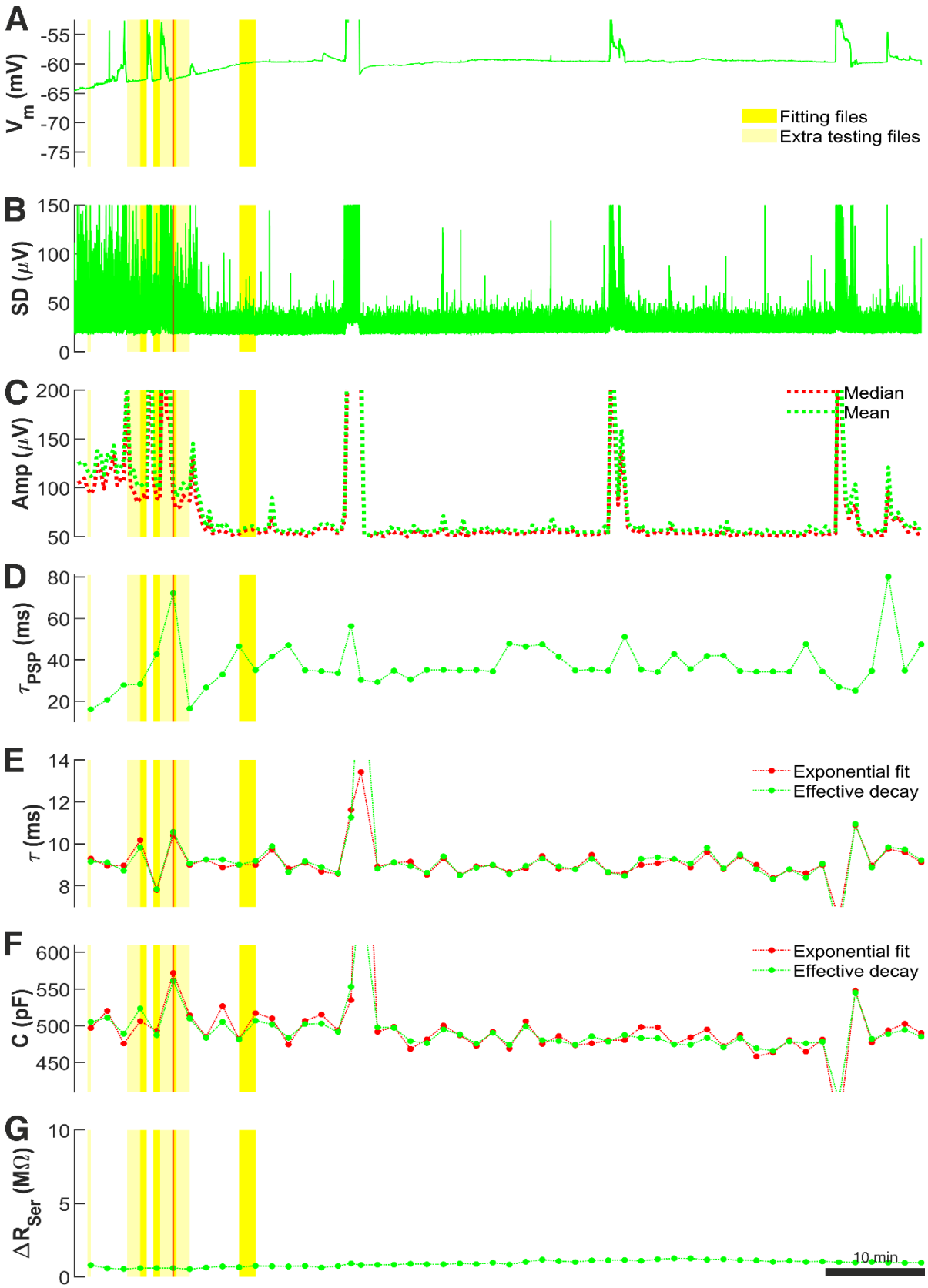

Supplementary Figure 2: Cell p108a (layer 5). Recording quality measures used to select 'noise with minis' and 'noise-alone' sweeps.

1092 Panels A-G as for Figure 1 except for data being averaged over 100-second-long windows (5
1093 recording sweeps of 20 s each) in panels D-G. The figure shows only part of the recording following
1094 the blockade of APs with only a single red vertical time marker visible indicating the time when
1095 pharmacological EPSP blockers were infused. The total duration of the recording shown in the figure
1096 was 5140 s. Some episodes with transient recording instabilities (noise glitches) were removed from
1097 the 'noise with minis' epoch (white gaps).
1098

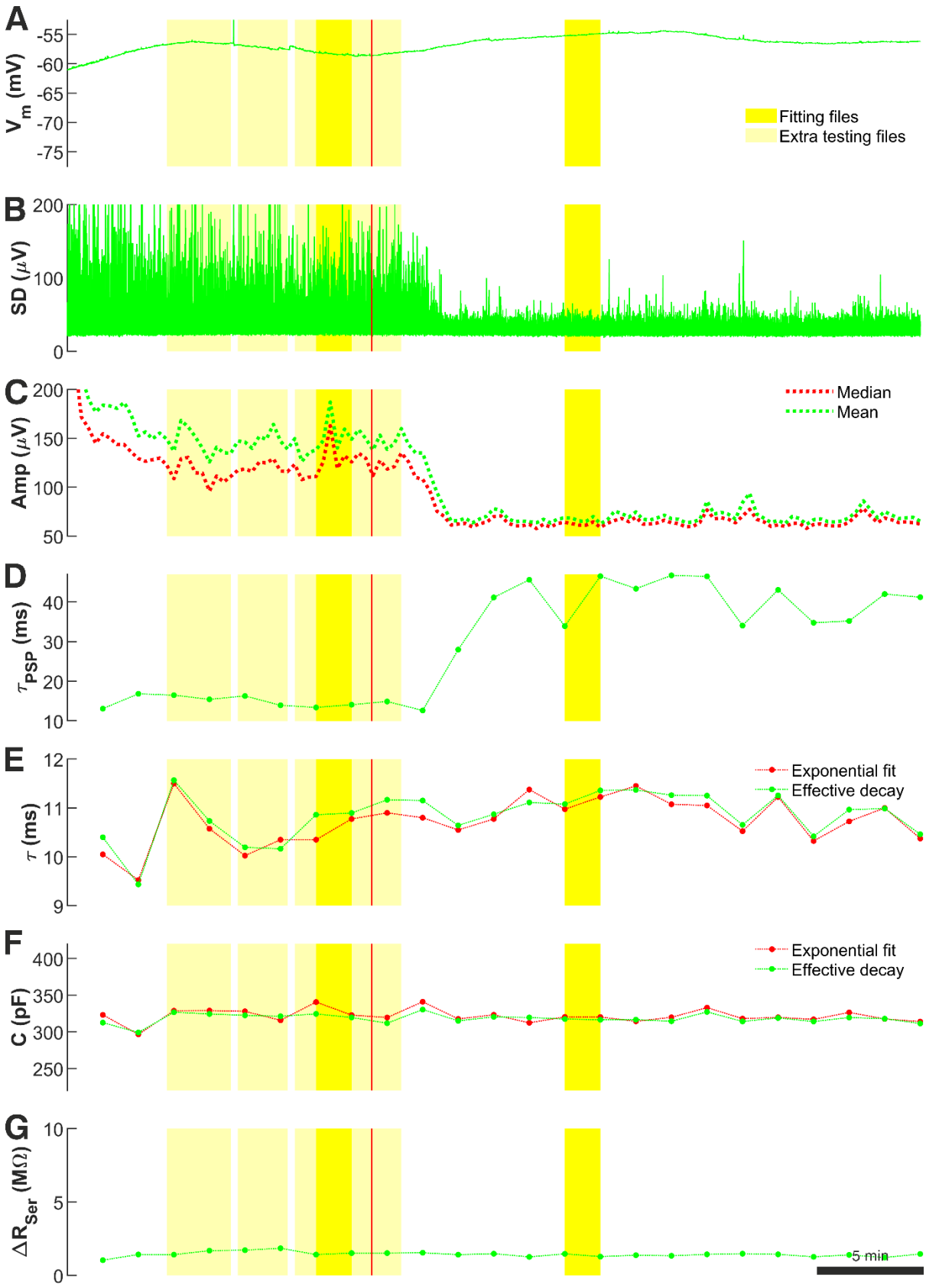

Supplementary Figure 3: Cell p108b (layer 5). Recording quality measures used to select 'noise with minis' and 'noise-alone' sweeps.

1102 Panels A-G as for Figure 2 and Supplementary Figure 2. Data were averaged over 100-second-long

1103 windows (5 recording sweeps of 20 s each) in panels D-G; duration 2400 s.

1104

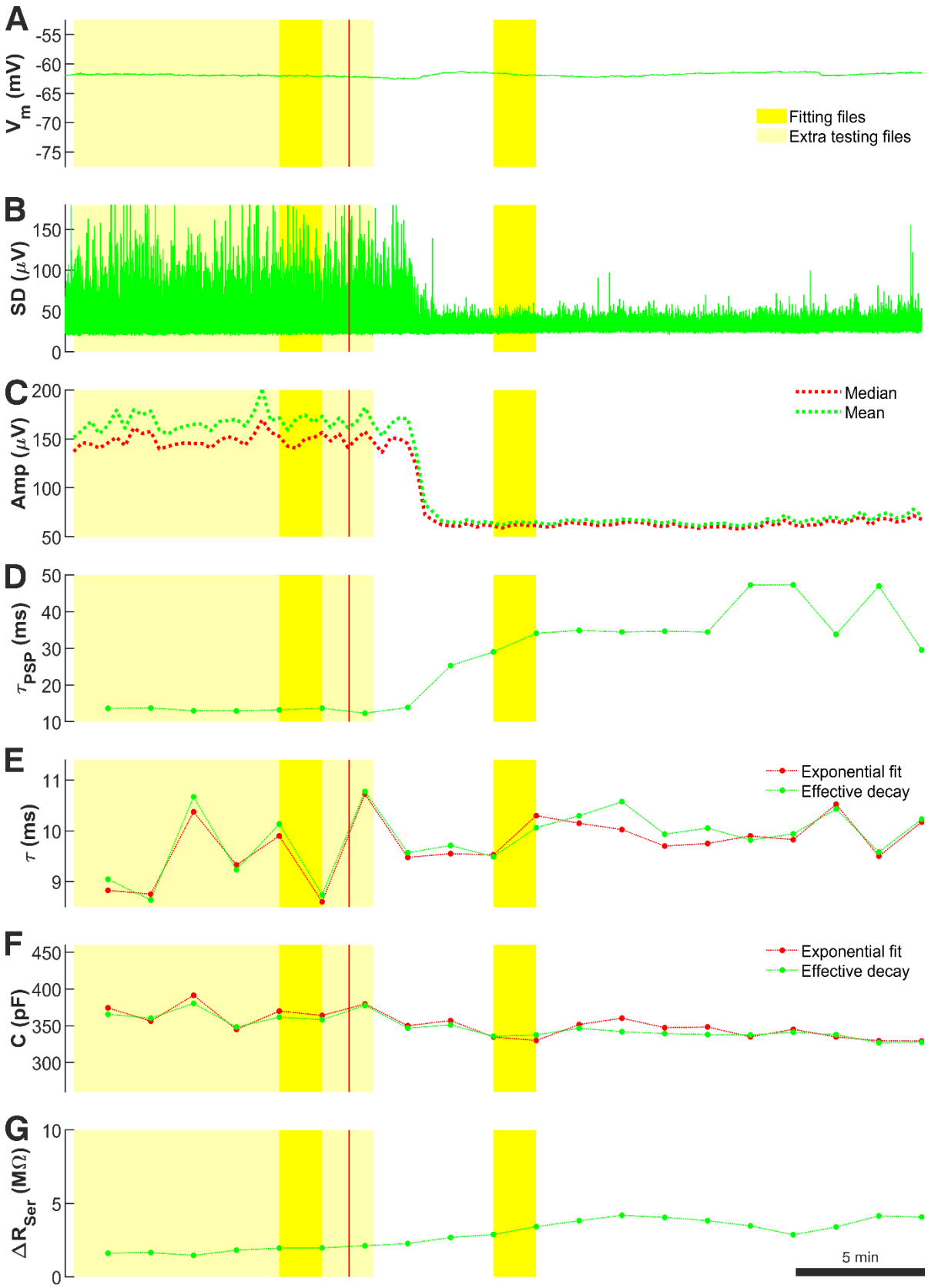

Supplementary Figure 4: Cell p108c (layer 5). Recording quality measures used to select 'noise with minis' and 'noise-alone' sweeps.

1108 Panels A-G as for Figure 2 and Supplementary Figure 2. Data were averaged over 100-second-long

1109 windows (5 recording sweeps of 20 s each) in panels D-G; duration 2000 s.

1110

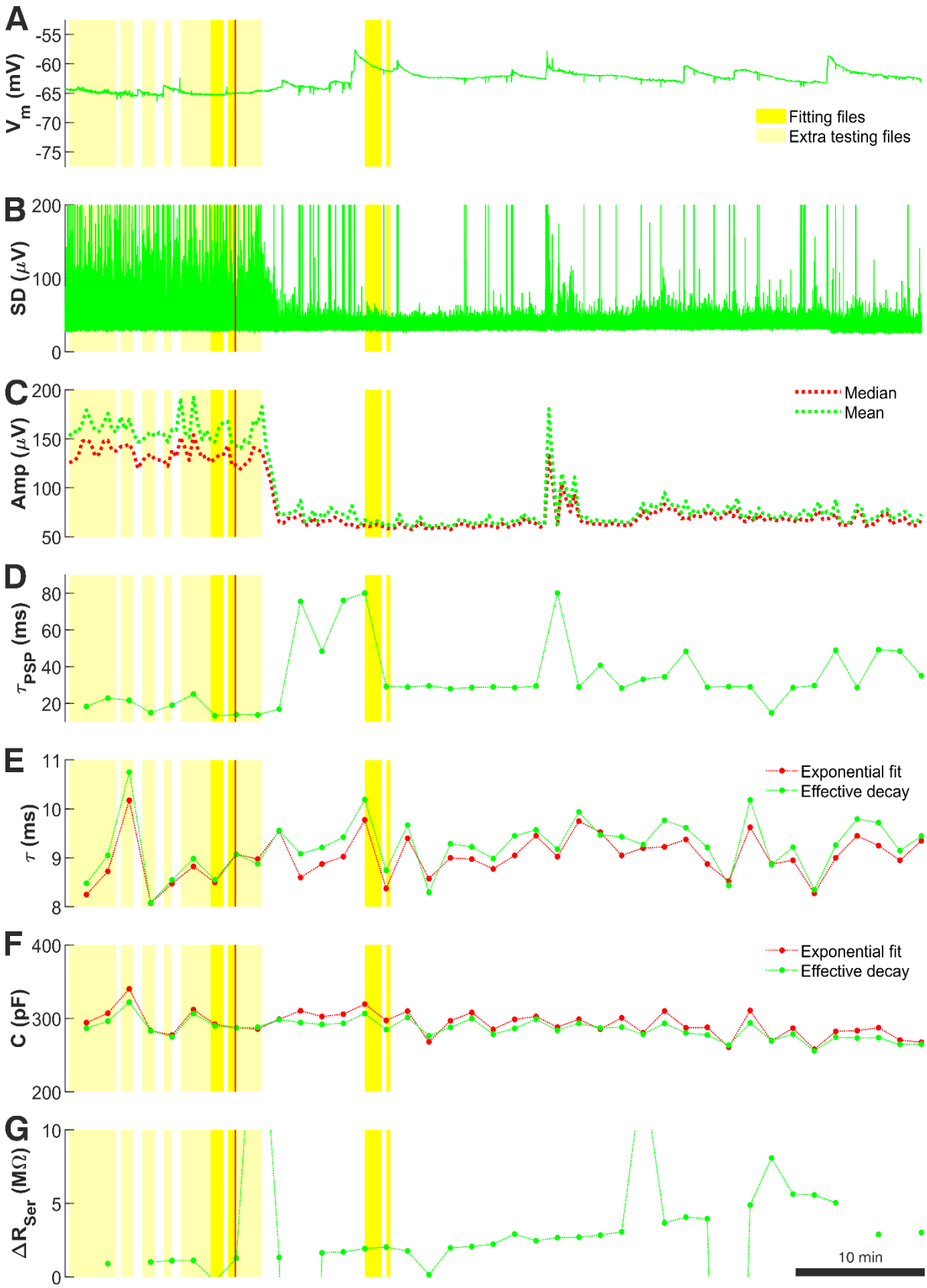

Supplementary Figure 5: Cell p120b (layer 2/3). Recording quality measures used to select 'noise with minis' and 'noise-alone' sweeps.

Panels A-G as for Figure 2 and Supplementary Figure 2. Data were averaged over 100-second-long windows (5 recording sweeps of 20 s each) in panels D-G; duration 4000 s. Some transient ‘glitchy’ extra noisy periods (due to transient recording instability) were manually excluded from the ‘noise with minis’ and ‘noise-alone’ epochs (white gaps).

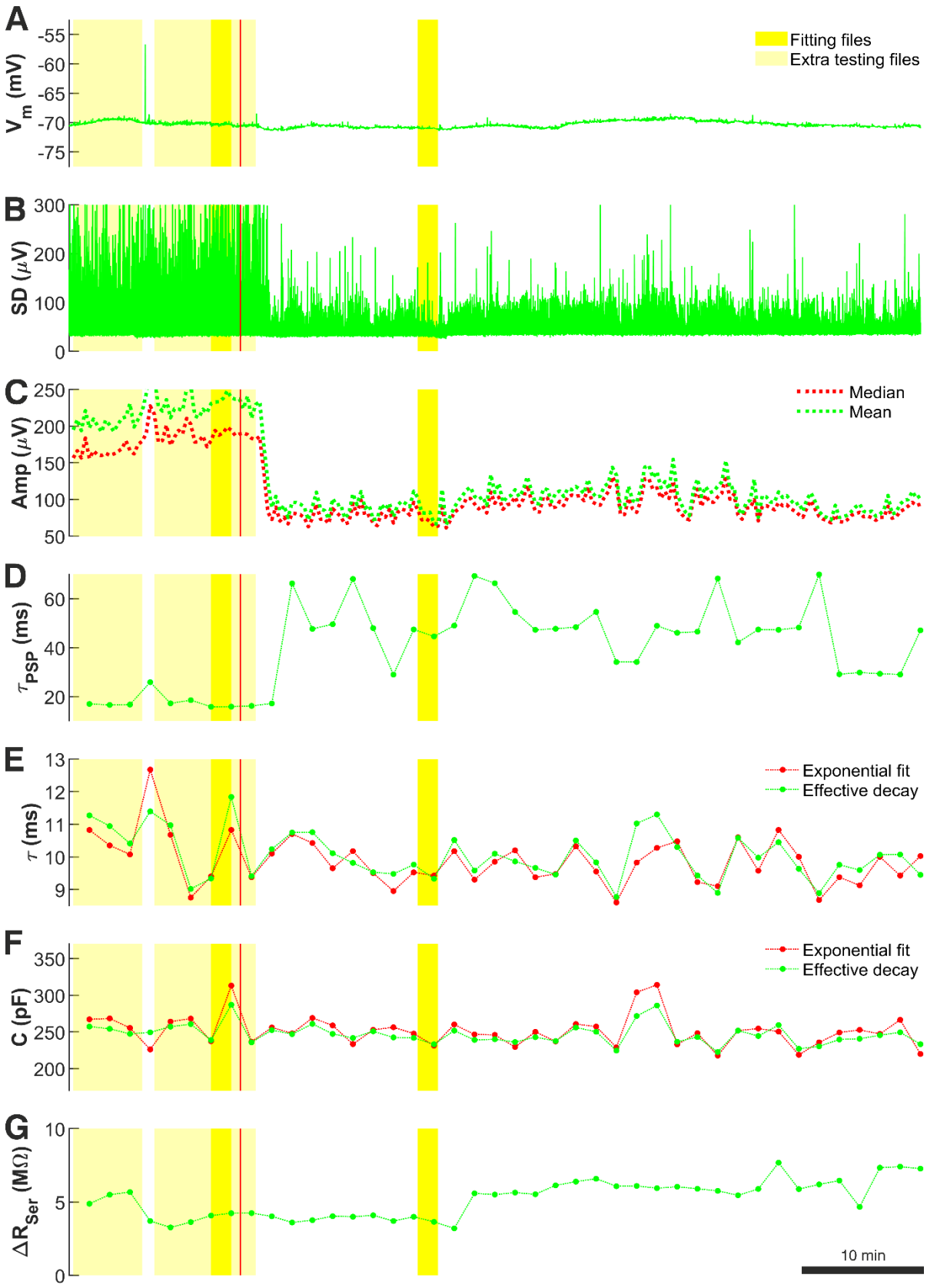

Supplementary Figure 6: Cell p122a (layer 2/3). Recording quality measures used to select 'noise with minis' and 'noise-alone' sweeps.

1122 Panels A-G as for Figure 2 and Supplementary Figure 2. Data were averaged over 100-second-long

1123 windows (5 recording sweeps of 20 s each) in panels D-G; duration 4200 s.

1124

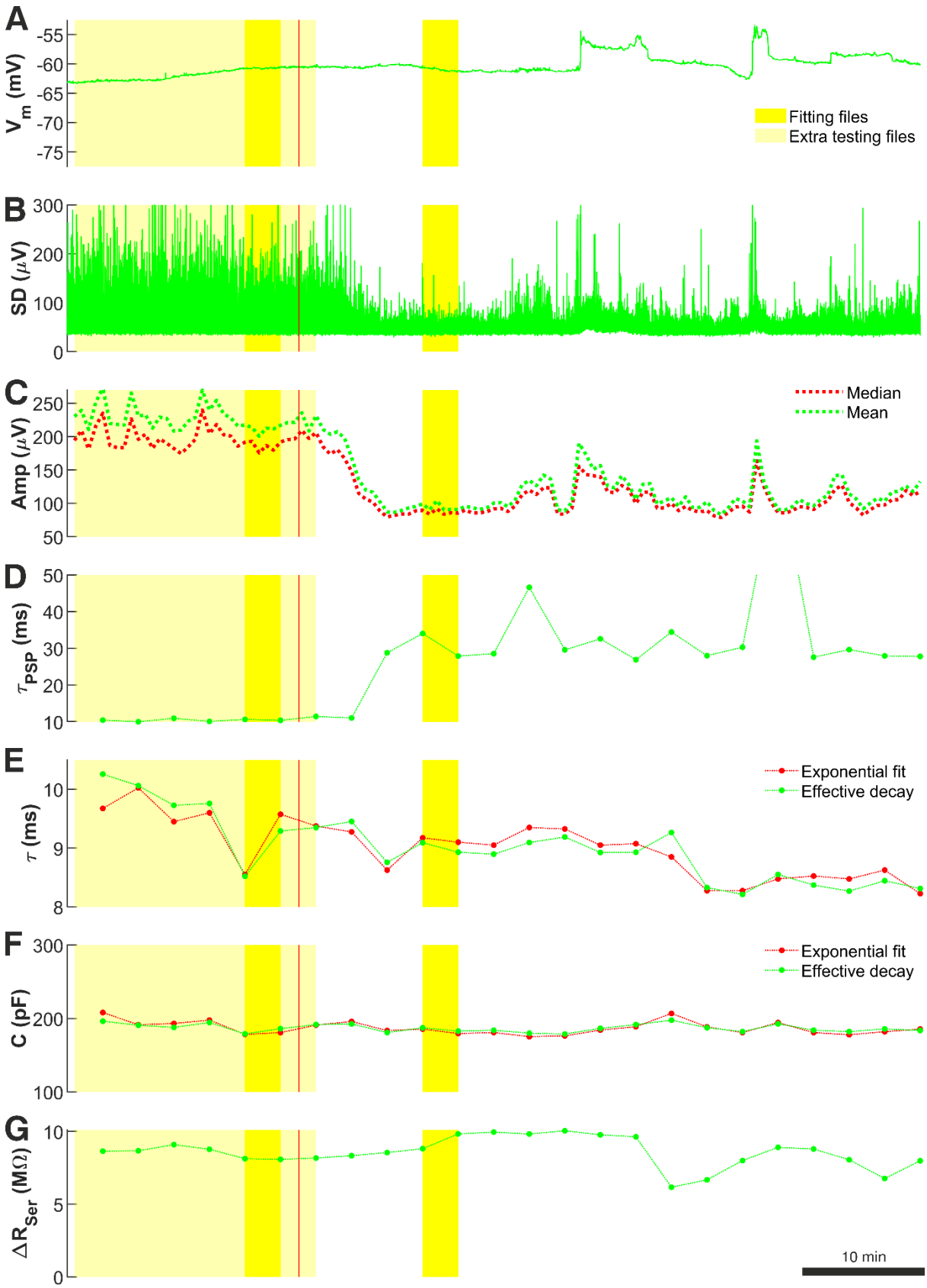

Supplementary Figure 7: Cell p124b (layer 5). Recording quality measures used to select 'noise with minis' and 'noise-alone' sweeps.

1128 Panels A-G as for Figure 2 and Supplementary Figure 2. Data were averaged over 100-second-long

1129 windows (5 recording sweeps of 20 s each) in panels D-G; duration 2400 s.

1130

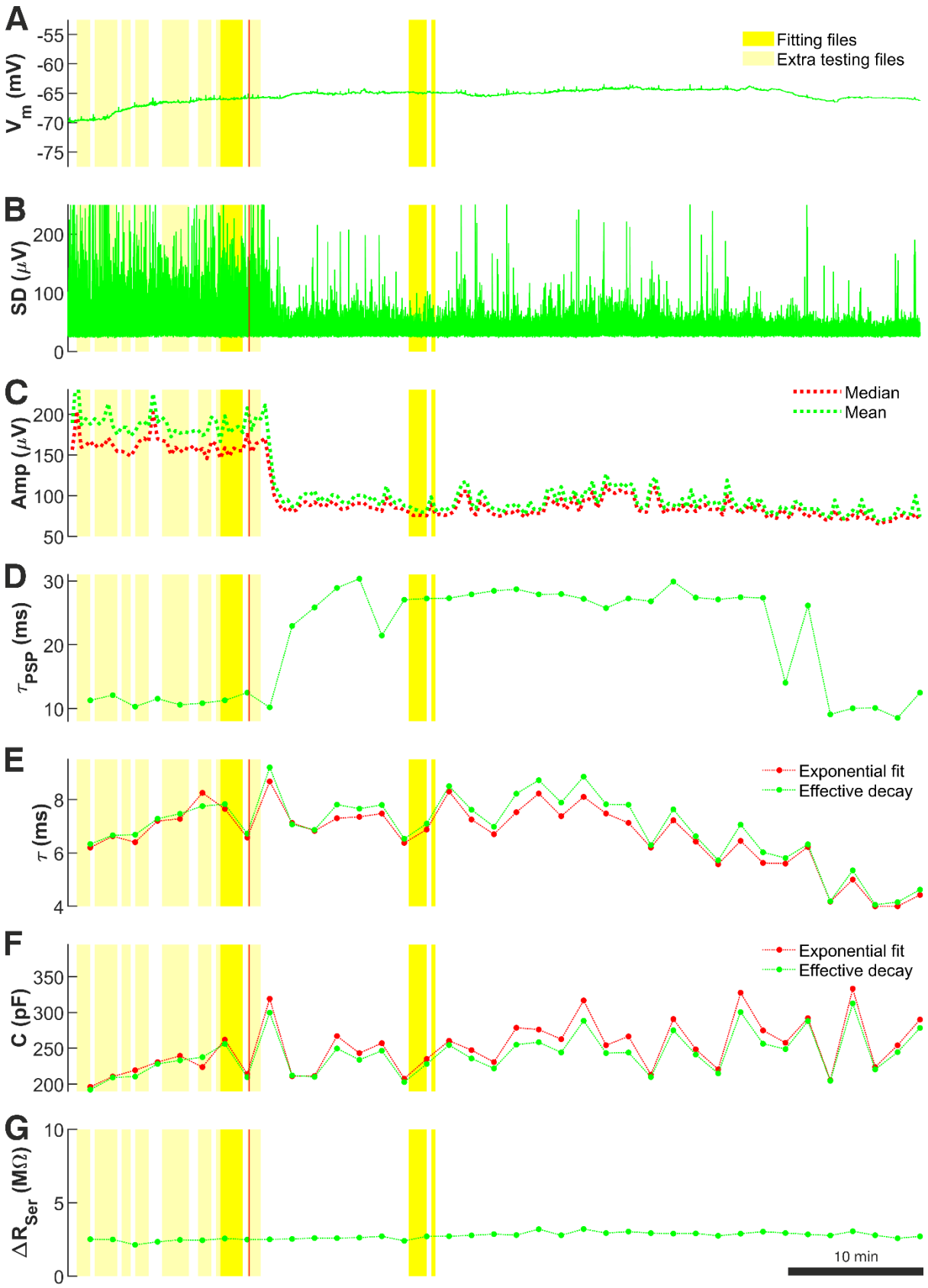

Supplementary Figure 8: Cell p125a (layer 2/3). Recording quality measures used to select 'noise with minis' and 'noise-alone' sweeps.

Panels A-G as for Figure 2 and Supplementary Figure 2. Data were averaged over 100-second-long windows (5 recording sweeps of 20 s each) in panels D-G; duration 3800 s. Some transiently extra noisy data due to temporary recording instability were excluded from the ‘noise-alone’ epoch.

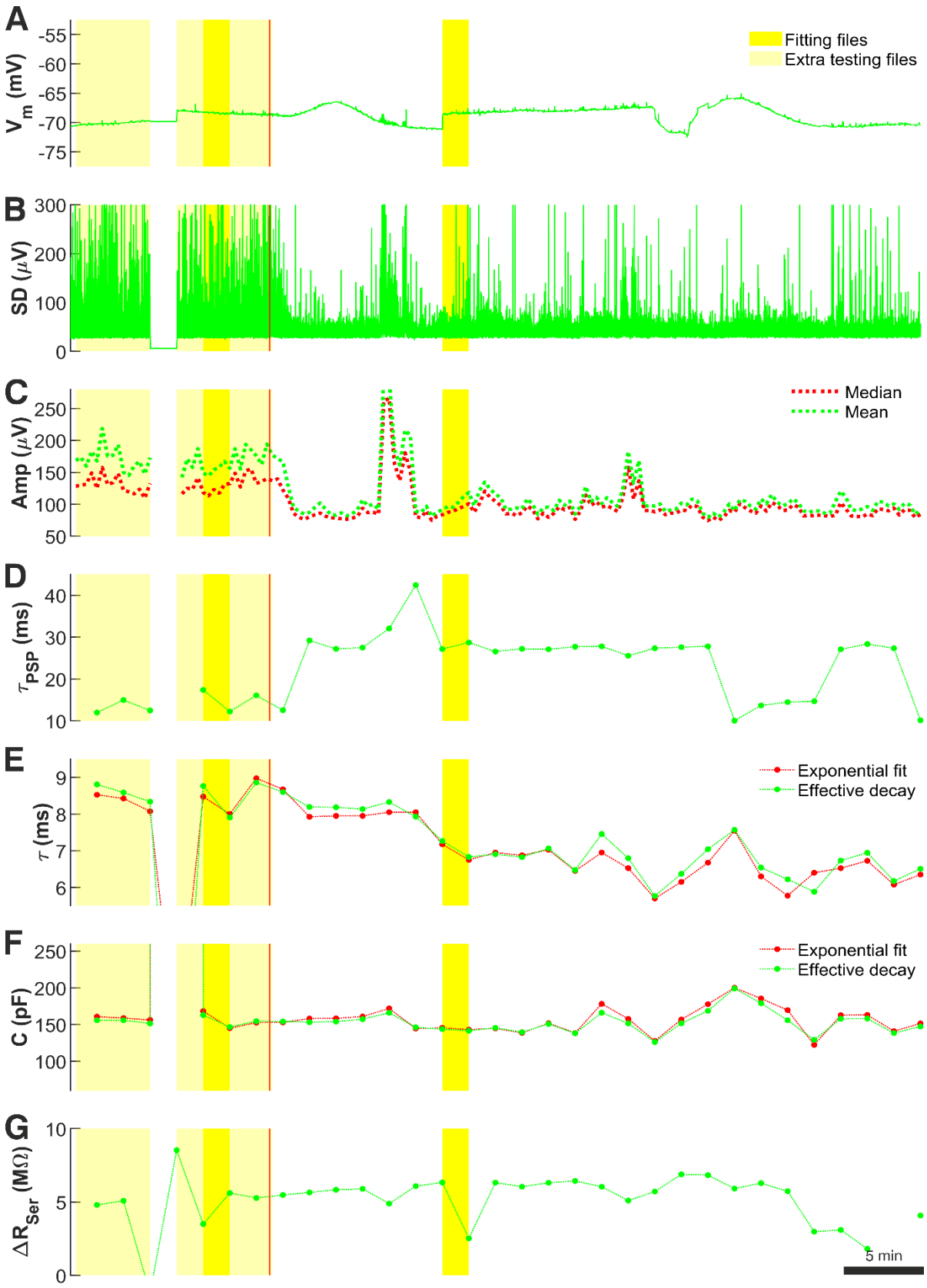

Supplementary Figure 9: Cell p127c (layer 2/3). Recording quality measures used to select 'noise with minis' and 'noise-alone' sweeps.

1141 Panels A-G as for Figure 2 and Supplementary Figure 2. Data were averaged over 100-second-long

1142 windows (5 recording sweeps of 20 s each) in panels D-G; duration 3200 s.

1143

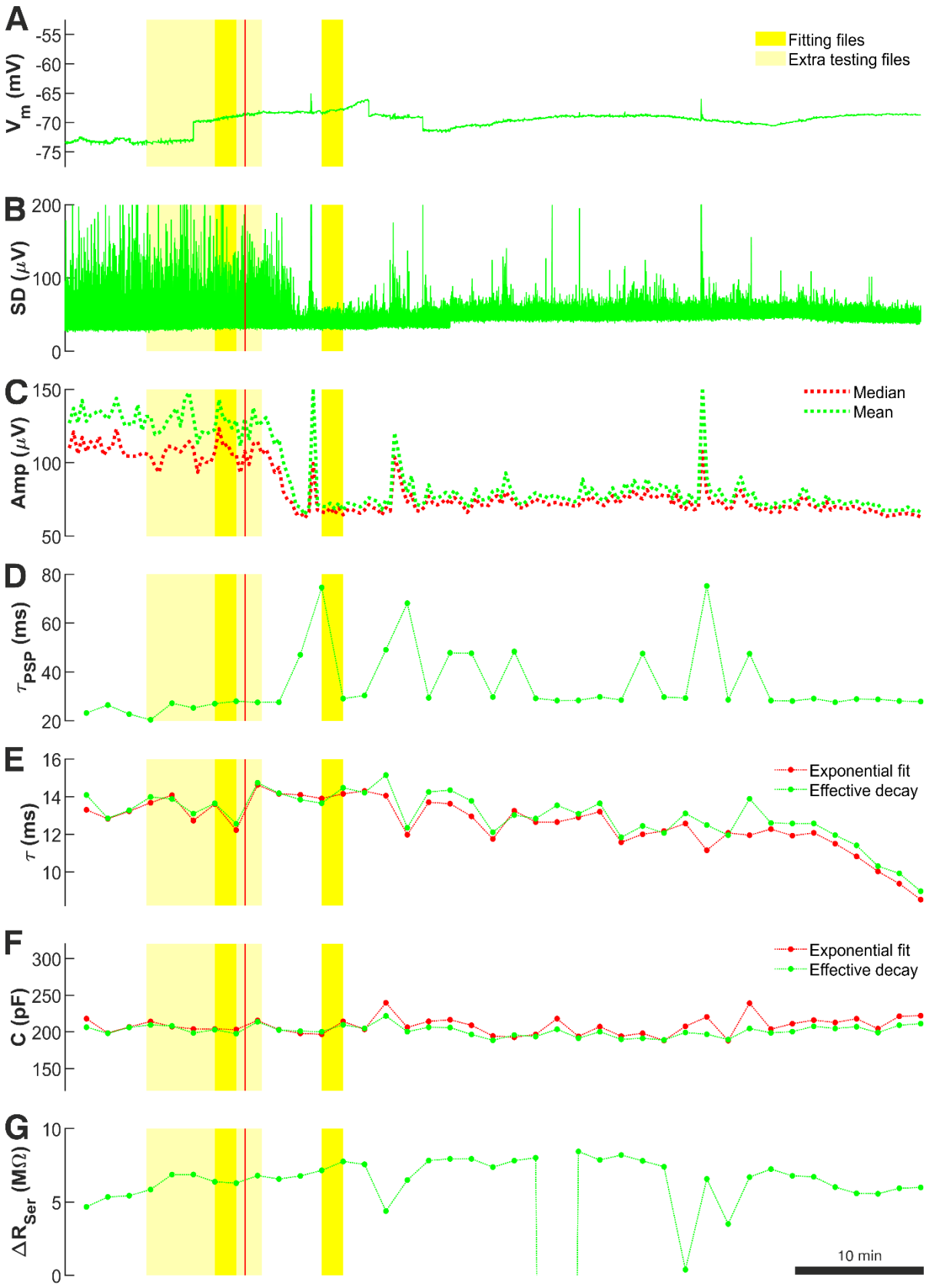

Supplementary Figure 11: Cell p129a (layer 5). Recording quality measures used to select 'noise with minis' and 'noise-alone' sweeps.

1147 Panels A-G as for Figure 2 and Supplementary Figure 2. Data were averaged over 100-second-long

1148 windows (5 recording sweeps of 20 s each) in panels D-G; duration 4000 s.

1149

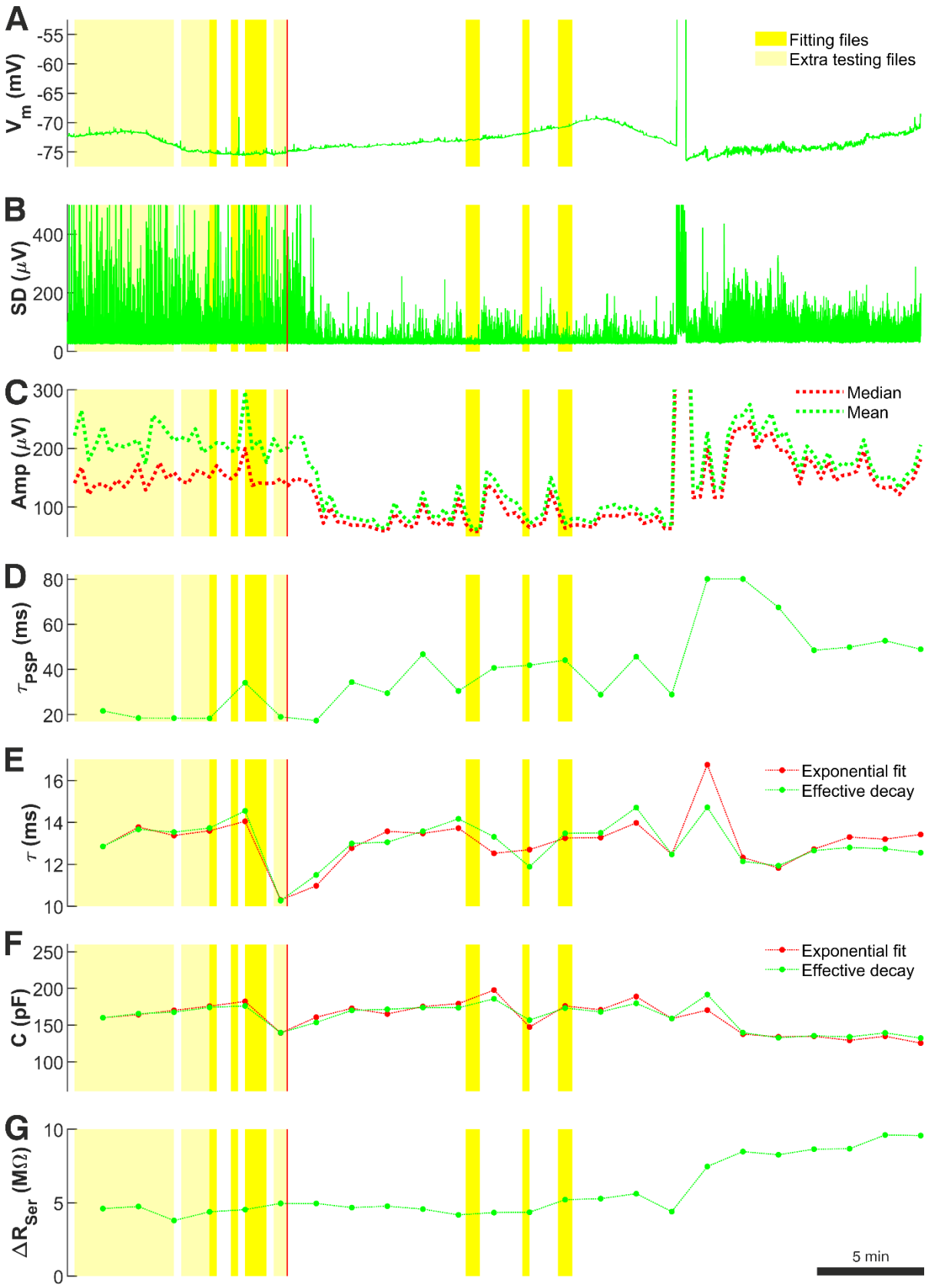

Supplementary Figure 12: Cell p131a (layer 2/3). Recording quality measures used to select 'noise with minis' and 'noise-alone' sweeps.

Panels A-G as for Figure 2 and Supplementary Figure 2. Data were averaged over 100-second-long windows (5 recording sweeps of 20 s each) in panels D-G; duration 2400 s. Fit epoch is fragmented due to noisy segments, with transient recording instability, being excluded.

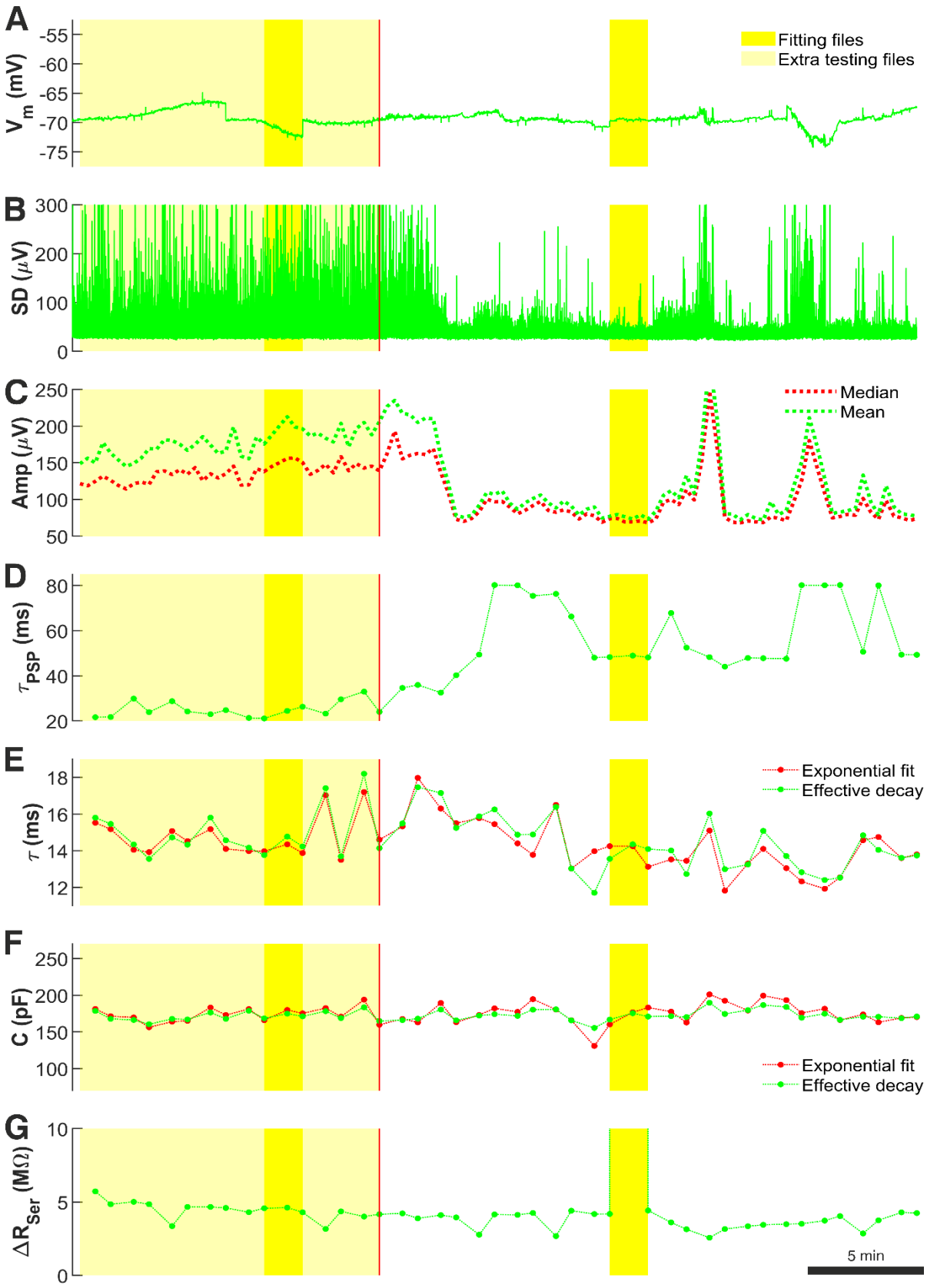

Supplementary Figure 13: Cell p131c (layer 2/3). Recording quality measures used to select 'noise with minis' and 'noise-alone' sweeps.

1160 Panels A-G as for Figure 2 and Supplementary Figure 2. Data were averaged over 100-second-long

1161 windows (5 recording sweeps of 20 s each) in panels D-G; duration 2200 s.

1162

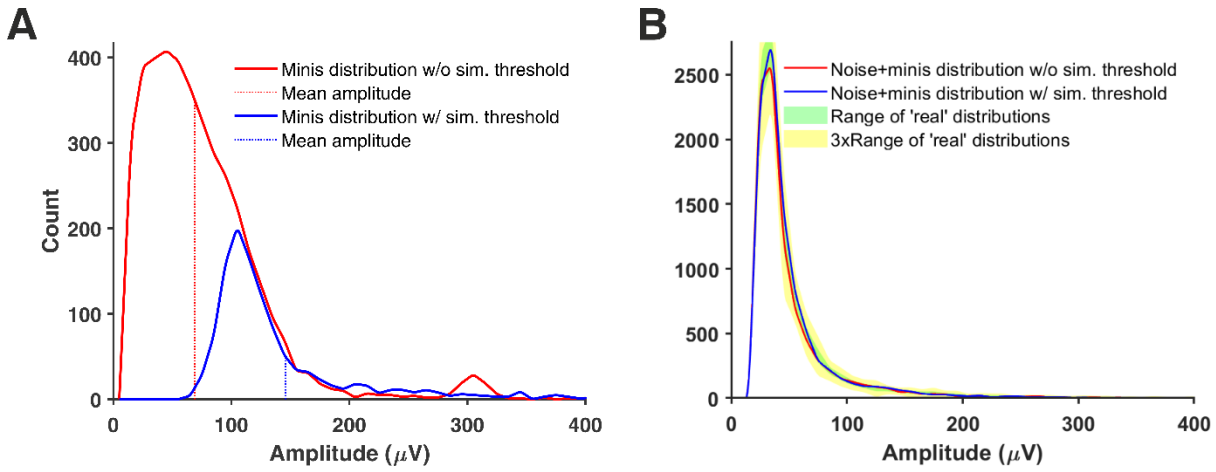

Supplementary figure 14: Non-uniqueness of simulated minis distributions.

(A) Two amplitude distributions of simulated minis events generated by the GA using a lower limit on simulated amplitudes of 10 µV (red histogram; termed as without simulation threshold) or 60 µV simulation threshold (blue histogram).

(B) Distributions of mini-like events detected in a ’noise with simulated minis’ voltage traces corresponding to the two minis source distributions in (A). Event histograms are shown superimposed on the full range of ‘real’ (‘noise with real minis’) distributions. The two distributions clearly fall within the range of ‘real’ distributions albeit being generated by two very different source distributions. Recordings obtained from cell p131c (layer 2/3).

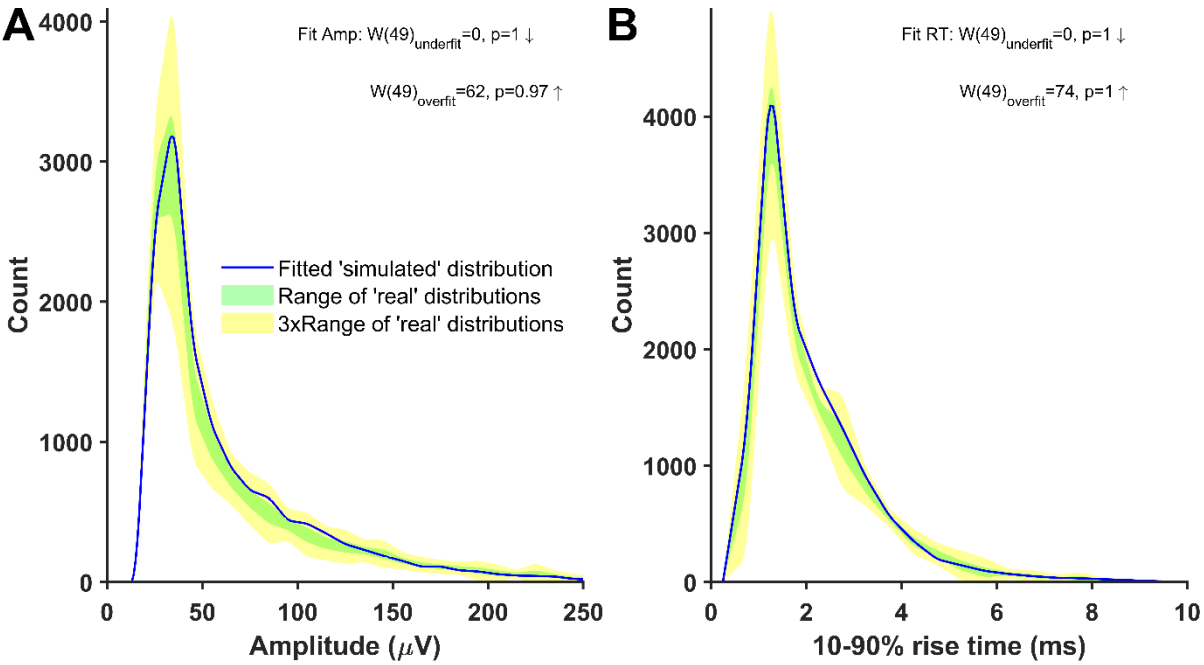

Supplementary figure 15: Distributions of mini-like events detected in a ’noise with simulated minis’ voltage trace that closely matched ‘noise with real minis‘ recordings and passed statistical good fit tests, i.e. did not ‘fail’ the poor fit (underfit) unidirectional tests (it could not be ‘picked out’ either objectively or ‘double-blind’ from the ‘noise with real minis’ distributions found with the same detection parameters).

Parameters of simulated minis were controlled by the GA; ’noise-alone’ recording obtained from cell p103a (layer 5). Downward arrows indicate ‘simulated’ SAD < ‘real’ SAD. Upward arrows indicate ‘simulated’ SAD > ‘real’ SAD. The ‘underfit’ (poor fit) unidirectional test (top) involves a comparison with the ‘worst-performing’ (highest between-file) ‘real’ SAD file (most discrepant from the others; the null hypothesis is ‘simulated’ SAD does not exceed ‘real’ SAD). The ‘overfit’ unidirectional test (bottom) involves a comparison with the ‘best-performing’ (lowest between-file) ‘real’ SAD (least discrepant from the others; the null hypothesis is ‘simulated’ SAD is not smaller than ‘real’ SAD), but ‘failure’ of this test ($p < 0.05$ Bonferroni-corrected, difference not by chance) does not indicate a fit rejection.

(A) Amplitude and (B) 10-90% rise time distributions of mini-like events detected in a ’noise with simulated minis’ voltage trace (blue curve).

1191

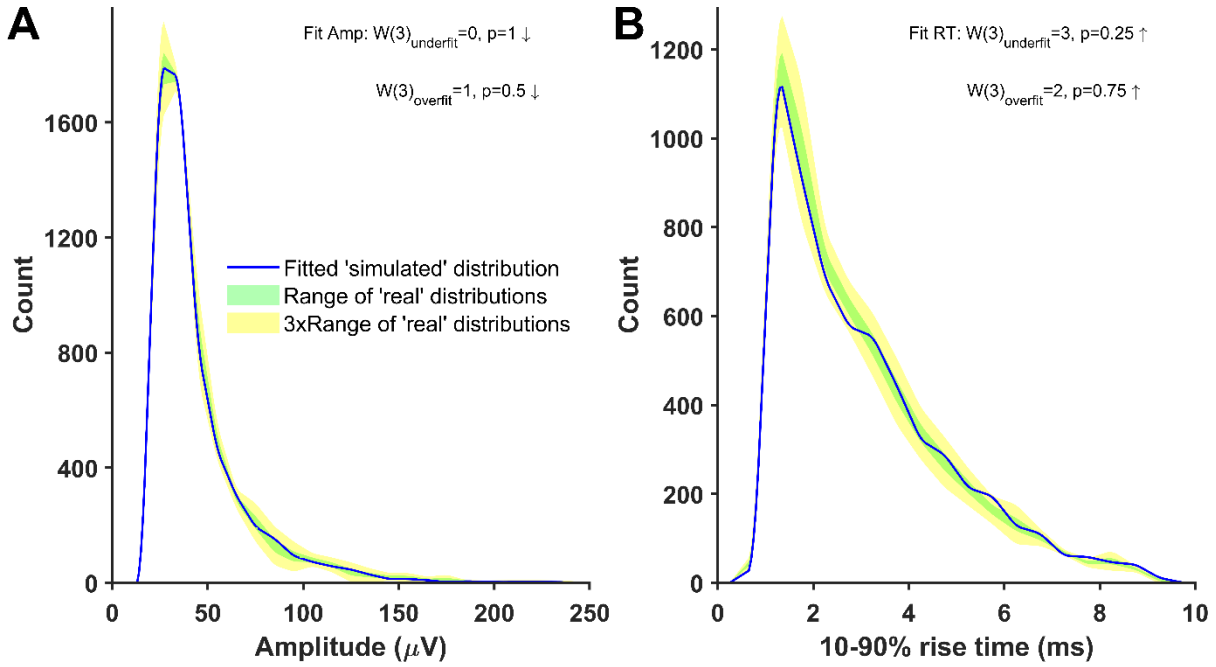

1192

1193 **Supplementary Figure 16:** Cell p108a (layer 5), distributions of mini-like events detected in a ’noise

1194 with simulated minis’ voltage trace that closely matched ‘noise with real minis‘ recordings.

1195 Parameters of simulated minis controlled by GA. Down arrow: ‘simulated’ SAD < ‘real’ SAD (up:

1196 ‘simulated’ > ‘real’; Suppl. Fig. 15).

1197

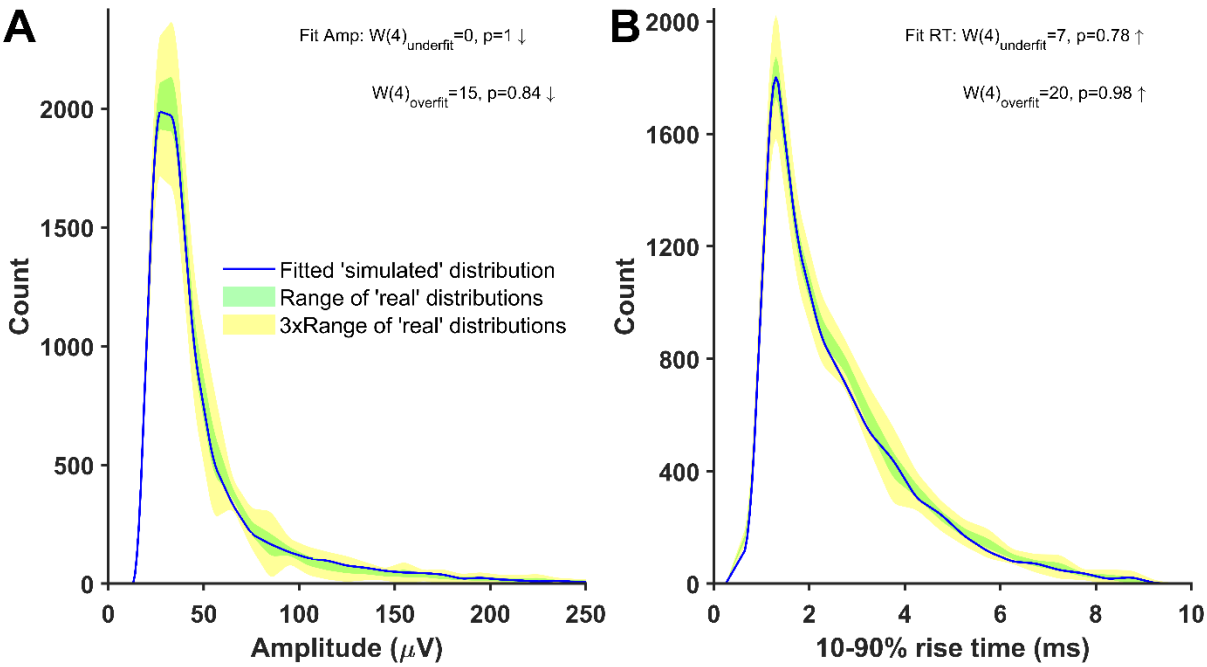

Supplementary Figure 17: Cell p108b (layer 5), distributions of mini-like events detected in a 'noise with simulated minis' voltage trace that closely matched 'noise with real minis' recordings. Parameters of simulated minis controlled by GA. Down arrow: 'simulated' SAD < 'real' SAD (up: 'simulated' > 'real'; Suppl. Fig. 15).

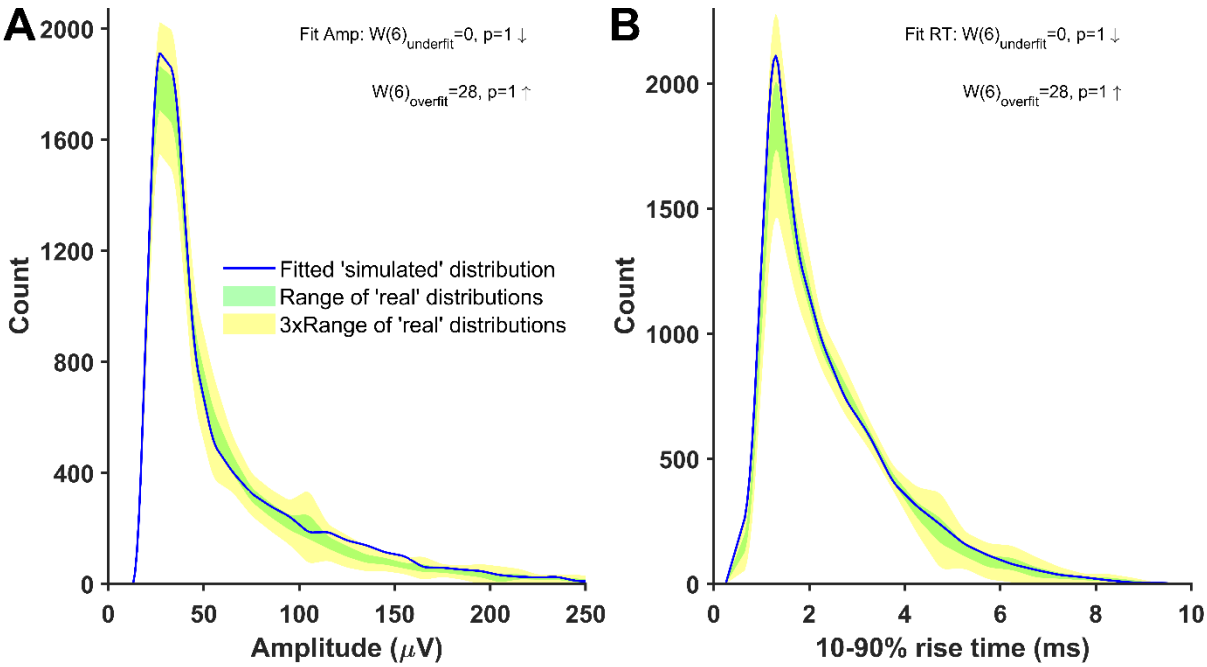

Supplementary Figure 18: Cell p108c (layer 5), distributions of mini-like events detected in a 'noise with simulated minis' voltage trace that closely matched 'noise with real minis' recordings. Parameters of simulated minis controlled by GA. Down arrow: 'simulated' SAD < 'real' SAD (up: 'simulated' > 'real'; Suppl. Fig. 15).

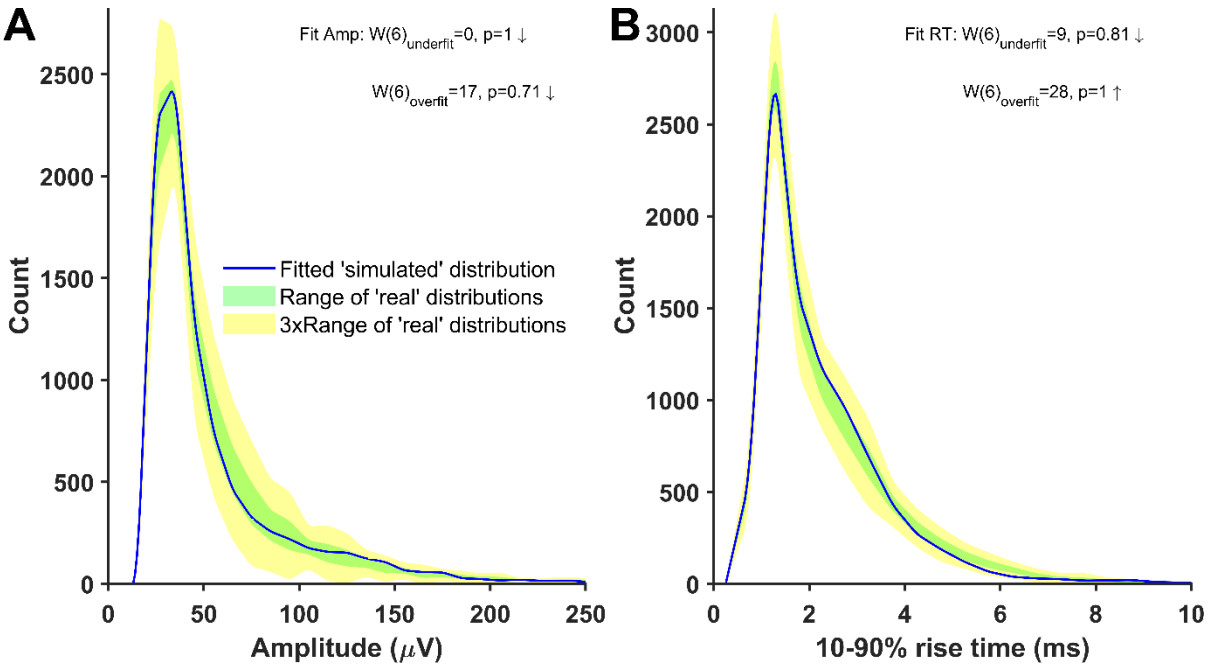

Supplementary Figure 19: Cell p120b (layer 2/3), distributions of mini-like events detected in a 'noise with simulated minis' voltage trace that closely matched 'noise with real minis' recordings. Parameters of simulated minis controlled by GA. Down arrow: 'simulated' SAD < 'real' SAD (up: 'simulated' > 'real'; Suppl. Fig. 15).

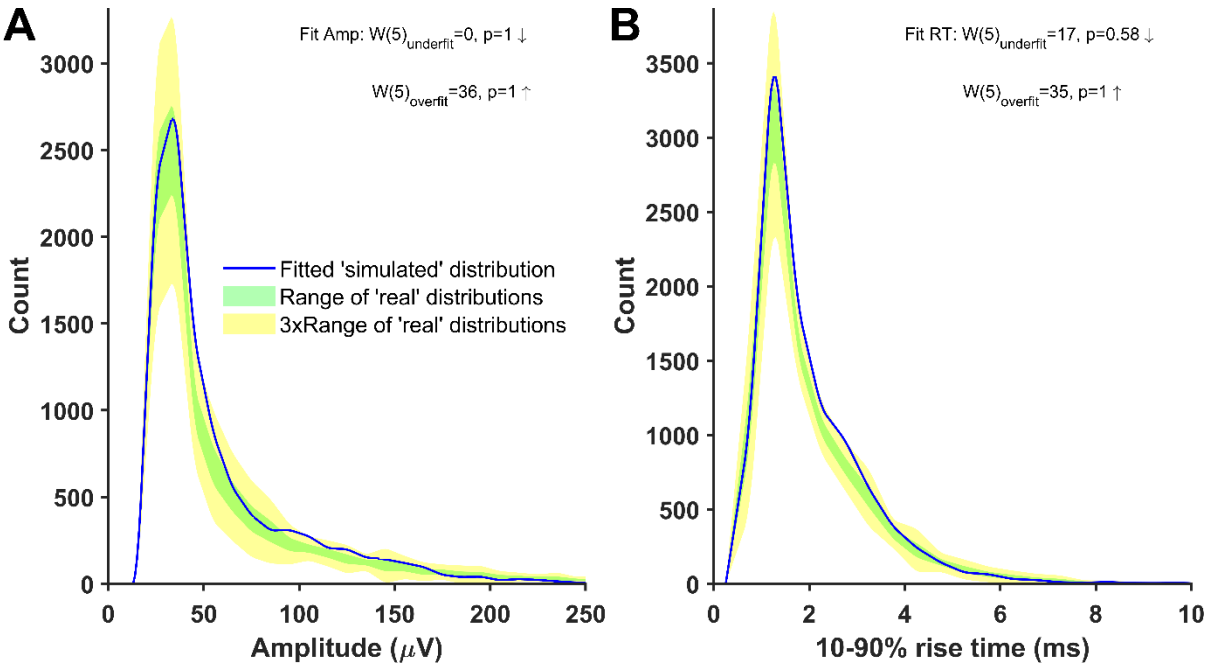

Supplementary Figure 20: Cell p122a (layer 2/3), distributions of mini-like events detected in a 'noise with simulated minis' voltage trace that closely matched 'noise with real minis' recordings. Parameters of simulated minis controlled by GA. Down arrow: 'simulated' SAD < 'real' SAD (up: 'simulated' > 'real'; Suppl. Fig. 15).

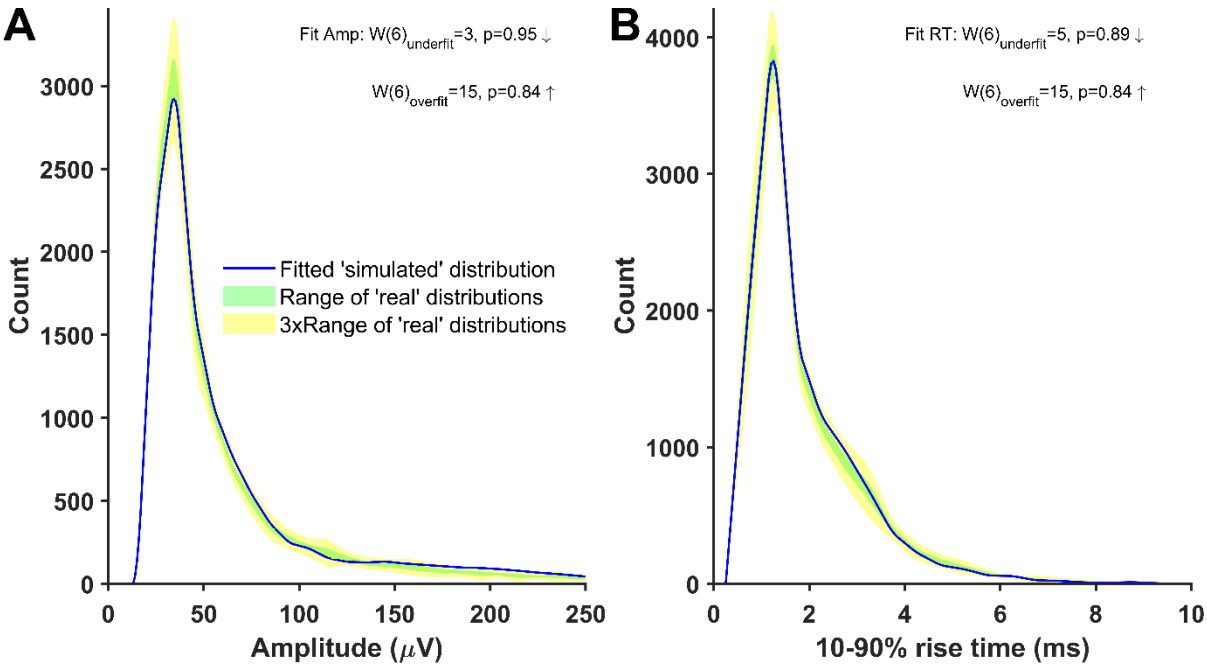

Supplementary Figure 21: Cell p124b (layer 5), distributions of mini-like events detected in a ’noise with simulated minis’ voltage trace that closely matched ‘noise with real minis‘ recordings. Parameters of simulated minis controlled by GA. Down arrow: ‘simulated’ SAD < ‘real’ SAD (up: ‘simulated’ > ‘real’; Suppl. Fig. 15).

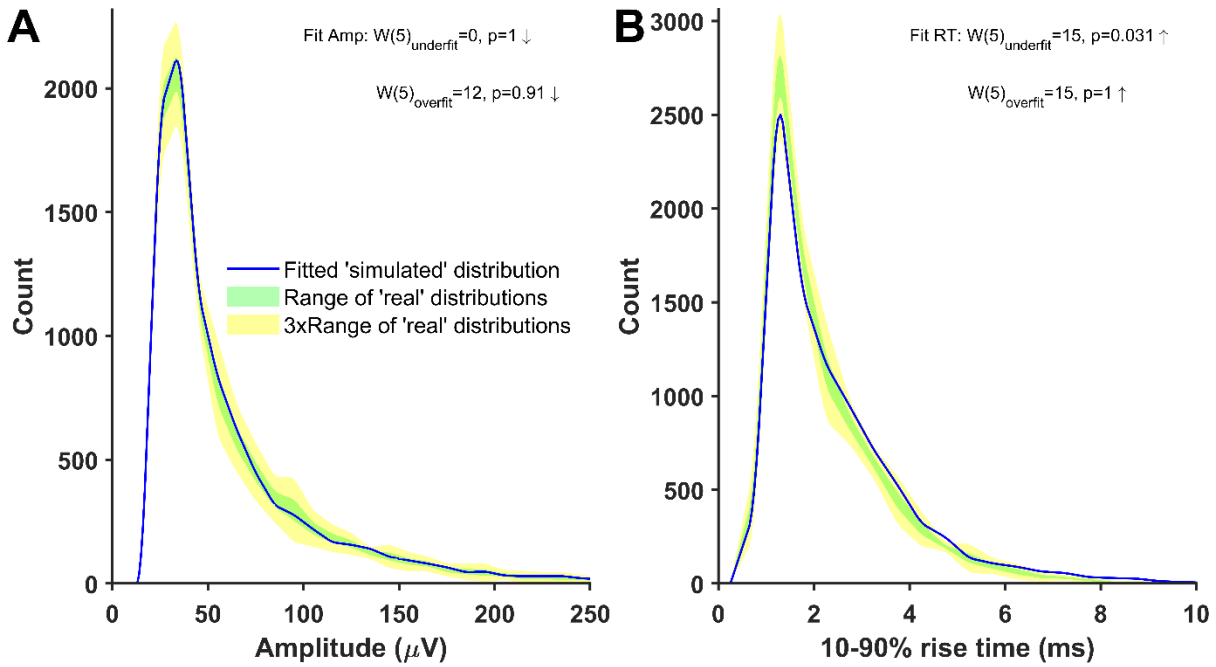

Supplementary Figure 22: Cell p125a (layer 2/3), distributions of mini-like events detected in a 'noise with simulated minis' voltage trace that closely matched 'noise with real minis' recordings. Parameters of simulated minis controlled by GA. Down arrow: 'simulated' SAD < 'real' SAD (up: 'simulated' > 'real'; Suppl. Fig. 15).

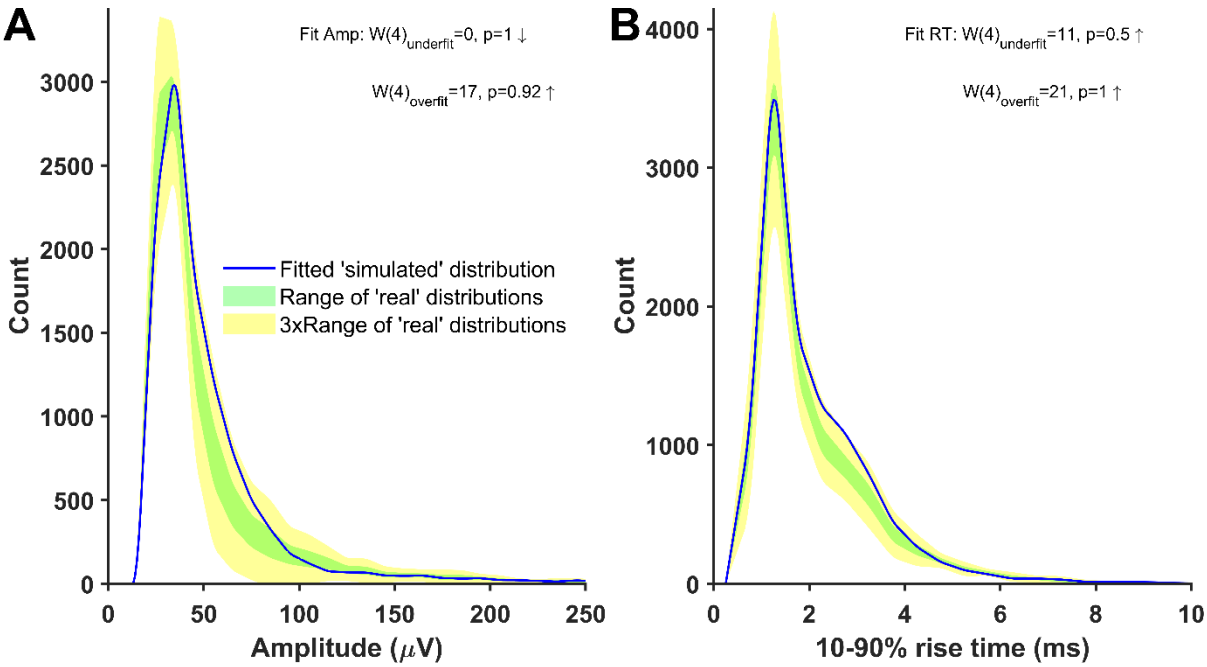

Supplementary Figure 23: Cell p127c (layer 2/3), distributions of mini-like events detected in a 'noise with simulated minis' voltage trace that closely matched 'noise with real minis' recordings. Parameters of simulated minis controlled by GA. Down arrow: 'simulated' SAD < 'real' SAD (up: 'simulated' > 'real'; Suppl. Fig. 15).

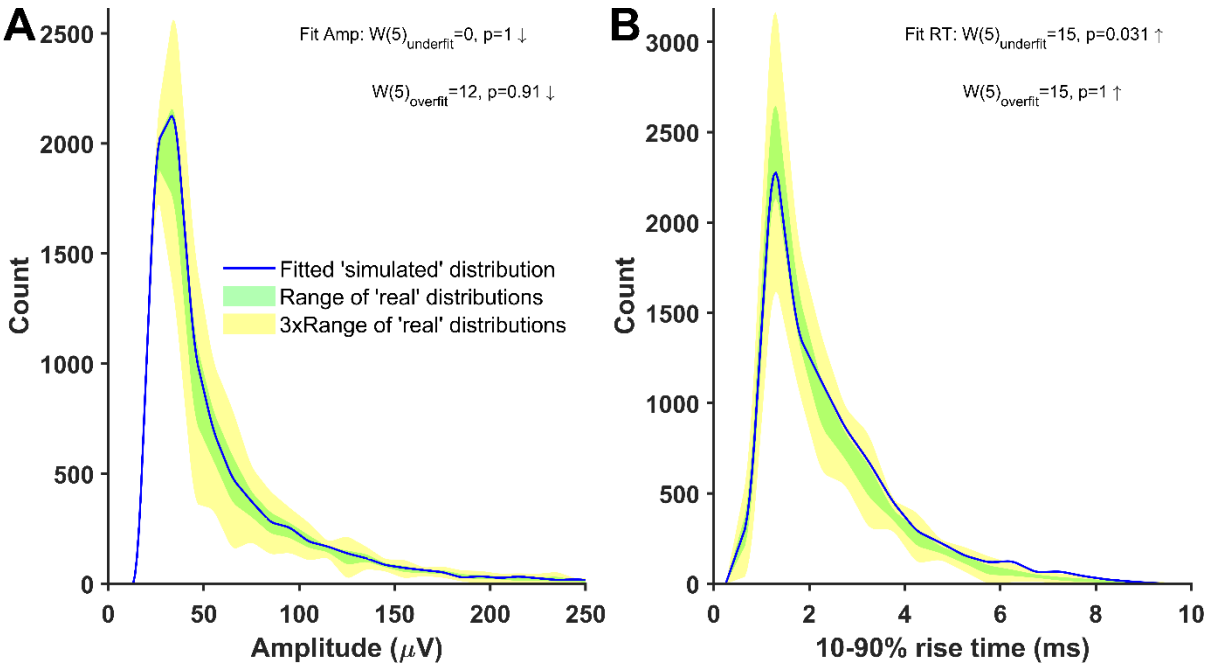

Supplementary Figure 24: Cell p128c (layer 2/3), distributions of mini-like events detected in a 'noise with simulated minis' voltage trace that closely matched 'noise with real minis' recordings. Parameters of simulated minis controlled by GA. Down arrow: 'simulated' SAD < 'real' SAD (up: 'simulated' > 'real'; Suppl. Fig. 15).

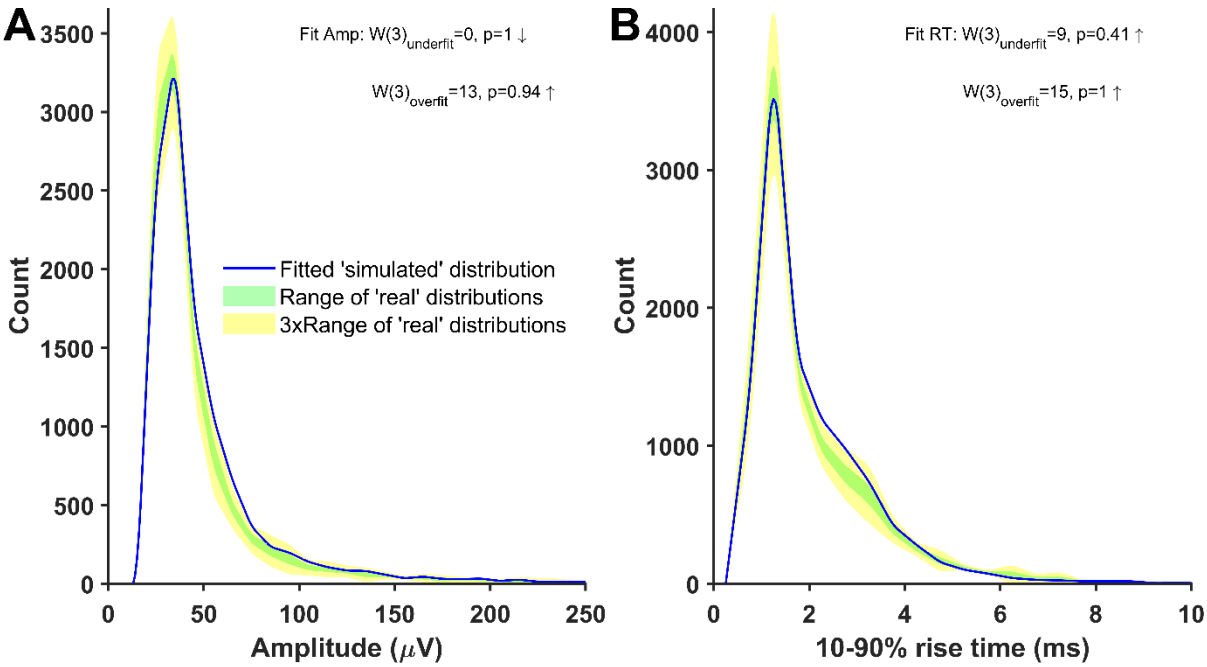

Supplementary Figure 25: Cell p129a (layer 5), distributions of mini-like events detected in a ’noise with simulated minis’ voltage trace that closely matched ‘noise with real minis‘ recordings. Parameters of simulated minis controlled by GA. Down arrow: ‘simulated’ SAD < ‘real’ SAD (up: ‘simulated’ > ‘real’; Suppl. Fig. 15).

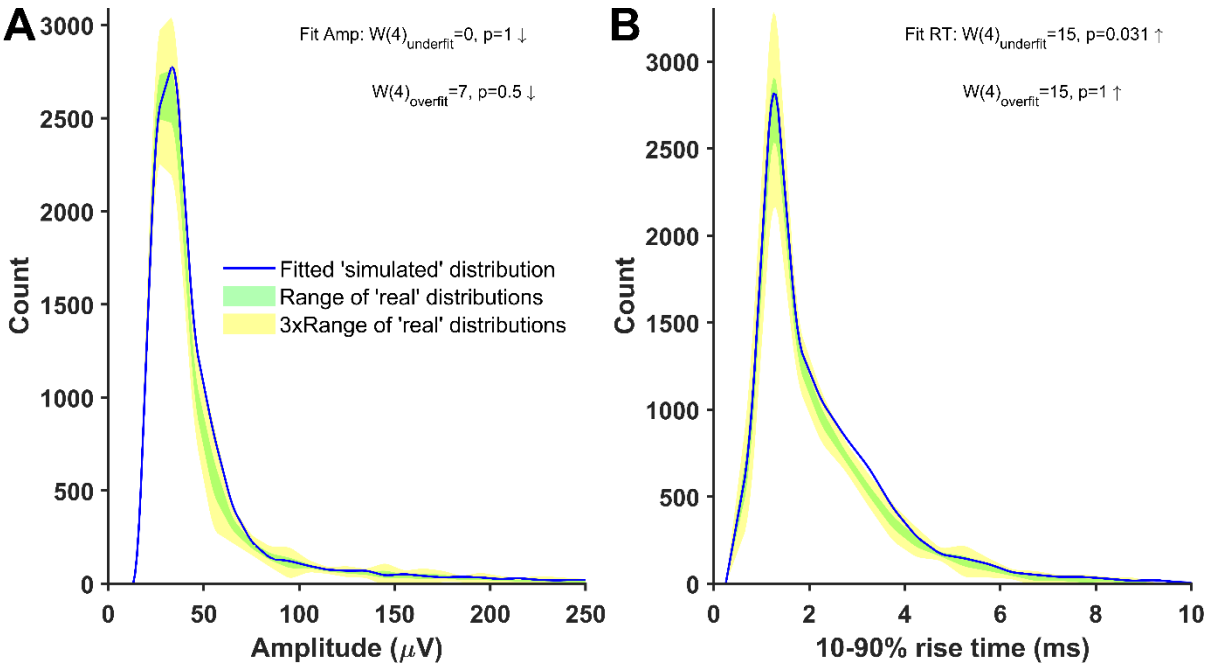

Supplementary Figure 26: Cell p131a (layer 2/3), distributions of mini-like events detected in a 'noise with simulated minis' voltage trace that closely matched 'noise with real minis' recordings. Parameters of simulated minis controlled by GA. Down arrow: 'simulated' SAD < 'real' SAD (up: 'simulated' > 'real'; Suppl. Fig. 15).

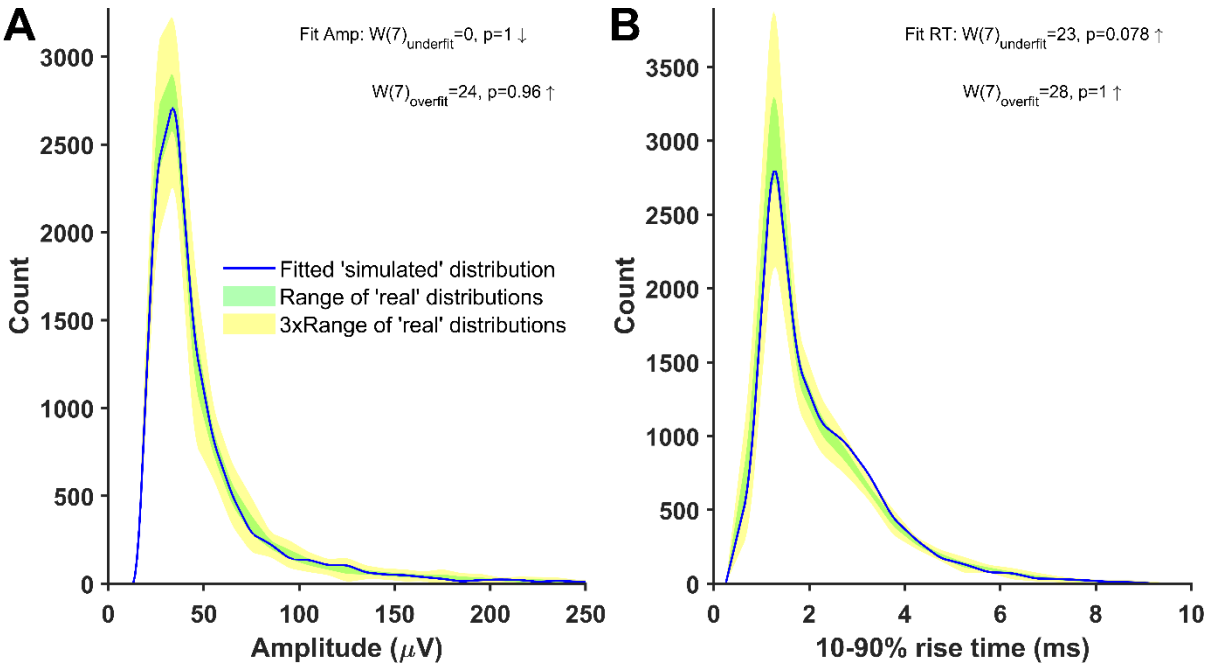

Supplementary Figure 27: Cell p131c (layer 2/3), distributions of mini-like events detected in a 'noise with simulated minis' voltage trace that closely matched 'noise with real minis' recordings. Parameters of simulated minis controlled by GA. Down arrow: 'simulated' SAD < 'real' SAD (up: 'simulated' > 'real'; Suppl. Fig. 15).

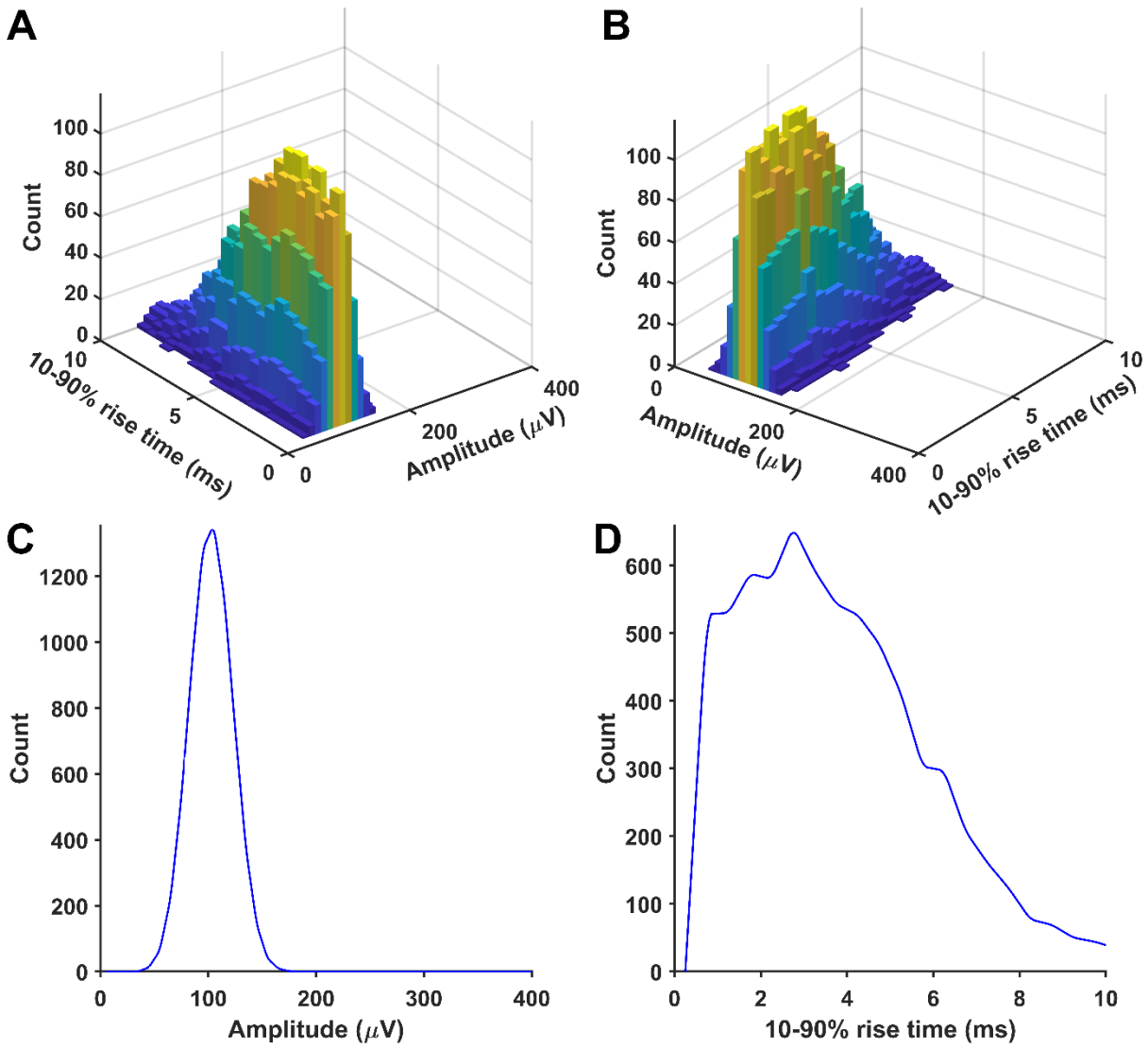

Supplementary Figure 28: An example of a distribution of randomly selected simulated minis that was used to produce a close match between distributions of mini-like events detected in a 'noise with simulated minis' voltage trace (40 µV lower limit on simulated amplitudes) and a 'noise with real minis' recording for cell p103a (layer 5).

(A) and (B) Joint amplitude and 10-90% rise time distribution of simulated minis (two views).

(C) 'Marginal' amplitude and (D) 10-90% rise time distributions (all 2-D bins projected onto that axis).

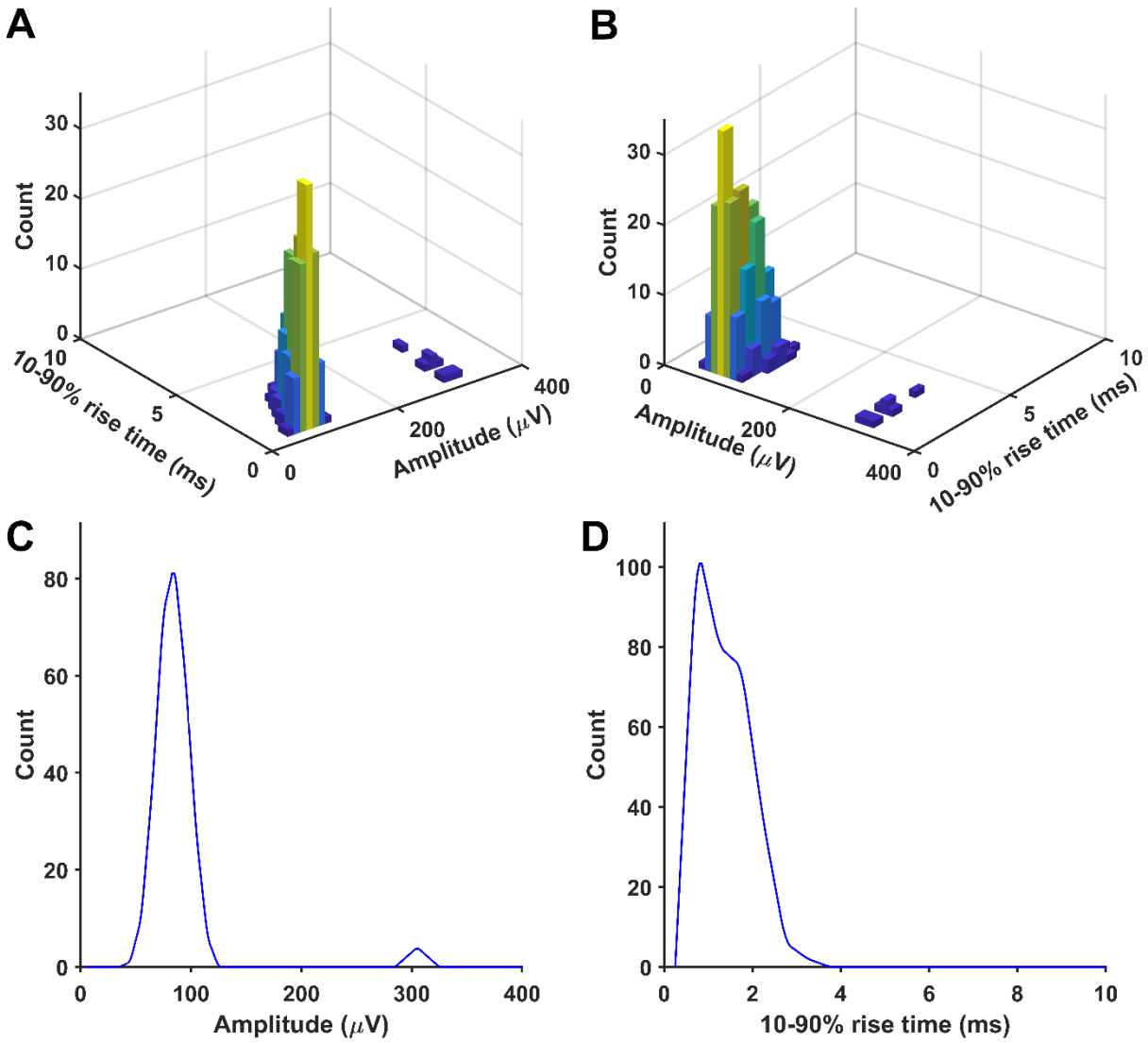

Supplementary Figure 29: An example of a distribution of randomly selected simulated minis that was used to produce a close match between distributions of mini-like events detected in a 'noise with simulated minis' voltage trace (40 µV lower limit on simulated amplitudes) and a 'noise with real minis' recording for cell p106b (layer 5).

Panels as for Supplementary Figure 28.

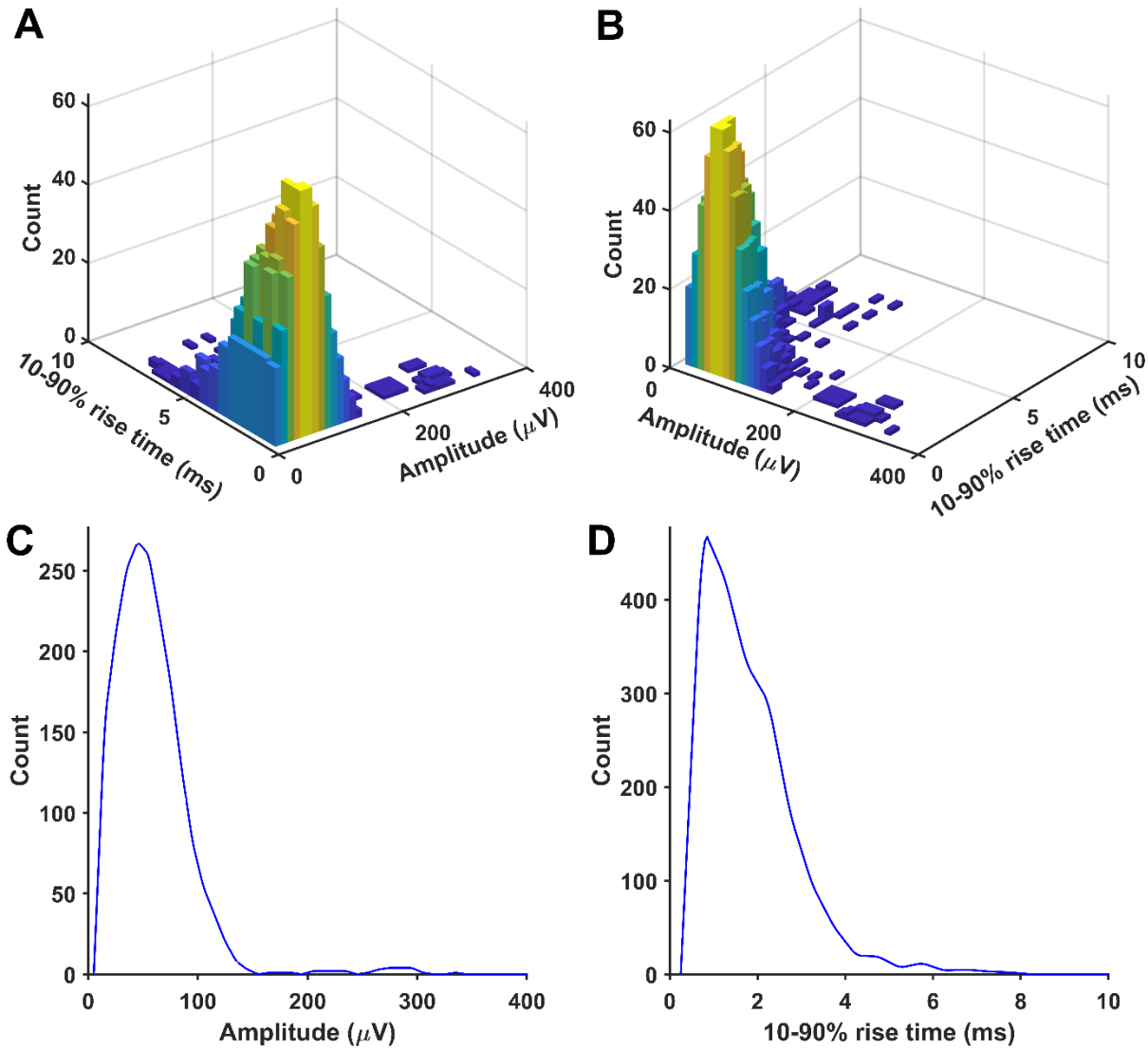

1278

1279 **Supplementary Figure 30:** An example of a distribution of randomly selected simulated minis that

1280 was used to produce a close match between distributions of mini-like events detected in a 'noise

1281 with simulated minis' voltage trace (10 µV lower limit on simulated amplitudes) and a 'noise with

1282 real minis' recording for cell p108a (layer 5).

1283 Panels as for Supplementary Figure 28.

1284

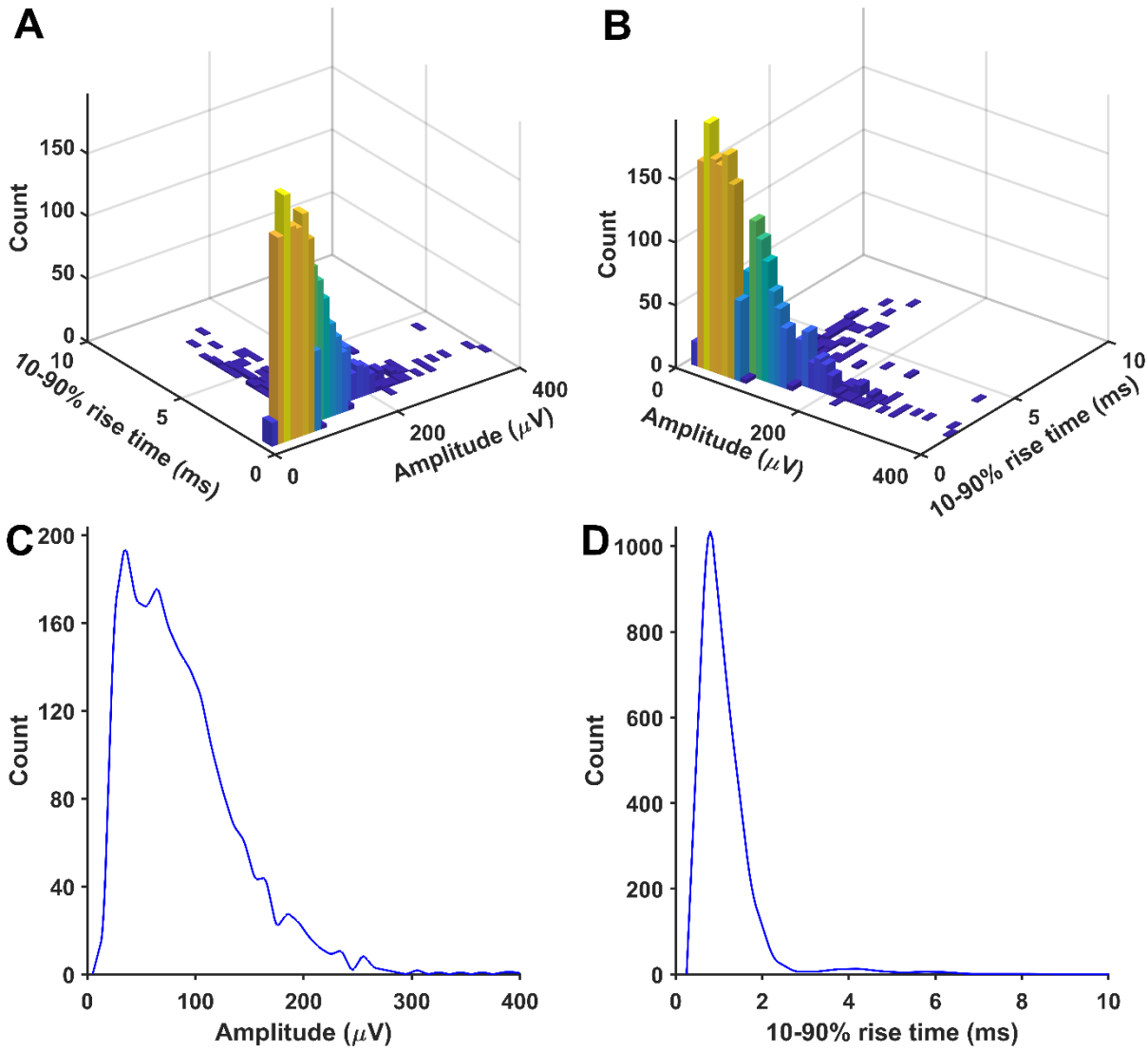

Supplementary Figure 31: An example of a distribution of randomly selected simulated minis that was used to produce a close match between distributions of mini-like events detected in a 'noise with simulated minis' voltage trace (10 µV lower limit on simulated amplitudes) and a 'noise with real minis' recording for cell p108b (layer 5).

Panels as for Supplementary Figure 28.

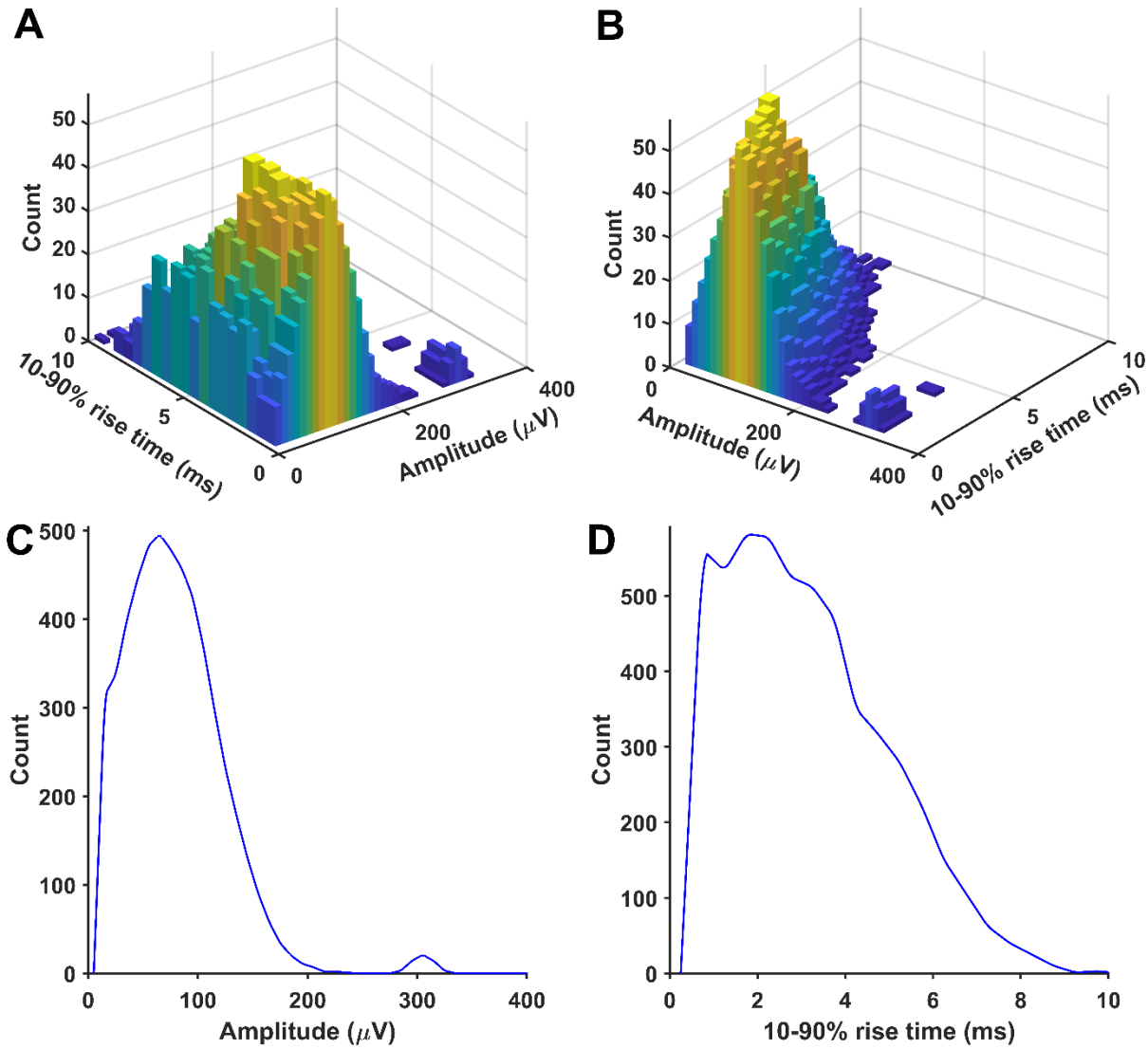

Supplementary Figure 32: An example of a distribution of randomly selected simulated minis that was used to produce a close match between distributions of mini-like events detected in a 'noise with simulated minis' voltage trace (10 µV lower limit on simulated amplitudes) and a 'noise with real minis' recording for cell p108c (layer 5).

Panels as for Supplementary Figure 28.

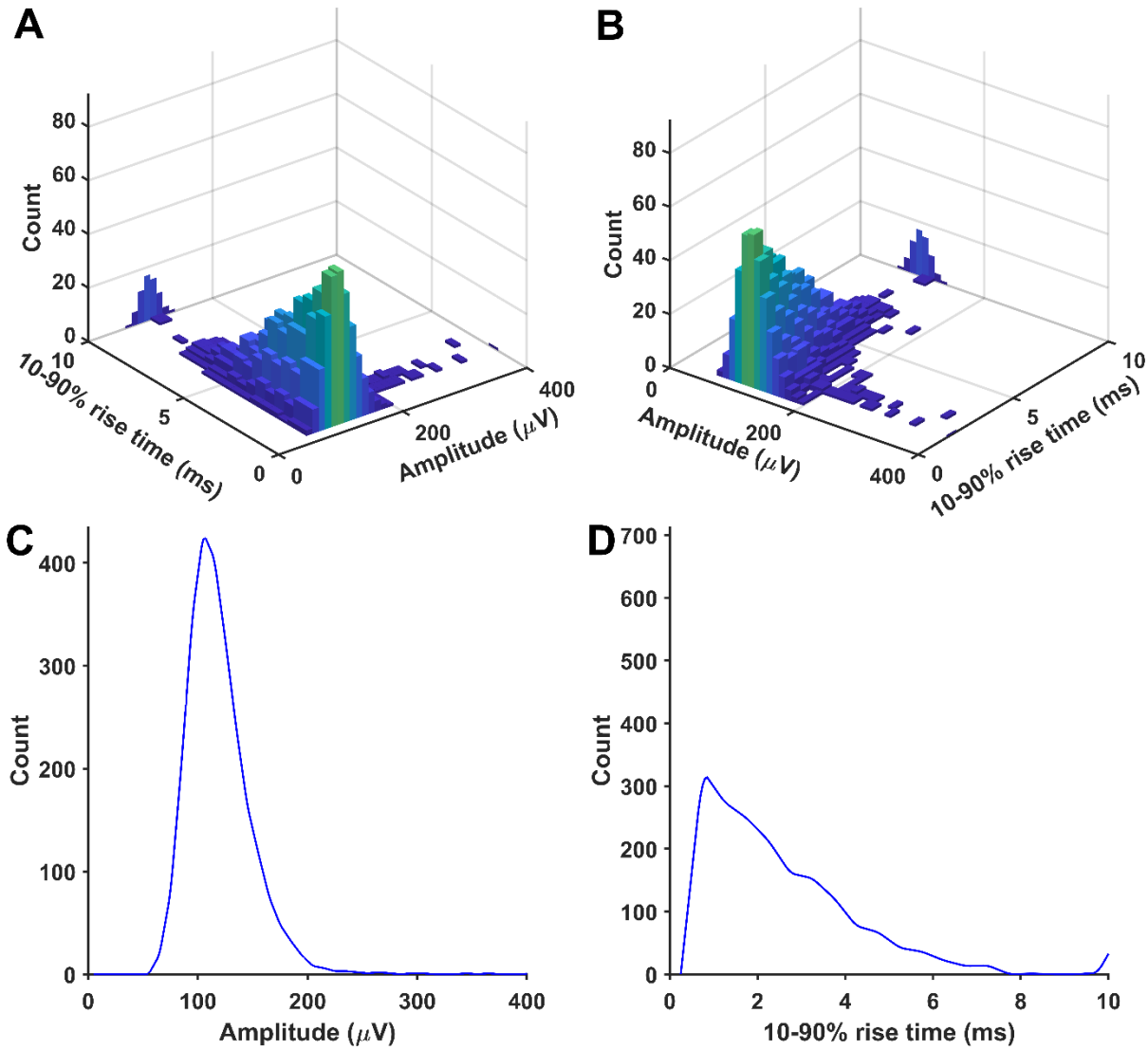

Supplementary Figure 33: An example of a distribution of randomly selected simulated minis that was used to produce a close match between distributions of mini-like events detected in a 'noise with simulated minis' voltage trace (60 µV lower limit on simulated amplitudes) and a 'noise with real minis' recording for cell p120b (layer 2/3).

Panels as for Supplementary Figure 28.

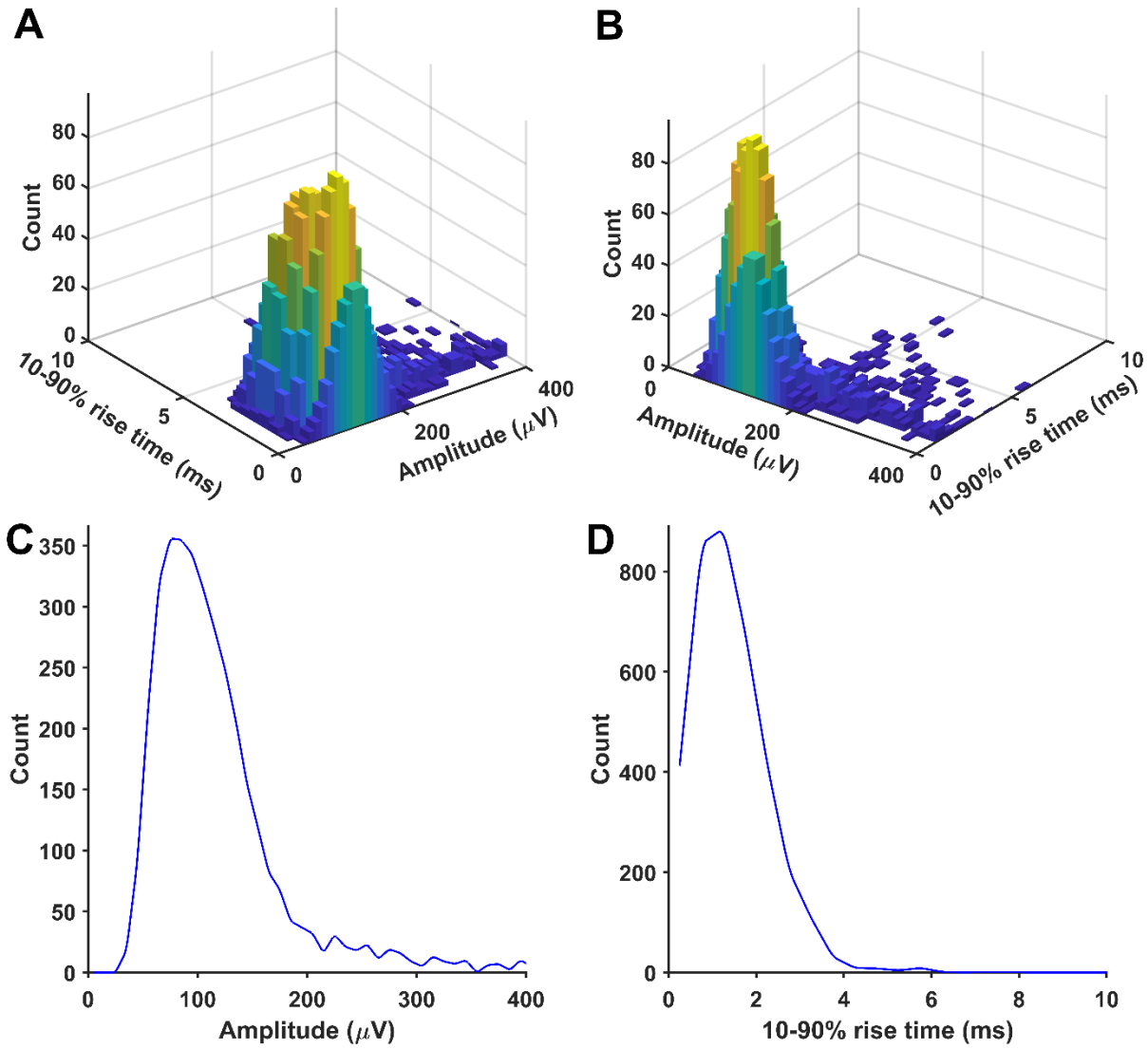

Supplementary Figure 34: An example of a distribution of randomly selected simulated minis that was used to produce a close match between distributions of mini-like events detected in a 'noise with simulated minis' voltage trace (30 µV lower limit on simulated amplitudes) and a 'noise with real minis' recording for cell p122a (layer 2/3).

Panels as for Supplementary Figure 28.

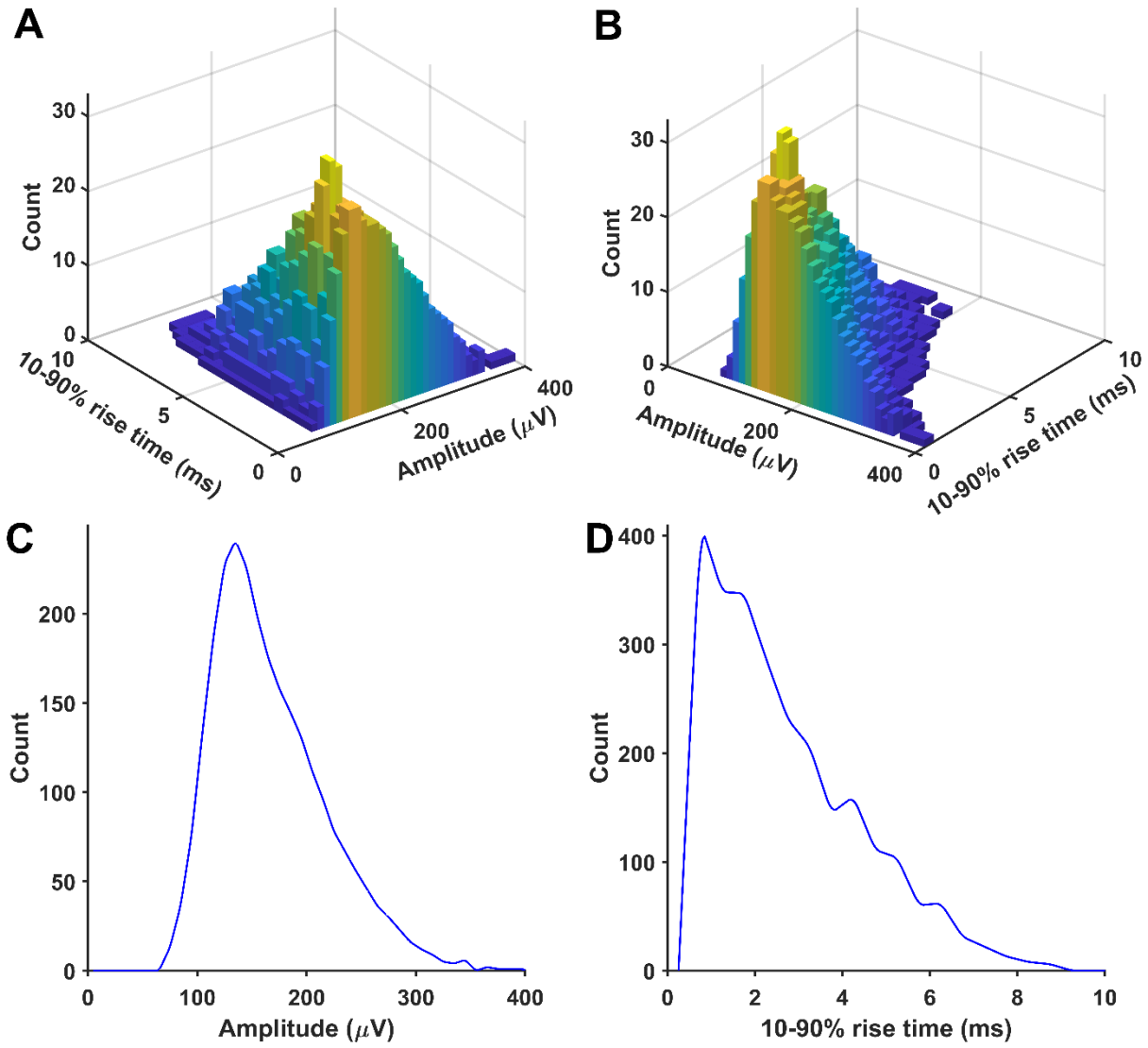

1313

1314 **Supplementary Figure 35:** An example of a distribution of randomly selected simulated minis that

1315 was used to produce a close match between distributions of mini-like events detected in a 'noise

1316 with simulated minis' voltage trace (40 µV lower limit on simulated amplitudes) and a 'noise with

1317 real minis' recording for cell p124b (layer 5).

1318 Panels as for Supplementary Figure 28.

1319

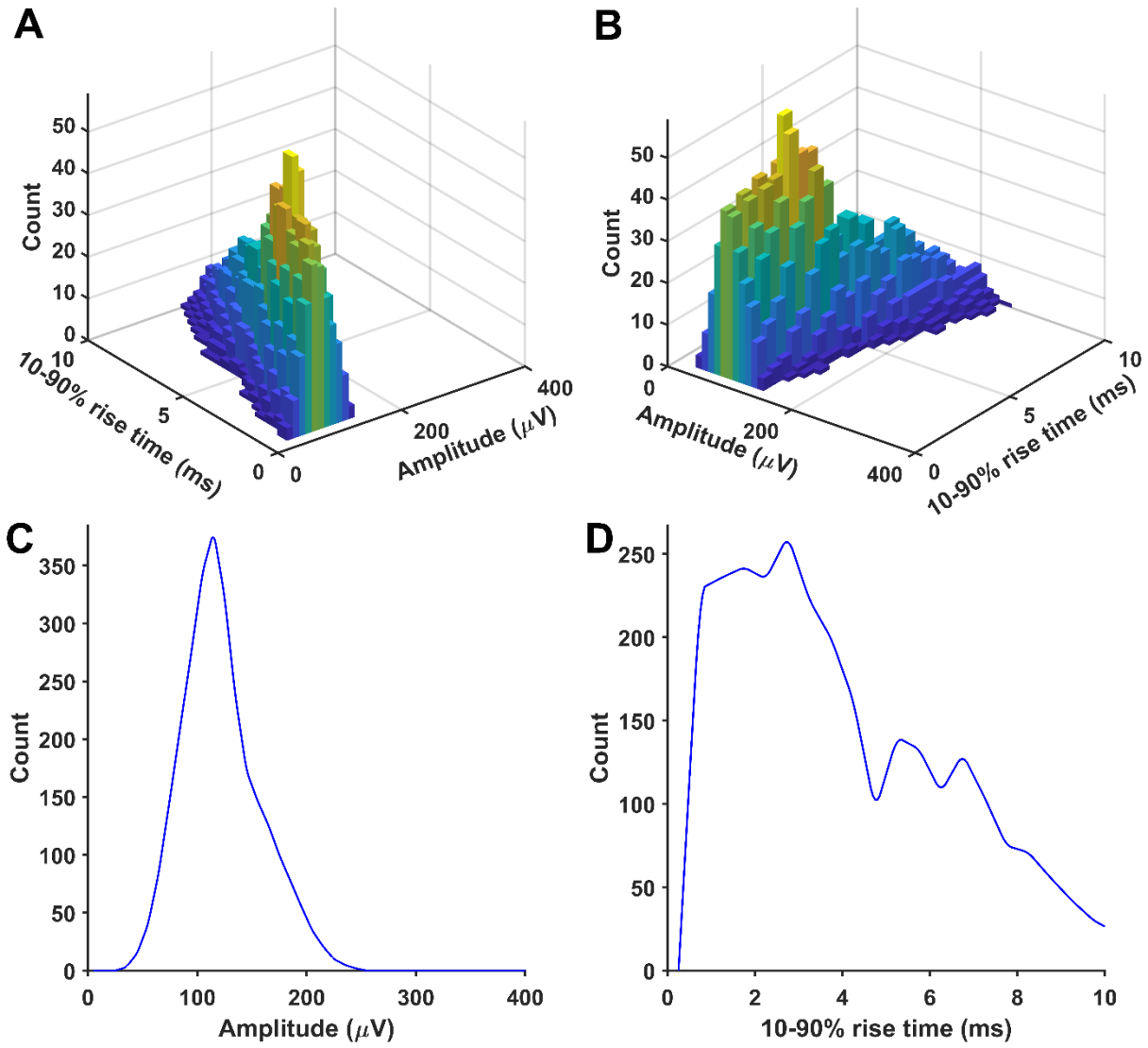

Supplementary Figure 36: An example of a distribution of randomly selected simulated minis that was used to produce a close match between distributions of mini-like events detected in a 'noise with simulated minis' voltage trace (30 µV lower limit on simulated amplitudes) and a 'noise with real minis' recording for cell p125a (layer 2/3).

Panels as for Supplementary Figure 28.

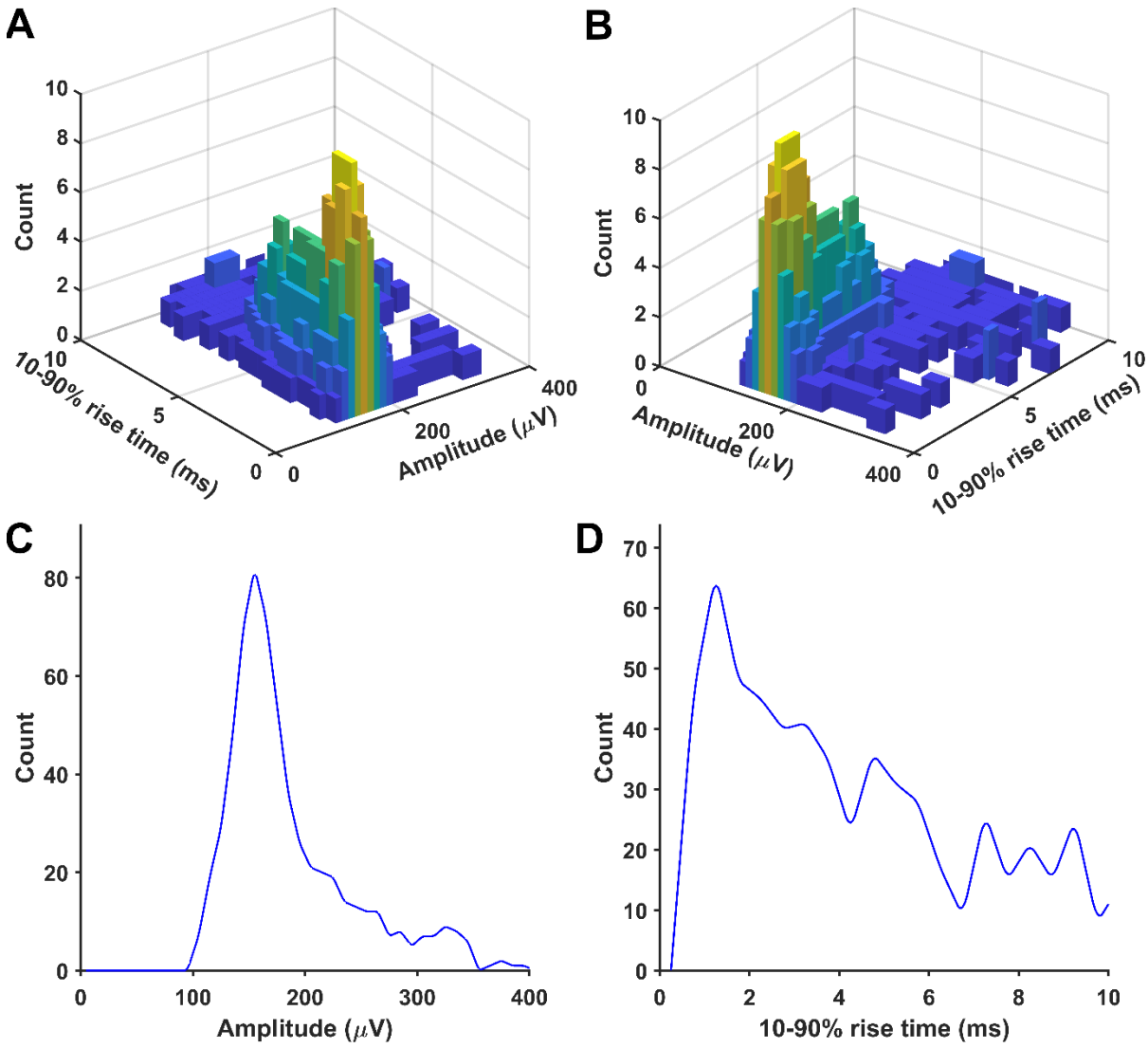

Supplementary Figure 37: An example of a distribution of randomly selected simulated minis that was used to produce a close match between distributions of mini-like events detected in a 'noise with simulated minis' voltage trace (100 µV lower limit on simulated amplitudes) and a 'noise with real minis' recording for cell p127c (layer 2/3).

Panels as for Supplementary Figure 28.

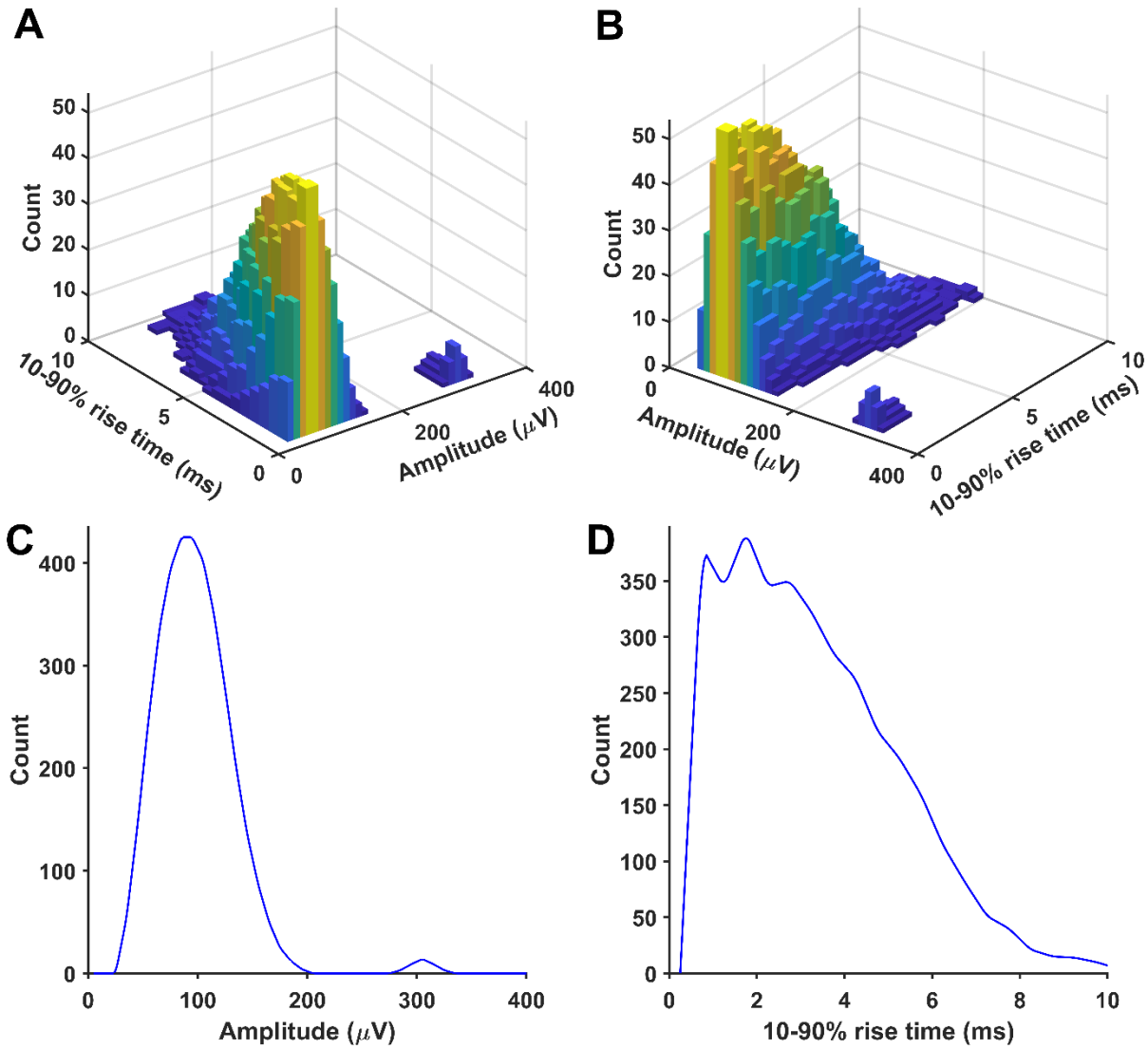

1334

1335 **Supplementary Figure 38:** An example of a distribution of randomly selected simulated minis that

1336 was used to produce a close match between distributions of mini-like events detected in a 'noise

1337 with simulated minis' voltage trace (30 µV lower limit on simulated amplitudes) and a 'noise with

1338 real minis' recording for cell p128c (layer 2/3).

1339 Panels as for Supplementary Figure 28.

1340

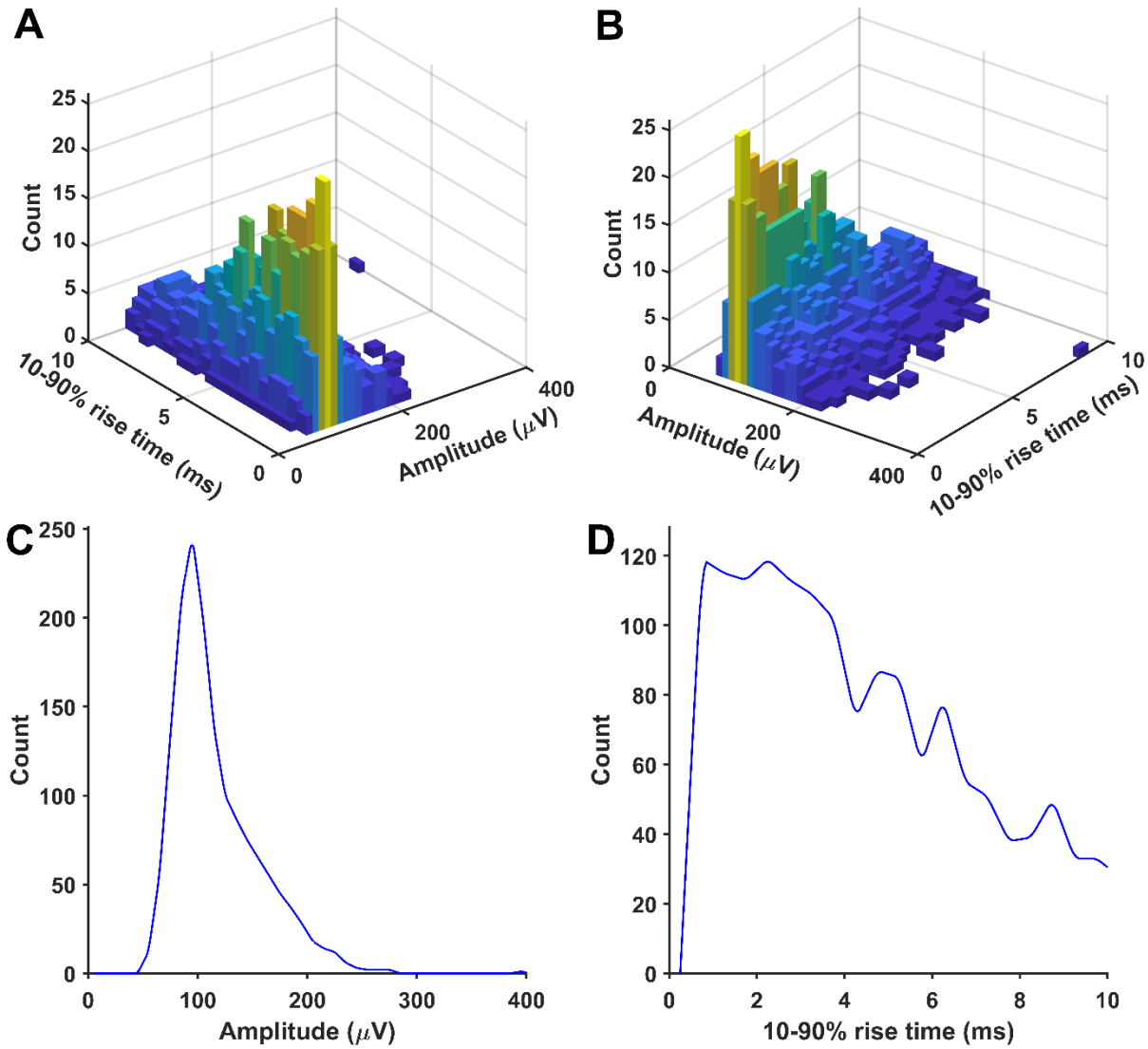

Supplementary Figure 39: An example of a distribution of randomly selected simulated minis that was used to produce a close match between distributions of mini-like events detected in a 'noise with simulated minis' voltage trace (50 µV lower limit on simulated amplitudes) and a 'noise with real minis' recording for cell p129a (layer 5).

Panels as for Supplementary Figure 28.

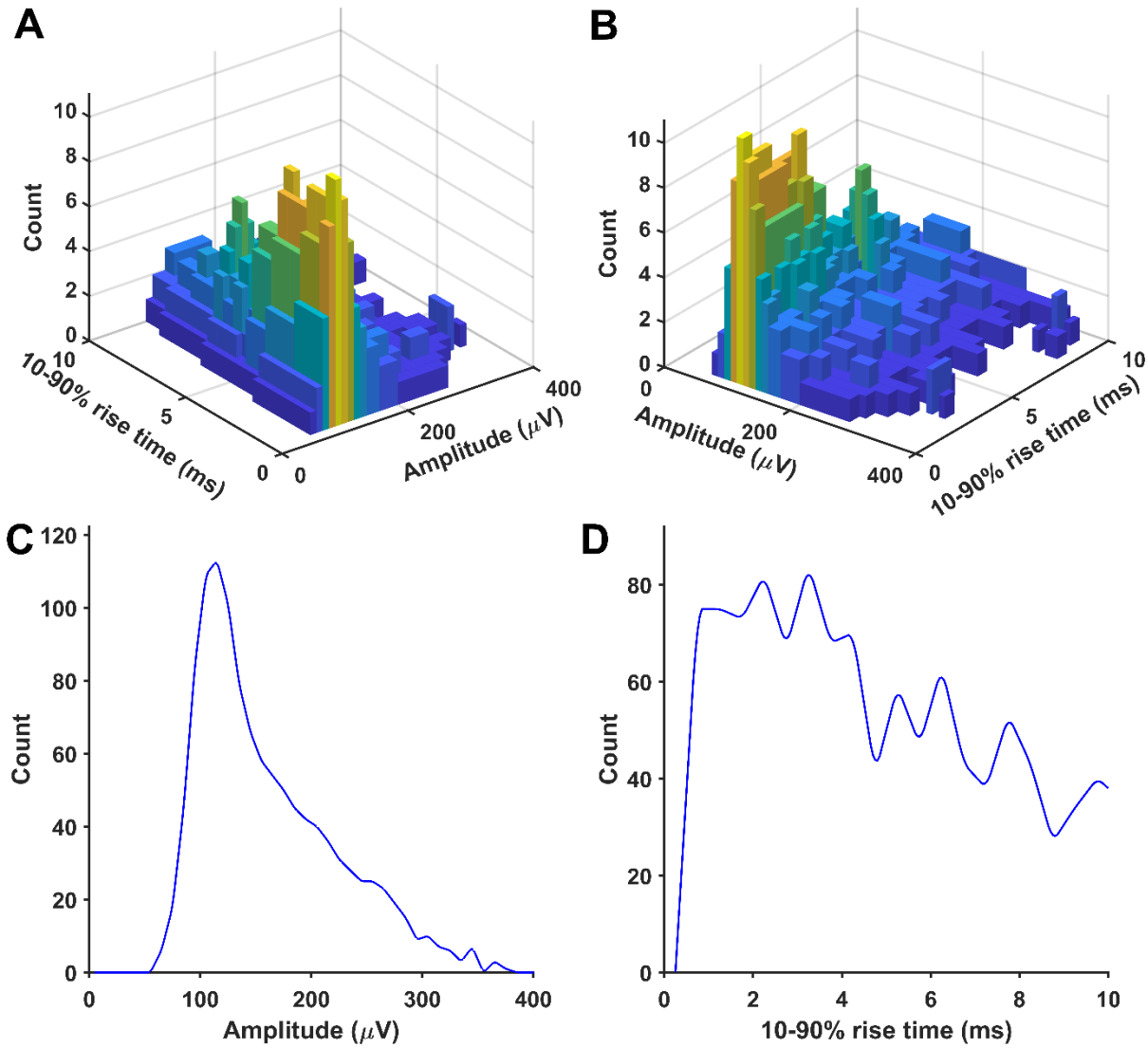

Supplementary Figure 40: An example of a distribution of randomly selected simulated minis that was used to produce a close match between distributions of mini-like events detected in a 'noise with simulated minis' voltage trace (60 µV lower limit on simulated amplitudes) and a 'noise with real minis' recording for cell p131a (layer 2/3).

Panels as for Supplementary Figure 28.